


國立交通大學

機械工程學系

博士論文

常壓平行板型氮與氨混合氣體介電質
電漿的數值模擬研究



**Numerical Investigation of a Parallel-Plate
Atmospheric-Pressure Nitrogen/Ammonia
Dielectric Barrier Discharge**

研究生：李富利

指導教授：吳宗信 博士

西元 2013 年 1 月

常壓平行板型氮與氨混合氣體介電質
電漿的數值模擬研究

Numerical Investigation of a Parallel-Plate
Atmospheric-Pressure Nitrogen/Ammonia
Dielectric Barrier Discharge

研究生：李富利

Student : Fu-Li Li

指導教授：吳宗信 博士

Advisor : Dr. Jong-Shinn Wu



博士論文

A Thesis

Submitted to Department of Mechanical Engineering

National Chiao Tung University

in Partial Fulfillment of the Requirements for the Degree of

Doctor of Philosophy

in Mechanical Engineering

January 2013

Hsinchu, Taiwan

西元 2013 年 1 月

常壓平行板型氮與氦混合氣體介電質電漿的數值模擬研究

學生：李富利

指導教授：吳宗信 博士

國立交通大學 機械工程學系

摘要

在本論文中，利用有限體積法解一維電漿流體模型程式，並進行模擬氮氣混合 0-2% 氦氣以及其含微量氧氣的常壓平板型介電質電漿。模擬中使用 30 kHz 頻率的脈衝式或正弦波電源驅動常壓介電質電漿。本論文研究主要可分成四部份，以下將依序簡介每一部份：

在第一部份，模擬常壓平板型氮與氦混合氣體介電質電漿。建構「氮/氦電漿化學模組」包含 23 種粒子和 141 條氣相化學反應式模擬電漿。模擬的電流密度於相位和大小與實驗量測的數據有相當的一致性。模擬的結果顯示氮氣混合 0-2% 氦氣電漿均為典型的類湯森電漿 (Townsend-like discharge)。因為離子的數量超過電子的數量太多，致使在遍及整個週期中電漿空間沒有電中性區域。我們發現於電漿崩潰 (breakdown) 發生過程和之後 N_2^+ 和 N_4^+ 等離子含量最多，類似純氮氣介電質電漿，其中 NH_4^+ 離子隨添加氦氣濃度增高而快速增加。增加氦氣濃度至氮氣電漿中，胺基 (NH_2) 和 H 原子隨之增加。另外，除背景氣體氮和氦等以外，中性氣體以 N 原子濃度最高。胺基在很多需要官能基接植 (functional group incorporation) 應用裡扮演著相當重要的角色。

在第二部份，針對常壓平板型氮與氦混合氣體介電質電漿進行廣泛的參數研究，包含交流正弦波電壓源不同的電壓峰值 (6-10 kV)、不同頻率 (10-100 kHz)、不同介電質材料 (石英和陶瓷)、不同介電質厚度 (0.5-2 mm) 以及不同電漿空

間距離 (0.1-1.2 mm) 等。研究結果顯示電漿的電流密度和電漿密度隨下列情形而增加：電壓增加、頻率增加、在相同介電質厚度條件下，介電質常數增加、在相同介電質常數條件下，介電質厚度變薄以及電漿空間距離增加。在所有模擬結果中，發現電漿均為典型的類湯森電漿。 N_2^+ 、 N_4^+ 以及 NH_4^+ 都是最重要的帶電粒子， N 、 N_2^* 、 NH_2 以及 H 都是最重要的中性粒子。

在第三部份，以數值與實驗方式對常壓氮氬介電質電漿在考慮微量氧氣雜質進行研究它的光源產生機制：包含 $NO-\gamma$ 、 $NO-\beta$ 以及 N_2 -SPS (second positive system) 等。建構完成的「氮/氧/氬電漿化學模組」包含 48 種粒子和 235 條氣相化學反應式模擬電漿。模擬結果趨勢與使用放射光譜 (optical emission spectroscopy) 量測電漿產生的光強度相當符合。研究結果發現 $NO-\gamma$ 隨著氮氣含量增加而減少，主要因為 $N_2(A^3\Sigma_u^+)$ 及 $NO(A)$ 被氮氣消耗。 $NO-\beta$ 隨著氮氣含量增加而減少，主要因為氮氣與 N 原子和 O 原子進行化學反應而耗損。 N_2 -SPS 隨著氮氣含量增加而減少，主要因為氮氣具高度電子親和力以及介穩態氮氣聯合離子化(associate ionization)效應變弱使得電子生成速率減弱。同時因為在電漿崩潰區間內離子濃度遠超過電子濃度及電場空間分佈僅受帶電粒子存在輕微的影響，添加 0-1%氮氣的氮氣 (含微量氧氣雜質) 的電漿仍視為典型的類湯森電漿。

在第四部份，發展簡化電漿化學反應機制方法，並對前述完整「氮/氧/氬電漿化學模組」包含 48 種粒子和 235 條化學反應式進行簡化。簡化電漿化學模組結果包含 33 種粒子和 87 條化學反應式。在氮氣含微量氧氣條件下添加氮氣濃度從 0%至 1%，使用完整和簡化的電漿化學模擬氮/氧/氬介電質電漿結果比較，結果顯示 33 種粒子密度和電漿的電流密度均具良好一致性。使用簡化的電漿化學模組模擬電漿的計算時間有效縮短 2.1 倍，且具有相同電性以及 33 種粒子密度之均方根誤差都小於 1.8%。

最後，將本論文研究的主要發現做為總結，並條列出對未來研究的建議方向。

關鍵字：電漿、常壓介電質電漿、類湯森電漿、流體模型、有限體積法、氮/氧/
氬電漿。



Numerical Investigation of a Parallel-Plate Atmospheric-Pressure Nitrogen/Ammonia Dielectric Barrier Discharge

Student: Fu-Li Li

Advisor: Dr. Jong-Shinn Wu

Department of Mechanical Engineering
National Chiao Tung University

Abstract

In this thesis, the planar atmospheric-pressure dielectric barrier discharges (AP-DBD) of nitrogen mixed with ammonia (0-2%) considering with and without oxygen impurity were simulated using one-dimensional self-consistent fluid modeling by applying the cell-centered finite-volume method. These AP-DBDs were driven by a 30 kHz power source with distorted sinusoidal or purely sinusoidal voltages. Researches in this thesis are divided into four major parts and are described in the following in turn.

In the first part, the N_2/NH_3 AP-DBDs were numerically investigated using a 1-D fluid modeling with 23 species and 141 reaction channels. The simulated discharge current densities are found to be in good agreement with the experimental data in both phase and magnitude. The simulated results show that the discharges of N_2 mixed with NH_3 (0-2%) are all typical Townsend-like discharges because the ions always outnumber the electrons greatly which leads to no quasi-neutral region in the gap throughout the cycle. N_2^+ and N_4^+ are found to be the most abundant charged species during and after the breakdown process, respectively, like a pure nitrogen DBD. NH_4^+ increases rapidly with increasing addition of NH_3 initially and levels off

with further increase of NH_3 . In addition, N is the most dominant neutral species, except the background species, N_2 and NH_3 . NH_2 and H are the second dominant species, which increase with the increasing addition of NH_3 . The existence of abundant NH_2 plays an important role in those applications which require functional group incorporation.

In the second part, an extensive parametric study of fluid modeling of N_2/NH_3 AP-DBD by varying the voltage amplitude of AC power source with sinusoidal voltages (6-10 kV), voltage frequency of AC power source with sinusoidal voltages (10-100 kHz), dielectric materials (quartz and ceramic), dielectric thickness (0.5-2 mm), and gap distance (0.1-1.2 mm), has been investigated. The results show that the discharge current density and species densities increase with 1) increasing amplitude of applied voltage, 2) increasing frequency of applied voltage, 3) increasing dielectric constant at the same thickness, 4) decreasing dielectric thickness at the same dielectric constant, and 5) increasing gap distance. For all these cases, we have found that they are typical Townsend-like discharges in an average sense in which N_2^+ , N_4^+ and NH_4^+ are found to be the most dominant ions species, and N, N_2^* , NH_2 , and H are the most dominant neutral species.

In the third part, the mechanisms of the light emissions, including NO- γ , NO- β and N_2 -SPS (second positive system), produced in a N_2/NH_3 AP-DBD considering realistic oxygen impurity was investigated numerically and experimentally. Self-consistent, one-dimensional fluid modeling was used to numerically simulate the discharge process with 48 species and 235 reaction channels. An optical emission spectroscopy (OES) was used to measure the relative intensities of the light emission. The simulations of the light emission intensities for the above-mentioned OES lines generally reproduced the trends observed in the experiments caused by changes in the NH_3 concentration. All of the predicted intensities of NO- γ , NO- β and N_2 -SPS

decreased with increasing amount of NH_3 caused by various reaction mechanisms. The former is due to the loss of $\text{N}_2(\text{A})$ and $\text{NO}(\text{A})$ by the reaction of NH_3 with $\text{N}_2(\text{A})$ and $\text{NO}(\text{A})$ respectively. The decrease of $\text{NO}-\beta$ is due to the depletion of N and O because of NH_3 , and the decrease of $\text{N}_2\text{-SPS}$ is due to electron attachment to NH_3 and a weaker metastable-metastable associative ionization of N_2 . All of the simulated results demonstrate that the discharges are typically Townsend-like because ions outnumber electrons and the electric field across the gap is distorted only slightly by the charged particles during the breakdown.

In the final part, a reduced chemical kinetics model for a planar atmospheric-pressure $\text{N}_2/\text{O}_2/\text{NH}_3$ dielectric barrier discharge is proposed and validated by benchmarking against a more complete version as shown in the third part. The set of complete chemistry, including 48 species and 235 reactions, has been successfully reduced to that consisting of 33 species and 87 reactions with a very limited loss of accuracy. The results show that the computational time for 1-D fluid modeling using the reduced chemistry is 2.1 times faster with essentially the same electrical properties and produces less than 1.8% of the root mean squared errors of major species compared to using the complete chemistry, when the oxygen (impurity) is taken to be 30 ppm and the ammonia varies in the range of 0-1%. The current density produced by the reduced chemistry is also found to be in excellent agreement with the current density produced by the complete chemistry.

Finally, major findings and recommendations for future study are summarized and outlined at the end of the thesis.

Keywords: plasma; atmospheric-pressure dielectric barrier discharge; Townsend-like discharge; fluid modeling; finite-volume method; nitrogen/oxygen /ammonia discharge

誌謝

在就讀博士班期間來，承蒙眾人的幫忙，得以完成學業。首先誠摯感謝指導教授吳宗信博士在研究上提供卓越見解、生活上照顧以及辛勞校訂論文，因此本論文得以順利完成，至為感激。在待人處事上，老師不遺餘力地諄諄教導，讓學生獲益良多。感恩您！

誠摯感謝敬愛的父親李進金與母親方塩甜，三十幾年來含辛茹苦栽培我取得博士學位。您們無怨無悔默默的付出與支持是我完成學業最重要的關鍵。感謝弟弟們富財和富榮在新竹照應，妹妹梅玲在家照顧父母。家人多方支持，讓我無後顧之憂，得以全心全力致力於學業上。因此，謹以本文獻給所摯愛的家人。

感謝口試委員林昭安教授、廖國基教授、陳彥升博士、魏大欽教授以及陳慶耀教授們在百忙之中對論文提供寶貴的建議與指正，使得本論文更臻完善。

感謝涂文福博士在交大求學期間熱心的相助、鼓勵及請客等。一起旅遊和聚餐的時光是美好的回憶。

感謝許國賢學長教導 PIC-MCC code、林昆模提供 Fluid Modeling code 與研究資料、古必任教導程式操作、楊宜偉量測實驗數據、洪捷祭、鄭凱文、邱沅明、胡孟樺、周子豪、邱垂青、王聖毅、林哲緯以及劉惠云等研究室的成員協助，得以順利完成研究。

感謝西如寺鳳師父在求學生涯裡扮演明燈與啟發，讓我有不一樣人生歷程，最終長途的求學旅程美妙地畫下句點。

最後，將獲得博士學位的喜悅獻給關心我的人們。謝謝您們！

Table of Contents

摘要.....	i
Abstract.....	iv
誌謝.....	vii
Table of Contents	viii
List of Tables.....	xi
List of Figures.....	xii
Nomenclature	xvi
Chapter 1 Introduction.....	1
1.1 Background and Motivation	1
1.2 Dielectric Barrier Discharge	3
<i>1.2.1 Homogeneous Dielectric Barrier Discharge</i>	<i>3</i>
<i>1.2.2 Classification of Homogeneous Dielectric Barrier Discharge</i>	<i>4</i>
1.3 Nitrogen Atmospheric-Pressure Dielectric Barrier Discharge	4
1.4 Literature Survey	5
<i>1.4.1 Experiments of N₂/NH₃ AP-DBD</i>	<i>5</i>
<i>1.4.2 Experiments of N₂/NH₃ AP-DBD Considering Oxygen Impurity</i>	<i>6</i>
<i>1.4.3 Algorithms of Reduced Chemical Kinetics.....</i>	<i>7</i>
1.5 Specific Objectives of the Thesis.....	8
1.6 Organization of the Thesis	9
Chapter 2 Numerical Methods	11
2.1 Fluid Modeling Equations	11
2.2 Discretization, Numerical Schemes and Algorithms.....	14
2.3 Boundary Conditions.....	15
2.4 Experimental Methods	16
Chapter 3 One-Dimensional Fluid Modeling of Nitrogen/Ammonia Dielectric Barrier Discharge	18
3.1 Plasma Chemistry	18
3.2 Simulation Conditions	19
3.3 Fitting of Applied Voltage Waveform.....	19
3.4 Grid Convergence Tests	20
3.5 Validation with Experimental Results	21
3.6 Effects of Ammonia Addition on Nitrogen Discharge	22
3.7 Summary.....	25

Chapter 4 Parametric Study of One-Dimensional Fluid Modeling of Nitrogen/Ammonia Dielectric Barrier Discharge	27
4.1 Simulation conditions	27
4.2 Effect of Varying Voltage Amplitudes of Power Source	27
4.3 Effect of Varying Driving Frequencies of Power Source	29
4.4 Effect of Varying Dielectric Materials	30
4.5 Effect of Varying Dielectric Thickness	31
4.6 Effect of Varying Gap Distances	32
4.7 Summary.....	32
Chapter 5 One-Dimensional Fluid Modeling of Nitrogen/Ammonia Dielectric Barrier Discharge Considering Oxygen Impurity	34
5.1 Plasma Chemistry	34
5.2 Simulation Conditions	35
5.3 Optical Emission Spectra Measurements	35
5.4 Validation with the Experimental Results.....	36
5.5 Distributions of Number Densities of Discharged Properties.....	37
5.6 Discharge Structure in the N_2/O_2 and $N_2/O_2/NH_3$ Discharges	41
5.7 Power Absorption in the N_2/O_2 and $N_2/O_2/NH_3$ Discharges.....	42
5.8 Summary.....	43
Chapter 6 A Reduced Chemical Kinetics for Atmospheric-Pressure Nitrogen/Oxygen/Ammonia Dielectric Barrier Discharge.....	45
6.1 Plasma chemistry	45
6.2 Simulation Conditions	45
6.3 Algorithm of Reducing Chemical Kinetics.....	45
6.4 Proposed Reduced Chemical Kinetics of the $N_2/O_2/NH_3$ Discharges.....	47
6.5 Summary.....	49
Chapter 7 Conclusion and Recommendations for Future Work	50
7.1 Summaries of the Thesis.....	50
7.1.1 <i>One-Dimensional Fluid Modeling of Nitrogen/Ammonia Dielectric Barrier Discharge</i>	<i>50</i>
7.1.2 <i>Parametric Study of One-Dimensional Fluid Modeling of Nitrogen/Ammonia Dielectric Barrier Discharge.....</i>	<i>51</i>
7.1.3 <i>One-Dimensional Fluid Modeling of Nitrogen/Ammonia Dielectric Barrier Discharge Considering Oxygen Impurity</i>	<i>52</i>
7.1.4 <i>A Reduced Chemical Kinetics for Atmospheric-Pressure Nitrogen/Oxygen/Ammonia Dielectric Barrier Discharge</i>	<i>54</i>
7.2 Recommendations for Future Work	54

References56
Tables.....62
Figures87
List of Publications132



List of Tables

Table 1. Order of magnitude of the different species in the two well characterized homogeneous DBD regimes [29].....	62
Table 2. Electron-Impact Collisions include N ₂ /NH ₃ plasma chemistry. All rate constants are adopted from [49][65].	63
Table 3. Ion-Molecular Collisions include N ₂ /NH ₃ plasma chemistry. T _e is the electron temperature, and T _g is the background gas temperature. Both are in Kelvin.	67
Table 4. Neutral-Neutral Collisions include N ₂ /NH ₃ plasma chemistry. The rate constants are calculated by $k = k_0 \times (T_g / 298)^n \times \exp(-E_a / R T_g)$ where T _g is the background gas temperature (K).	70
Table 5. The test grid convergence for N ₂ /0.01%NH ₃ AP-DBD as the applied voltage of 8 kV and the frequency of 30 kHz.	73
Table 6. Test conditions used for parametric study.	74
Table 7. Summary of N ₂ /O ₂ /NH ₃ plasma chemistry.	75
Table 8. The summary of species with various reduced chemical kinetics.	83
Table 9. Accuracy and computational time with various chemical kinetics.	84
Table 10. The reaction paths for generating the dominant species in N ₂ /NH ₃ discharge.	85
Table 11. The reaction paths for generating the dominant species in N ₂ /O ₂ /NH ₃ discharge.	86

List of Figures

Figure 1. Common planar and cylindrical dielectric barrier discharge configurations [28].	87
Figure 2. Measured light distribution and calculated space distribution from anode to cathode in (a) a He APGD and (b) a N ₂ APTD when the discharge current intensity is maximum [38].	88
Figure 3. The schematic framework of the thesis.	89
Figure 4. The flowchart of fluid modeling simulation.	90
Figure 5. Sketch of a planar N ₂ /NH ₃ atmospheric pressure dielectric barrier discharge system.	91
Figure 6. The schematic diagram of one-dimensional atmospheric pressure dielectric barrier discharge simulated in the study.	92
Figure 7. The test grid convergence for N ₂ /0.01% NH ₃ AP-DBD as the applied voltage of 8 kV and the frequency of 30 kHz.	93
Figure 8. Comparison between the simulated and measured current density in pure nitrogen AP-DBD.	94
Figure 9. Spatiotemporal averaged number densities of charge species with concentration ratio of ammonia in AP-DBD.	95
Figure 10. Temporal profiles of the space-averaged number densities of charge species for N ₂ /0.1%NH ₃ AP-DBD.	96
Figure 11. Temporal profiles of the space-averaged number densities of neutral species for N ₂ /0.1%NH ₃ AP-DBD.	97
Figure 12. Distributions of charge species densities across the electrode gap for N ₂ /0.1%NH ₃ AP-DBD at the peak of discharge current density.	98
Figure 13. Distributions of charge species densities across the electrode gap for N ₂ /0.1%NH ₃ AP-DBD in the post-breakdown period.	99
Figure 14. Spatiotemporal distribution of electron number density.	100

Figure 15. Spatiotemporal distribution of N_2^+ number density.....	101
Figure 16. Spatiotemporal averaged number densities of neutral species with concentration ratio of ammonia in AP-DBD.	102
Figure 17. Temporal variation of discharge properties: (a) discharge current density, (b) gap voltage, and (c) electron number density with various amplitude of voltage.....	104
Figure 18. Spatiotemporal averaged number densities of (a) charged species and (b) neutrals with various amplitude of voltage.....	105
Figure 19. Temporal variation of discharge properties: (a) discharge current density, (b) gap voltage, (c) electron number density, and (d) power absorbed by electrons with various frequencies of applied voltage.	107
Figure 20. Temporal variation of accumulated charge on powered dielectric (Q_a) at 100 kHz of frequency of applied voltage.....	108
Figure 21. Spatiotemporal averaged number densities of (a) charged species and (b) neutrals with various frequencies.....	109
Figure 22. Temporal variation of (a) discharge current density and (b) gap voltage with various dielectric materials.	110
Figure 23. Spatiotemporal averaged number densities of (a) charged species and (b) neutrals with various dielectric materials.	111
Figure 24. Temporal variation of discharge current density for various dielectric thicknesses.	112
Figure 25. Spatiotemporal averaged number densities of (a) charged species and (b) neutrals for various dielectric thicknesses.	113
Figure 26. Temporal variation of (a) current density and (b) displacement (J_D) and conduction current density (J_C) at various gap distances.....	114
Figure 27. Spatiotemporal averaged number densities of (a) charged species and (b) neutrals for various gap distances.	115
Figure 28. Optical emission spectra of $N_2/(0-1\%)NH_3$ AP-DBD from 180 to 900 nm under experimental conditions (30 kHz, 8 kV, 50 SLM, 400W).	116

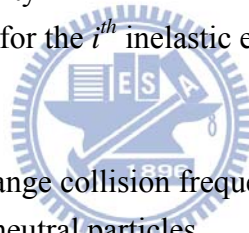
Figure 29. Spatiotemporal distributions of (a) $N_2(C)$ and (b) $N_2(A)$ under same conditions as Brandenburg's experimental conditions [34].	117
Figure 30. Spatiotemporal intensity distributions of (a) N_2 -SPS and $NO-\gamma$ were measured in the gas mixture of 300ppm O_2 in N_2 by Brandenburg <i>et al.</i> [34].	118
Figure 31. Optical emission spectra comparison of simulations and measurements. (Note that 0.001% NH_3 really represents 0% NH_3 on the x-axis.)	119
Figure 32. Spatiotemporal averaged number density of (a) charged, (b) excited and (c) neutral species as function of concentration of ammonia from 0 to 1%.	121
Figure 33. Snapshots of distribution of plasma properties of charged species in (a) $N_2/30ppm-O_2$ and (b) $N_2/30ppm-O_2/1\% NH_3$ discharges at maximum current density.	122
Figure 34. Temporal profiles of space-averaged number densities of charged species in (a) $N_2/30ppm-O_2$ and (b) $N_2/30ppm-O_2/1\% NH_3$ discharges in a cycle.	123
Figure 35. Spatiotemporal distribution of light emission intensity of N_2 -SPS in (a) $N_2/30ppm-O_2$ and (b) $N_2/30ppm-O_2/1\% NH_3$ discharges in a cycle.	124
Figure 36. Temporal power absorption in (a) $N_2/30ppm-O_2$ and (b) $N_2/30ppm-O_2/1\% NH_3$ discharges.	125
Figure 37. Spatiotemporal distribution of electron power absorption in (a) $N_2/30ppm-O_2$ and (b) $N_2/30ppm-O_2/1\% NH_3$ discharges in a cycle.	126
Figure 38. The flowchart of reduced chemistry algorithm.	127
Figure 39. Comparison of rate of production of atomic oxygen among various ammonia concentrations in N_2/O_2 discharges.	128
Figure 40. Comparison of discharge current density among various chemical kinetics in $N_2/30ppm-O_2/0.1\% NH_3$ discharge.	129
Figure 41. Spatiotemporal averaged number density of charged species comparison of complete chemistry and Simplified Chemistry 2 at various concentrations of ammonia.	130
Figure 42. Spatiotemporal averaged number density of excited species comparison of complete chemistry and Simplified Chemistry 2 at various concentrations of	

ammonia.....131



Nomenclature

D	diffusivity
E	electric field
k	rate constant
k_B	Boltzmann constant
m	mass
n	number density
q	charge
S	source/sink of continuity equation
T_e	electron temperature
T_g	Background gas temperature
Γ	particle flux
v_{th}	thermal velocity
ε	permittivity
ε_0	vacuum permittivity
ε_i	threshold energy for the i^{th} inelastic electron collision
ϕ	potential
μ	mobility
ν_m	momentum exchange collision frequency between electron and background neutral particles



Chapter 1 Introduction

1.1 Background and Motivation

Atmospheric-pressure plasmas (APP) have attracted much attention recently mainly because: 1) they do not require the use of expensive vacuum equipment, and 2) they have found increasingly numerous applications in modern science and technology. The former drives the cost down dramatically as compared to low-pressure plasmas and also offers the possibility of in-line processing for mass production in industry. The above have led to development of different kinds of AP plasma sources.

The AP plasma sources are generally classified based on the types of power sources, which may include alternating current (AC) dielectric barrier discharge (DBD) (10-100 kHz), radio frequency (RF) capacitively coupled discharge (1-100 MHz) and microwave discharge (300 MHz - 10 GHz). Among these, DBD may represent one of the most popular discharges because of its easier implementation and simple scalability from small laboratory reactors to large industrial installations.

Among these APPs, dielectric barrier discharges using ammonia have been well studied experimentally because it can produce abundant atomic nitrogen and hydrogen which have been used in various applications such as surface treatment to improve wettability [1], biocompatibility of polymer surfaces [2], surface nitridation for semiconductor applications [3][4], and modifying surfaces for increased adhesion between polymer layers in composite materials [5], among others. There exist several studies of atmospheric-pressure dielectric barrier discharge (AP-DBD) with simulations [nitrogen: [6][7][8]; helium: [9][10][11][12] and experiments [nitrogen: [13][14][15]; helium: [14]]. However, nearly no related simulation study in ammonia DBD has been found, except very few in low-pressure environments for DBD [4] and

ICP [16].

Recently, N_2/NH_3 discharges have also been studied experimentally in low-pressure environment because of its potential applications, such as surface nitridation for semiconductor applications [3][17], etching [18][19][20], reduction of nitrogen oxide [21], modification of surface wetting properties [22] and laser [23]. There have been very few experimental studies of AP-DBD for N_2/NH_3 mixture [24][25][26]. However, no detailed physical and chemical mechanisms of N_2/NH_3 discharges were provided. Thus, better understanding of N_2/NH_3 AP-DBD is strongly desired.

It is well known that detailed experimental measurement of the discharge is not an easy task. Plasma fluid modeling may represent one of the most efficient and cost effective tools in unveiling the insight of complex physics and chemistry in N_2/NH_3 AP-DBD with and without the oxygen impurity level. Hopefully, much deeper understanding of the plasma mechanism can provide more constructive input to the design of plasma source. Unfortunately, there has been no related simulation study on N_2/NH_3 AP-DBD with and without considering the oxygen impurity level to the best knowledge of the authors.

In this thesis, we intend to develop sets of complex plasma chemistry for N_2/NH_3 and $N_2/O_2/NH_3$ discharges, respectively, to describe the behaviors of the gas discharges. The fluid modeling code with the plasma chemistry of N_2/NH_3 and $N_2/O_2/NH_3$ is first validated by good agreement of discharge current densities and discharge light intensities between simulations and experiments. Then, effect of ammonia addition into nitrogen and N_2/O_2 on the structure of gas discharge is presented and discussed in detail.

1.2 Dielectric Barrier Discharge

The dielectric barrier discharges are very attractive for industrial applications because they can provide non-equilibrium plasma which has the temperature of electron much higher than the heavy particles (i.e. ions and neutrals) at atmospheric pressure. The temperatures of the heavy particles usually are close to the room temperature and that of electron is as high as 10,000~50,000K. Therefore, the DBD offers high selectivity and energy efficiency and is able to operate efficiently at low temperature without any special quenching [27]. Figure 1 shows the classical DBD configurations utilize planar and cylindrical arrangements with at least one dielectric layer placed between the electrodes [28]. The typical discharge gas distances are range from 0.1mm to several cm. Dielectric barrier discharges are originally driven by an alternating voltage (10-100 kHz), usually a sine wave. Typical dielectric materials used are quartz, ceramics, glass, or polymers in some applications with additional protective or functional coatings. A primary feature of the DBD is that the dielectric barrier suppresses the occurrence of arc discharges and prevents the metallic electrodes from erosion caused by the arc.

1.2.1 Homogeneous Dielectric Barrier Discharge

Homogeneous discharge has been used in numerous new applications including thin film deposition, bio-decontamination, and aerodynamic flow control [29]. The feature of the homogeneous discharge allows one to treat surfaces more uniformly. Homogeneous DBD at atmospheric pressure could only be obtained under specific conditions, first described by Kanazawa *et al.* [30]. A precise control of the electric circuit (voltages, frequency), working gas composition, dielectric (materials, thickness), discharge gas spacings, and working pressures are needed to obtain such

discharge [28][29][30][31][32].

1.2.2 Classification of Homogeneous Dielectric Barrier Discharge

The homogeneous discharges were classified by Massines *et al.* [29] as atmospheric-pressure glow discharge (APGD or GDBD) and atmospheric-pressure Townsend discharge (APTD or TDBD). The differences between APGD and APTD are summarized in Table 1. Figure 2a shows the major features of APGD in Helium. The glow discharge at atmospheric pressure are typically featured by the high current density ranging from 10-100 mA/cm², a quasi-neutral region (positive column), a high electric field region at the cathode (cathode fall), and maximal light emission near the cathode. Figure 2b shows the major features of APTD in nitrogen. The typical features of Townsend discharge at atmospheric pressure include ions outnumber electron, the low current density ranges from 0.1-10 mA/cm², a quasi-neutral region is absent, the electric field is nearly constant in the discharge gap, and maximal light emission from the excited species appears near the anode.

1.3 Nitrogen Atmospheric-Pressure Dielectric Barrier Discharge

It is relatively easy to obtain the homogeneous barrier discharges in helium [31], nitrogen [31], nitrogen with oxygen impurity [33], nitrogen with the trace amount of oxygen (which less than 400 ppm) [34][35][36][37], and neon [31], among others. Among these gases, nitrogen is often used as the working gas, because its low cost and the homogeneous barrier discharge in nitrogen almost shows a Townsend discharge at atmospheric pressure.

Nitrogen AP-DBD has been studied by simulations and experiments for a long time. Nitrogen AP-DBD has been investigated frequently by one-dimensional fluid

modeling [6][7][8][38]. The results showed that the discharge structure is strongly influenced by different driving frequencies, voltage amplitudes and the dielectric materials. Moreover, nitrogen discharges with addition of other gases for special objectives are not unusual for practical applications. For instance, ammonia is widely added in nitrogen discharges to generate high amount of NH_2 which are believed to be important for the incorporation of amine functional group into materials.

In addition, the nitrogen AP-DBD with small admixtures of oxygen has been investigated by plasma diagnostics (optical emission spectroscopy, OES) and numerical modeling [34][35][36][37]. Brandenburg *et al.* [34] presented that the spatial distribution of the optical emission intensities of discharge with addition of a small amount of oxygen (300 ppm) in nitrogen were measured by spatially resolved cross-correlation spectroscopy (CCS). The spatial distributions of the measured optical emission intensities of N_2 -SPS and NO - γ are used to compare with the current simulated results that will be presented later (Chapter 5).

1.4 Literature Survey

1.4.1 Experiments of N_2/NH_3 AP-DBD

Yang *et al.* [25][26] have developed a two-step AP plasma treatment for increasing the bio-compatibility of polylactide (PLA): first by N_2/O_2 DBD and followed by N_2/NH_3 DBD. Results had shown that appreciable amount of N 1s and NH_2 bond were incorporated into PLA surface after the two-step plasma treatment process. However, no detailed physical and chemical mechanisms of N_2/O_2 and N_2/NH_3 discharges were provided, particularly the latter. Thus, better understanding of N_2/NH_3 AP-DBD is strongly desired. In addition, no detailed parametric study has been performed. Therefore, a systematic parametric study is required to further

understand the underlying plasma physics and chemistry. In this thesis, an extensive parametric study of the discharge characteristics is presented by varying several important operation conditions, including the voltage amplitude of AC power source, the frequency of AC power source, dielectric constant of dielectric material, dielectric thickness, and gap distance between dielectric materials.

1.4.2 Experiments of N_2/NH_3 AP-DBD Considering Oxygen Impurity

As mentioned in the above, N_2/NH_3 AP-DBD has been studied experimentally by Yang *et al.* [25][26], in which the emission spectra (NO- γ , NO- β and N_2 -SPS) were clearly detected. These optical intensities that were measured by optical emission spectroscopy supported the presence of oxygen impurities in the working gas. In addition, these emission spectra were also detected in a nitrogen-based discharge. In a commercial nitrogen bottle (99.99%), we found that the oxygen impurity level could reach ~ 30 ppm, based on the measurements using a gas chromatographer (YL 6100GC, Young Lin Instrument Co., Ltd.). However, in these studies, the mechanisms of optical emissions and effects of oxygen impurity were not explored, which are important in further understanding the complex plasma chemistry. Therefore, for realistic modeling of N_2/NH_3 AP-DBD, the trace oxygen impurity level must be included to reproduce these light emissions. In this thesis, a set of complex reaction pathways for the plasma chemistry of $N_2/O_2/NH_3$ AP-DBD was developed to describe the mechanism of light emission by gas discharge. The effect of ammonia addition into N_2/O_2 discharge on the light intensities of the various emissions will be presented and discussed in detail later (Chapter 5).

1.4.3 Algorithms of Reduced Chemical Kinetics

By reducing the number of reactions and reacting species properly, one can reduce the computational cost of fluid modeling without sacrificing the accuracy of the results. Therefore, the final aim of this study is to develop a general method for deducing a reduced chemical kinetics from the complex plasma chemistry. In general, there are three reduction methods in the study of classical chemical kinetics [42]: a reduction of the number of reacting species and reactions; a reduced mechanism using quasi-steady-state and partial equilibrium assumptions; and a mathematical representation based on the time-scale separation. However, there have been very few studies particularly in reducing plasma chemistry [43][44][45]. For example, Liu *et al.* [43] presented that a set of plasma chemistry with 46 species and 577 reactions in He/H₂O plasma simulated by global model at atmospheric pressure. The reduction of the number of reacting species and reactions has been used to simplify the plasma chemistry. Then, they briefly described reduction methods used by special conditions include the densities of selected species are more than 0.5% of electron density and the reactions contribute more than 2% to the generation/loss of the remaining species. With this simplification, a set of plasma chemistry consisting of 34 species and 90 reactions was found to capture the main reaction behavior of the discharge at low-water vapour concentration (1-30 ppm), while another set consisting of 40 species and 129 reactions was needed when the water vapour concentration was high (30-3000 ppm).

In general, Chemkin [46] has been used to reduce the number of reactions and species in a classical chemical mechanism without involving gas discharges. However, the simulated results using the Plasma PSR module of Chemkin (global modeling) are not compatible with the simulated results using fluid modeling (e.g., 1-D), even with

the same plasma chemistry, because the applied voltage, the driving frequency, the density of species and the electron temperature as a function of time and space are not considered in the 0-D Chemkin code. Therefore, a combination of these two tools is required. In this study, we propose a general reduction method that can reduce the number of species and reaction by combining Chemkin with 1-D fluid modeling with a minimal loss of accuracy.

1.5 Specific Objectives of the Thesis

To understand the insight of the discharges, simulation has become an important method since the direct measurements are either very difficult or very costly to be conducted in such a small gap. The numerical simulation can be used as the supplementary tool of experiments for better understanding of discharge behaviors. An efficient and accurate modeling, which provides detailed plasma physics and chemistry within complex gas discharges, may be also used as an optimization tool for designing a new plasma source. Therefore, in this thesis numerical simulation is used to study N_2/NH_3 AP-DBD with and without the oxygen impurity level in this thesis. The specific objectives of the thesis are summarized as follows:

1. To develop a set of the complex plasma chemistry of N_2/NH_3 that can describe the discharge properly. To validate the one-dimensional fluid modeling code with the plasma chemistry for a N_2/NH_3 AP-DBD, to compare the simulated result with the experimental data, and to study the effects of ammonia in nitrogen AP-DBD and its physics and chemistry.
2. To understand fundamental characteristics of plasma physics and chemistry in a N_2/NH_3 AP-DBD under varying test conditions including voltage amplitudes of power source, driving frequencies of power source, dielectric materials,

- dielectric thickness, and discharge gap distances between dielectric materials.
3. To develop a set of the complex plasma chemistry of $N_2/O_2/NH_3$ that can reproduce the available measurements. To validate one-dimensional fluid modeling code with the plasma chemistry for a N_2/NH_3 AP-DBD with the oxygen impurity, to compare the relative light intensities with the experimental data, and to study the effects of ammonia in N_2/O_2 AP-DBD and its related physics and chemistry.
 4. To develop a general method in deducing a reduced chemical kinetics and to apply it for the $N_2/O_2/NH_3$ AP-DBD.

1.6 Organization of the Thesis

Figure 3 illustrates the schematic framework of the thesis. The organization of the thesis is summarized as follows:

Chapter 2 introduces the research methods consisting of numerical methods and experimental methods.

Chapter 3 presents and discusses the effect of ammonia addition in a nitrogen AP-DBD driven by a realistic sinusoidal voltage power source by comparing simulations with experimental results.

Chapter 4 presents and discusses the parametric study of simulated N_2/NH_3 AP-DBD driven by sinusoidal voltage power source.

Chapter 5 presents and discusses the effects of ammonia addition in a nitrogen AP-DBD considering oxygen impurity that is driven by a realistic distorted sinusoidal voltage power source.

Chapter 6 presents and discusses the general method in deducing a reduced chemical kinetics from a set of complex chemistry combining Chemkin and 1-D fluid

model. The $N_2/O_2/NH_3$ AP-DBD is then used as an example showing the capability of this method.

Chapter 7 summarizes the important findings of the thesis and the recommendations of future research.



Chapter 2 Numerical Methods

To simulate such complicated AP discharge physics and chemistry, a 1-D fluid modeling is employed. We solve a set of model equations self-consistently, including the continuity equations for charged species with drift-diffusion approximation for the momentum equations, the neutral species continuity equations, the electron energy density equations, and Poisson's equations. The collocated cell-centered finite-volume method is used to discretize these equations. The discretized equations are solved using the semi-implicit method to enlarge the simulation time step. The corresponding numerical schemes and algorithms are described in a previous study [39] in detail.

2.1 Fluid Modeling Equations

The governing equations for the fluid modeling of plasma are the same as the previous work [47], which was based on LMEA (local mean energy approximation) approach [48], and are briefly described below for completeness. The general continuity equation for ion species can be written as

$$\frac{\partial n_p}{\partial t} + \vec{\nabla} \cdot \vec{\Gamma}_p = \sum_{i=1}^{r_p} S_{p_i} \quad p=1, \dots, K \quad (1)$$

where n_p is the number density of ion species p , K is the number of ion species, r_p is the number of reaction channels that involve the creation and destruction of ion species p and $\vec{\Gamma}_p$ is the particle flux that is expressed, based on the drift-diffusion approximation, as

$$\vec{\Gamma}_p = \text{sign}(q_p) \mu_p n_p \vec{E} - D_p \vec{\nabla} n_p \quad (2)$$

$$\vec{E} = -\vec{\nabla} \phi \quad (3)$$

where q_p , \vec{E} , ϕ , μ_p , and D_p are the ion charge, the electric field, the electric potential, the ion mobility, and the ion diffusivity respectively. Note that the form of the source term S_{p_i} can be modified according to the modeled reactions describing how the ion species p is generated or destroyed in reaction channel i .

The continuity equation for electron species can be written as

$$\frac{\partial n_e}{\partial t} + \vec{\nabla} \cdot \vec{\Gamma}_e = \sum_{i=1}^{r_e} S_{e_i} \quad (4)$$

where n_e is the number density of electrons, r_e is the number of reaction channels that involve the creation and destruction of electrons and $\vec{\Gamma}_e$ is the corresponding particle flux that is expressed, based on drift-diffusion approximation, as

$$\vec{\Gamma}_e = -\mu_e n_e \vec{E} - D_e \vec{\nabla} n_e \quad (5)$$

where μ_e and D_e are the electron mobility and electron diffusivity, respectively. These two transport coefficients can be readily obtained as a function of the electron temperature from the solution of a publicly available computer code for the Boltzmann equation, named BOLSIG⁺ [49]. Similar to S_{p_i} , the form of S_{e_i} can also be modified according to the modeled reactions that generate or destroy the electron in reaction channel i .

The continuity equation for neutral species can be written as

$$\frac{\partial n_{uc}}{\partial t} + \vec{\nabla} \cdot \vec{\Gamma}_{uc} = \sum_{i=1}^{r_{uc}} S_{uc_i} \quad uc=1, \dots, L \quad (6)$$

where n_{uc} is the number density of uncharged neutral species uc , L is the number of neutral species, r_{uc} is the number of reaction channels that involve the generation and destruction of uncharged species uc and $\vec{\Gamma}_{uc}$ is the corresponding particle flux, neglecting convection effects, which can be expressed as

$$\vec{\Gamma}_{uc} = -D_{uc} \vec{\nabla} n_{uc} \quad (7)$$

where D_{uc} is the diffusivity of neutral species. Similarly, the form of S_{uc_i} can also be modified according to the modeled reactions that generate or destroy the neutral species in reaction channel i .

The electron energy density equation can be expressed as

$$\frac{\partial n_e}{\partial t} + \vec{\nabla} \cdot \vec{\Gamma}_{n_e} = -e\vec{\Gamma}_e \cdot \vec{E} - \sum_{i=1}^{S_c} \varepsilon_i k_i n_e n_i - 3 \frac{m_e}{M} n_e k_B \nu_m (T_e - T_g) \quad (8)$$

where $n_e \left(= \frac{3}{2} n_e k_B T_e \right)$ is the electron energy density, T_e is the electron temperature, e is the charge of electron, ε_i and k_i are the threshold energy and rate constant for the i^{th} inelastic electron collision respectively, S_c is the number of reaction channels of inelastic electron collision, k_B is the Boltzmann constant, ν_m is the momentum exchange collision frequency between the electron (mass m_e) and the background gas (mass M), T_g is the background gas temperature and is assumed to be 400 K. $\vec{\Gamma}_{n_e}$ is the corresponding electron energy density flux and can be expressed as

$$\vec{\Gamma}_{n_e} = \frac{5}{2} k_B T_e \vec{\Gamma}_e - \frac{5}{2} D_e n_e \vec{\nabla} (k_B T_e) \quad (9)$$

The second term on the right-hand side of Eq. (8) represents the sum of the energy losses of the electrons due to inelastic collision with other species. The last term on the right-hand side of Eq. (8) represents the energy losses of the electrons due to elastic collision with the background gas, which can be ignored for low-pressure gas discharges, while it is important for medium-to-atmospheric pressure discharges.

The Poisson equation for electrostatic potential can be expressed as

$$\vec{\nabla} \cdot (\varepsilon \vec{\nabla} \phi) = - \sum_{i=1}^K (qn)_i \quad (10)$$

where ϕ is the potential and ε is a function of position, whose value is either the vacuum or dielectric permittivity.

2.2 Discretization, Numerical Schemes and Algorithms

In the current study, the above equations are discretized using the collocated cell-centered finite-volume method [50]. The discretized equations are solved using the semi-implicit method to enlarge the simulation time step. The fluxes in the continuity equations and the electron energy density equation are calculated with the Scharfetter–Gummel scheme [51]. The backward Euler method is employed as a time-integrator. Details are presented elsewhere [39] and only several key features are described here for brevity. Figure 4 shows the flowchart of fluid modeling simulation. The program starts from the evaluation of transport properties and rate constants of reaction channels. At each time step, the resulting algebraic linear systems are solved equation by equation using parallel preconditioned Krylov subspace method provided by PETSc library [52] through domain decomposition technique on top of the MPI protocol. We have employed the additive Schwarz method, with LU or incomplete LU as a sub-domain solver, for preconditioning the coefficient matrix and then the Generalized Minimal Residual Method [53] for solving the linear matrix equation. For 1-D fluid modeling, the linear matrix equation is solved using the direct LU method since the matrix size is relatively small compared to that in 2-D fluid modeling. The continuity equation of charged species consists of the mobility, the diffusivity, and the local distribution of electric field, which are varied both temporally and spatially. Therefore, the coefficients of the matrices for these continuity equations need to be updated at each time step. Moreover, The electron energy density equation is used to obtain the electron temperature, which is used to update the temporally and spatially varying transport properties and rate constants for the reaction channels.

2.3 Boundary Conditions

The flux-type boundary conditions of ions, electrons, and neutral species are employed on the solid surfaces (dielectric or electrode) as

$$\vec{\Gamma}_p = a \cdot \text{sign}(q_p) \mu_p n_p \vec{E} - D_p \vec{\nabla} n_p \quad (11)$$

$$\vec{\Gamma}_e = -a \cdot \mu_e n_e \vec{E} - D_e \vec{\nabla} n_e + \frac{1}{4} n_e v_{th} \quad (12)$$

$$\vec{\Gamma}_{uc} = -D_{uc} \vec{\nabla} n_{uc} \quad (13)$$

where $a = 1$ if drift velocity ($\text{sign}(q_p) \mu_p \vec{E}$) points toward the dielectric surface, and $a = 0$ otherwise. Note that the calculations of transport coefficients such as mobilities and diffusivities of electron, ions and neutrals will be described wherever they are appropriate in later chapters. The ions and electrons are assumed to be accumulated at the dielectric surface at the boundary, while the neutral species are assumed to be quenched at the dielectric surface in the present study. The thermal velocity of electron is

$$v_{th} = \sqrt{\frac{8k_B T_e}{\pi m_e}} \quad (14)$$

where m_e is the electron mass. For all species, the fluxes at the boundaries of computational domain (except the dielectric surfaces) are assumed to be zero.

The boundary conditions of electron energy density flux at the dielectric surfaces are

$$\vec{\Gamma}_{n_e} = 2k_B T_e \vec{\Gamma}_e \quad (15)$$

For the Poisson equation, the potentials of powered and grounded electrode are assigned with applied voltage and zero potential respectively. The effect of charge accumulation on the dielectric surface is considered and can be expressed as

$$\varepsilon_{dielectric} E_{dielectric} - \varepsilon_{discharge} E_{discharge} = \sigma_{surf} \quad (16)$$

where σ_{surf} is the surface charge density on the dielectric, calculated by integrating fluxes of charged species directed to the dielectric surface as

$$\frac{\partial \sigma_{surf}}{\partial t} = e(\sum \Gamma_i - \sum \Gamma_e) \quad (17)$$

It is assumed that charges remain on the dielectric surface until recombining with opposite charges.

2.4 Experimental Methods

To directly validate the fluid modeling presented in the current study, we performed several corresponding experiments of N₂/NH₃ AP-DBD in our laboratory, which are described in detail in the following. [Figure 5](#) shows the schematic diagram of a planar atmospheric-pressure N₂/NH₃ dielectric barrier discharge along with a gas supply system and the instrumentation for voltage and current measurements. This DBD consists of two parallel copper electrodes (50×50×8 mm each) with embedded cooling water. Each of the electrodes was covered with a 70×70×1 mm quartz plate with measured relative permittivity of 4.76. The distance between the two dielectric plates is kept at 1 mm throughout the study except Chapter 4. The DBD assembly is driven by a 30 kHz power supply (Model Genius-2, EN technologies Inc.) with distorted sinusoidal voltage. The input voltage and output current waveforms across the electrodes of the parallel-plate discharge are measured by a current probe (Tektronix TCP312) and a high-voltage probe (Tektronix P6015A) through a digital oscilloscope (Tektronix TDS1012B). Nitrogen gas (99.99% purity) is used as the discharge gas that flows through the parallel plate. Nitrogen flow rate (50 SLM) is controlled by manually adjustable flowmeters.

The working gas was introduced through two holes at the top of the parallel plate assembly and then passes through a sieved aluminum plate containing 480 holes (0.5 mm in diameter each) for flow velocity redistribution. Afterwards, it flows through a convergent section with length of 10 mm to coincide with the channel gap size (1 mm) at the end of the section. The flow rates were controlled by manually adjustable flowmeters and digital mass flow controllers (BROOKS 5850E series). Furthermore, various working gases flow through the gap between two dielectrics. To note that an inevitable existence of impurities in purchased gas cylinder such as O₂ has been carefully verified through gas chromatography in our lab.

The optical emission intensities of the AP-DBD were measured using a monochromator (PI Acton SP 2500) with a Photomultiplier tube (Hamamatsu R928), which was mounted on a mobile 3-D table. The measured location of optical emission spectra was in the discharge region. The spectra were measured from 180 to 900 nm with 1200-g/mm grating (Holographic, 300-nm Blaze and 500-nm Blaze). To note that the linear dispersion is 1.489 nm/mm while the center wavelength of emission line is 400 nm. Both sides of the fiber (Ocean Optic. BTW-FPC-600-0.22-1.5-UV, 600 μ m) were connected to the SMA adapter of the monochromator and the collimating lenses (Ocean Optics 74-UV), respectively.

Chapter 3 One-Dimensional Fluid Modeling of Nitrogen/Ammonia Dielectric Barrier Discharge

3.1 Plasma Chemistry

In the plasma chemistry, we consider 23 species (e^- , NH^+ , NH_2^+ , NH_3^+ , NH_4^+ , N^+ , N_2^+ , N_4^+ , H^+ , H_2^+ , N^* , N_2^* , NH , NH_2 , N_2H , N_2H_3 , N , H , N_2H_2 , N_2H_4 , H_2 , N_2 , and NH_3) and 141 reaction channels as summarized in [Table 2](#) to [Table 4](#), which include 56 electron-impact reactions, 34 ion-molecular reactions and 51 neutral-neutral reactions respectively. Reaction channels 1 to 22 consider chemistry for the pure ammonia discharge, reaction channels 23 to 43 consider chemistry for the pure nitrogen discharge, reaction channels 44 to 56 consider chemistry for the pure hydrogen discharge, while the rest consider chemistry among the species. This set of N_2/NH_3 plasma chemistry includes momentum transfer collision, electron-impact vibrational excitation, electron-impact rotational excitation, electron-impact electronic excitation, electron-impact ionization, electron-impact dissociation, electron-impact dissociative ionization, electron-ion recombination, electron-ion dissociative recombination, ion-molecular charge exchange, ion-molecular metastable into ground state, metastable-metastable associative ionization. The transport coefficients and the rate constants related to the electrons are calculated by solving the Boltzmann equation using BOLSIG⁺ [49]. Note that these coefficients were predicted and stored in a lookup table as function of the electron temperature in N_2/NH_3 background gas at temperature of 400 K. The mobilities of the ions are taken from the literature [54][55], and the corresponding diffusivities are calculated using the Einstein relation. The diffusivities of the neutral species are calculated from the Chapman-Enskog equation for binary diffusion [56]. The diffusivities of excited neutral species are assumed to be

equal to those of the corresponding ground-state neutral species.

3.2 Simulation Conditions

Figure 6 illustrates the schematic diagram of the one-dimensional atmospheric-pressure dielectric barrier discharge. The discharge is sustained in the 1-mm gap between two electrodes (50 x 50 mm each) with each covered by a 1-mm thick quartz plate having measured relative permittivity of 4.76. The powered electrode (left) is driven by a 30 kHz power source with distorted sinusoidal voltages of 8 kV in amplitude, and the right electrode is grounded throughout the cycle. This configuration is kept the same through the study. Effect of ammonia addition in the range of 0-2% is considered in the simulations. 130 cells with non-uniform spacing were found to be accurate enough after detailed grid convergence study and were used throughout the study. Time step is set as $10^{-10} \sim 10^{-11}$ seconds, unless otherwise specified. The electrical properties of the discharges remain essentially the same after 3-5 cycles of simulation, although the neutral species are still evolving slightly. Thus, we have used the results obtained at 5th cycle throughout Chapter 3.

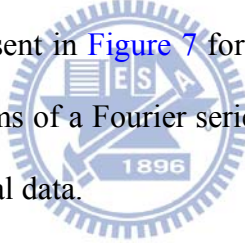
3.3 Fitting of Applied Voltage Waveform

The AP-DBD problem investigated here is driven by quasi-pulse power source with a frequency of 30 kHz. Input temporal voltages waveform for simulations are fitted by a Fourier series expansion of the measured voltage waveform across electrodes using 30 terms of sine and cosine function with 30 kHz as fundamental frequency. In general, this fitting method can be applied to any arbitrary realistic voltage waveform, which is described in detail in the following.

Since the experimental voltage waveform is not an ideal sinusoidal one, we need to fit the voltage properly for an efficient numerical study. The experimental voltages are fitted using a Fourier series as shown in Eq. (18).

$$f(x) = c + \sum_{n=0}^n \left[a_n \cos\left(\frac{n\pi x}{T}\right) + b_n \sin\left(\frac{n\pi x}{T}\right) \right] \quad (18)$$

Theoretically, Fourier series is capable of fitting arbitrary voltage waveform. At each time step, the voltage of powered electrode is calculated with the fitted Fourier series as the boundary conditions of Poisson equation. It is important to determine the number of terms of Fourier series. If too few terms are used, the experimental voltage may not be fitted well due to insufficient degrees of freedom. If too many terms are used, the small variation of high frequency components of Fourier series leads to the oscillation of simulated current. The simulation temporal discharge current density along with measurements is present in Figure 7 for discharge as applied voltage of 8 kV with voltage fitted by 30 terms of a Fourier series, the result of fitted voltage is in well agreement with experimental data.



3.4 Grid Convergence Tests

Figure 7 shows that test grid independence on discharges for $N_2/0.01\%NH_3$ AP-DBD as the applied voltage of 8 kV and the frequency of 30 kHz. There is no obvious difference to be observed for various cell numbers throughout a cycle. Table 5 shows cycle-spatial-averaged number densities for various cell number, the result of 60 cells underestimates the number densities of charge species throughout a cycle, which overestimates the number densities of neutral species throughout a cycle, while the those results of 130 and 370 cells is similar. Therefore, we chose 130 cells for all simulation.

3.5 Validation with Experimental Results

Figure 8 shows the comparison of simulated discharge current densities generated by a pure nitrogen AP-DBD with the experimental data obtained in this study. Detailed description of the experimental setup can be found in Chiang *et al.* [57] and are not repeated here for brevity. On top of the figure, there is a photo taken from the bottom of the discharge with 0.2 seconds of exposure time. It shows that the discharge is very uniform in the direction parallel to the plates, which may justify the use of 1-D fluid modeling in the current study. Similar homogeneous DBDs with nitrogen at atmospheric condition were also found in several previous experimental and numerical studies [[29][31] and references cited therein]. Results show that the simulated discharge current densities are in excellent agreement with the measurements quantitatively. This may be attributed to the LMEA approach adopted in the current fluid modeling, which has demonstrated better agreement with measurements for low-pressure gas discharge [48], although it is atmospheric in the current study. Similarly, the discharge current densities for the cases of 0.1% and 2.0% addition of NH₃ are found to agree well with the experiments. In general, the addition of NH₃ into the nitrogen AP-DBD does not influence the discharge current densities very much based on the simulations and experiments, although the visible light emission becomes dimmer with increasing concentration of NH₃. The dimmer light emission with increasing ammonia amount may possibly be attributed to less emission of photons resulting from, e.g., N₂(C³Π_u) to N₂(B³Π_g) and makes the photo much dimmer. The problem will be discussed in Chapter 5.

3.6 Effects of Ammonia Addition on Nitrogen Discharge

Figure 9 shows the spatiotemporal averaged number densities of various charged species as a function of different concentrations of ammonia addition in a nitrogen AP-DBD. Results show that charged species such as electron, N_2^+ and N_4^+ are essentially the same with ammonia addition in the range of 0-2%, which leads to the approximately the same discharge current densities. In addition, N_2^+ is the most dominant charged species and is at least two orders of magnitude more than electron, which is a typical feature of Townsend-like discharge. In the current study, the electric field is slightly increased from anode to cathode, much more ions than electrons, much more electrons near the anode, and current density is relatively high ($\sim 10 \text{ mA/cm}^2$), which is termed as “Townsend-like discharge”. For the ammonia reaction related charged species, such as NH_4^+ and NH_2^+ , their concentrations generally increase with increasing addition of ammonia and become roughly the same after 0.5% of ammonia addition. In brief summary, the order of decreasing amount of charged species is $N_2^+ > N_4^+ > N_e > NH_2^+ > NH_4^+$ and $N_2^+ > N_4^+ > NH_4^+ > N_e > NH_2^+$ at smaller and larger ammonia addition respectively.

Figure 10 shows the temporal profiles of space-averaged number densities of charged species of nitrogen AP-DBD with 0.1% ammonia addition. Results demonstrate that the number density of electron is always much smaller than the total number density of ions (N_2^+ and N_4^+) and is nearly the same as NH_4^+ during the gas breakdown period throughout a cycle. The simulated electric field across the gap is almost linear with slight distortion by the charge density during the breakdown period, which will be shown later (Figure 12). The above two phenomena demonstrate that it is a typical Townsend-like discharge [7][38], in which there is no quasi-neutral region and very weak (slightly non-constant) electric field in the gap. In addition, N_2^+ is

found to be most abundant during the breakdown process, while N_4^+ becomes dominant during the post-breakdown process due to associative ionization between metastable nitrogen generated during the breakdown process. NH_4^+ is found to be secondly dominant after the breakdown caused by the charge exchange between NH_x^+ ($x = 1, 2, \text{ and } 3$) ions, leading to the formation of abundant NH_4^+ , which has the smallest ionization potential among all the ions in the chemical reaction channels.

In addition, [Figure 11](#) shows the temporal profiles of space-averaged number densities of neutral species of nitrogen AP-DBD with 0.1% ammonia addition in a cycle. Results show that all neutral species change very little with time except metastable nitrogen throughout a cycle. Metastable nitrogen has changed dramatically with time, which is caused by excitation of electron impact on ground N_2 (No. 32-37 in [Table 2](#)), excited recombination of electron-ion on N_4^+ (No. 5 in [Table 3](#)), excited recombination, exchange of neutral-neutral collision (No. 44, 45, and 47 in [Table 4](#)).

In [Figure 10](#) and [Figure 11](#), the electrical properties of the discharges reach a quasi-steady state at 3-5 cycles. It is because diffusion time scale is much longer than drift time scale due to electric field for charged species. It is also true that densities of neutral species increase slightly with time except the metastable species because of its very short life time. Thus, it is difficult for the neutral species to reach the “real” quasi-steady state within such a short period of physical time (3-5 cycles) in the simulation. However, the structure of discharge remains essentially unchanged even when the neutral species reach equilibrium after very long period of simulation.

[Figure 12](#) and [Figure 13](#) show that the snapshots of distribution of charged species at the peak of the breakdown (highest discharge current density) and after the breakdown, respectively, which further reveals that nitrogen DBD is a typical Townsend-like discharge with addition of 0.1% NH_3 as mentioned earlier. These two

plots both show that ions outnumber electrons throughout the cycle. During the breakdown period, the electric field is almost linear (3-3.5 kV/mm) with slight distortion due to ion space charge and the electron temperature is roughly 5 eV. All the above show that it is a typical Townsend-like discharge as presented by other authors [7][38]. In the post-discharge period, only a very small amount of N_4^+ exists, resulting from the associative ionization of metastable/metastable nitrogen, with nearly a traced amount of electrons. Note the amounts of electron, N_2^+ and NH_4^+ are all very low which are not included in the plots. The corresponding electric field is almost constant with a smaller value (~ 1 kV/mm), which mimics a capacitor without charged particles.

Figure 14 and Figure 15 show the spatiotemporal evolution of number density of electron and N_2^+ along with the temporal simulated current density in a cycle. They show that electrons are concentrated near the anode ($x=1$ mm) and the ions (N_2^+) is relatively uniform across the gap. It clearly shows that ions outnumber electrons very much during the breakdown period near the cathode dielectric surface ($x= 2$ mm) when the discharge current is appreciable.

Finally, Figure 16 presents the spatiotemporal averaged number densities of neutral species as a function of ammonia addition. The results show that the most dominant species is atomic nitrogen which had been observed experimentally in pure nitrogen AP-DBD [58] and remains nearly the same no matter how much ammonia is added with the present test condition. Interestingly, metastable nitrogen shows similar trend, although it is approximately 2 orders of magnitude smaller than the atomic nitrogen. The decreasing order of number densities of all neutral species except metastable nitrogen is $N > NH_2 > H > NH > H_2 > N_2H_2$. Abundant atomic nitrogen is generated from three major types of reaction: 1) dissociation of electron-impact on

NH, NH₂ and N₂ (No. 14, 21, and 38 in Table 2), 2) de-excited metastable atomic nitrogen (No. 7 in Table 3), and 3) dissociation, recombination and excitation into ground state of neutral-neutral collision (No. 12, 16, 42, and 48 in Table 4). The number densities of NH₂, H, NH, H₂ and N₂H₂ increase rapidly with increasing addition of ammonia. It is noted that the primary source of NH₂ generation is by electron impact dissociation with ammonia because of low threshold energy of 5.72 eV for dissociation. Abundant generation of NH₂ in N₂/NH₃ discharge plays an important role in incorporating N1s into some polymer to make it biocompatible [25][26].

3.7 Summary

In this chapter, we have employed one-dimensional self-consistent fluid modeling for simulating a parallel-plate atmospheric-pressure dielectric barrier discharge (driven by a 30 kHz power source) of nitrogen added with small amount of ammonia (0-2%). Simulations were validated by good agreement between predicted and experimental current densities. The simulated results show that the discharges of N₂ mixed with NH₃ (0-2%) are all typical Townsend-like discharges because the ions always outnumber the electrons to a large extent which leads to no quasi-neutral region in the gap throughout the cycle. N₂⁺ and N₄⁺ are found to be the most abundant charged species during and after the breakdown process, respectively, like a pure nitrogen DBD. NH₄⁺ increases rapidly initially, respectively, with increasing addition of NH₃ and levels off eventually. In addition, N is the most dominant neutral species, except the background species, N₂ and NH₃, and NH₂ and H are the second dominant species, which increase with increasing added NH₃ in the range of added ammonia. Abundant H, NH and NH₂ in a discharge of N₂ mixed with NH₃ may play a critical

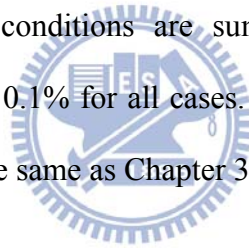
role in some applications which require functional group incorporation [e.g.,
[\[24\]](#)[\[25\]](#)[\[26\]](#)].



Chapter 4 Parametric Study of One-Dimensional Fluid Modeling of Nitrogen/Ammonia Dielectric Barrier Discharge

4.1 Simulation conditions

The discharge is sustained in the gap (0.1-1.2 mm) between two electrodes with each covered by a quartz or ceramic plate (0.5-2 mm) having measured relative permittivity of 4.76 and 11.63, respectively. The powered electrode (left) is driven by an AC power source (10-100 kHz) with sinusoidal voltages, and the right electrode is grounded throughout the cycle. The other simulation conditions are the same as those used in Chapter 3. The test conditions are summarized in [Table 6](#), in which concentration of NH_3 is kept as 0.1% for all cases. The plasma chemistry of N_2/NH_3 AP-DBD used in this study is the same as Chapter 3.



4.2 Effect of Varying Voltage Amplitudes of Power Source

[Figure 17](#) shows the temporal distribution of discharge properties within a cycle at various amplitudes of voltage (6-10 kV with 8 kV as the reference) at the simulation conditions of a frequency of 30 kHz, a gap distance of 1 mm, and quartz as the dielectric material, as those summarized in [Table 6](#). [Figure 17a](#) shows the temporal distributions of discharge current density and the referable applied voltage at different amplitudes of applied voltage. Results show that the maximum current density changes from 2.15 to 4.37 mA/cm^2 as the voltage amplitude increases from 6 to 10 kV and the maximum current density for the 10 kV case is two times larger than that of the 6 kV case. The maximal discharge current density increases with

increasing amplitude of voltage in the range of 6-10 kV because rate of voltage rising of 10 kV is greater than that of 6 kV at the same frequency of oscillation, which favors the energy absorption from electric field for electrons. The results also show that the gas breakdown becomes earlier and longer for the case of larger voltage amplitude. [Figure 17b](#) shows the temporal variation of gap voltage at various amplitudes of applied voltage. Surprisingly, the results show that maximal saturated gap voltage (~ 3 kV) is almost the same for all applied voltages and appears earlier temporally with increasing applied voltages. Note during the breakdown period the resulting electric field is approximately 30 kV/cm that is almost the same as the measured breakdown electric field of nitrogen under atmospheric condition with a similar frequency of power source [\[15\]](#). [Figure 17c](#) shows that maximal electron number density increases nearly two times for the 10 kV case as compared to the 6 kV case, which is attributed to larger rate of gap voltage rising and longer sustaining gap voltage in the former.

[Figure 18a](#) shows the spatially and temporally averaged number densities of charged species for various amplitudes of voltage. The simulated results for the 8 kV case are not shown here for the brevity of presentation. It is seen that the number densities of charged species increase with increasing amplitude of voltage. Among these, N_2^+ , N_4^+ and NH_4^+ are found to be the most dominant ion species. On the other hand, results show that the number density of the most dominant ion species (N_2^+) is much larger than that of electron throughout a cycle in the amplitude range of 6-10 kV. It shows that they are typical Townsend-like discharges [\[7\]\[38\]\[40\]](#).

[Figure 18b](#) shows the number densities of neutral species for various amplitudes of voltage. Results show that the number densities of neutral species for larger amplitude of voltage are always higher than that for smaller amplitude of voltage in a cycle. The most dominant species is atomic nitrogen which is produced

by electron impact dissociation of nitrogen [58]. Moreover, N, N₂^{*}, NH₂, and H are found to be the most dominant neutral species, except background gas, N₂ and NH₃.

4.3 Effect of Varying Driving Frequencies of Power Source

Figure 19 shows the temporal (normalized period) distributions of discharge properties with various frequencies of power source having a voltage amplitude of 8 kV, a gap distance of 1 mm, and dielectric quartz with thickness of 1 mm. Figure 19a shows the temporal distributions of discharge current density with an applied voltage amplitude of 8 kV at various frequencies of 10-100 kHz. Results show that the maximal current density increases 15.2 times from 1.05 to 16 mA/cm² as frequency increases from 10 to 100 kHz. Gas breakdown occurs as the gap voltage exceeds ~30 kV/cm (Figure 19b) [15]. The gap voltages (~3 kV) are also almost the same for all frequencies, except a slight increase with increasing frequency. This is mainly attributed to the increase of rate of change of voltage with increasing driving frequency which causes increasing number density of electrons (Figure 19c) and power absorption by electrons (Figure 19d). Gas breakdown occurs at nearly the same normalized temporal point for all frequencies. In addition, discharge current density and electron number density both oscillate nearly in phase rapidly during gas breakdown period at the frequency of 100 kHz, which shows that the increase of discharge current density is mainly due to the conduction current caused by electrons. Figure 19c shows that electron number density increases with increasing frequency because the higher frequency gives rise to increased dissociation and ionization of the molecules because of increased rate of voltage change. The oscillation of electron number density occurs at the frequency of 100 kHz because of shielding effect caused by a large amount of accumulated charges on the dielectric surfaces, which leads to

discharge quench and re-ignition because of continuous voltage rise and decrease, respectively, during the first half and second half of a period. [Figure 20](#) shows the temporal distributions of applied voltage, gap voltage, current density and accumulated charge on powered dielectric during the rise of voltage at a frequency of 100 kHz. The results show that the oscillation of gap voltage caused by oscillation of current density due to a large amount of accumulated charges on the dielectric surface and continuously increasing voltage leads to the extinguishment of the discharge. A final note to the observation of the rapid oscillation during gas breakdown is that the instantaneous discharge structure is still Townsend-like, in which ions outnumber electron.

[Figure 21a](#) shows the spatially and temporally averaged number densities of charged species for various frequencies (10 and 100 kHz) of applied voltage. Results show that the use of 100 kHz leads to approximately one order of magnitude higher number densities of charged species because of higher rate of change of applied voltage. Among these, N_2^+ , N_4^+ and NH_4^+ are found to be the most dominant ion species, in which their sum of number densities outnumbers that of electron that is a typical Townsend-like discharge structure. [Figure 21b](#) shows the number densities of neutral species for various frequencies of voltage. Results show that averaged number densities of neutral species for higher frequency are always higher than that for lower frequency due to similar reason as explained in the above. Among these, N, N_2^* , NH_2 , and H are found to be the most dominant neutral species.

4.4 Effect of Varying Dielectric Materials

[Figure 22a](#) shows the temporal distribution of current density using quartz and ceramic with permittivity of 4.7 and 11.67, respectively, with the simulation

conditions of an applied voltage of 8 kV, a frequency of 30 kHz, and a gap distance of 1 mm. The maximal discharge current density changes from 3.36 to 9.11 mA/cm² and gas breakdown occurs earlier when quartz is replaced by ceramic dielectric material. It is because the gap voltage is higher for the dielectric material with higher permittivity due to lower voltage drop across the material (Figure 22b). Thus, discharge current density increases with increasing dielectric constant of the material. In addition, Figure 23 show that averaged number densities of charged species and neutral species are generally higher for the case using material with higher dielectric constant.

4.5 Effect of Varying Dielectric Thickness

Figure 24 shows the temporal distribution of discharge current density at two dielectric thicknesses (0.5 and 2.0 mm) under the conditions of 8 kV (applied voltage), 30 kHz (frequency), 1 mm (gap distance) and dielectric quartz in a cycle. The maximal discharge current density changes from 1.47 to 7.1 mA/cm² when the thickness of the dielectric material decreases from 2.0 mm to 0.5 mm. The maximal discharge current density for dielectric thickness of 0.5 mm is about 4.8 times larger than that for dielectric thickness of 2 mm. As a result, the use of dielectric barrier with smaller dielectric thickness leads to higher discharge current density because dielectric voltage for thinner dielectric material is smaller as compared to the thicker dielectric material for the same applied voltage and driving frequency. Thus, discharge current density increases with decreasing thickness of dielectric material. Again Figure 25 shows the averaged number densities of charged and neutral species for the two cases having different dielectric thickness. In general, for the same operating condition, both the number densities of charged and neutral species increase

with decreasing thickness of dielectric material.

4.6 Effect of Varying Gap Distances

Figure 26a shows the temporal profiles of discharge current density of N_2/NH_3 discharges with dielectric quartz for two gap distances (0.1 and 1.2 mm) under the conditions of 8 kV (applied voltage), 30 kHz (frequency), 4.76 (dielectric quartz) and 1 mm (dielectric thickness) in a cycle. We adopt these two gap distances to stand for the extreme cases that the discharge can be maintained. The maximal discharge current density increases from 2.57 to 3.58 mA/cm² when the gap distance increases from 0.1 to 1.2 mm. However, in the case of gap distance of 0.1 mm, the peak current is purely displacement current, while the breakdown occurs much later with a much smaller conduction current as compared to the case of 1.2 mm, as shown in Figure 26b. It is also observed that the current leads voltage nearly 90° in the case of 0.1 mm, which represents a typical capacitor because of very small amount of conduction current, which is very similar to that by [59]. As expected, the averaged charged and neutral species of the 1.2 mm case outnumber those of the 0.1 mm case, which are shown in Figure 27.

4.7 Summary

In this chapter, we have employed one-dimensional self-consistent fluid modeling in simulating a parallel-plate atmospheric-pressure dielectric barrier discharge (driven by a sinusoidal voltage source) of nitrogen mixed with a small amount of ammonia. An extensive parametric study of N_2/NH_3 AP-DBD by varying the five major parameters (amplitude of voltage, frequency, dielectric material,

dielectric thickness, and gap distance) has been performed systematically. Results show that discharge current density and densities of charged and neutral species increase with: 1) increasing amplitude of applied voltage; 2) increasing frequency of applied voltage; 3) increasing permittivity of dielectric material; 4) decreasing dielectric thickness; 5) increasing gap distance from 0.1 to 1.2 mm. In all simulated cases, results show that the gas discharges are typical Townsend-like discharges. N_2^+ , N_4^+ and NH_4^+ are found to be the most dominant ions species; N, N_2^* , NH_2 , and H are found to be the most dominant neutral species, except background gas, N_2 and NH_3 . These results are important in understanding the mechanism of several recent applications of improvement of biocompatibility of PLA by applying N_2/NH_3 dielectric barrier discharge jet [25][26].



Chapter 5 One-Dimensional Fluid Modeling of Nitrogen/Ammonia Dielectric Barrier Discharge Considering Oxygen Impurity

5.1 Plasma Chemistry

In this chapter, a set of plasma chemistry of $N_2/O_2/NH_3$ is proposed, including 48 species (e^- , H^+ , H_2^+ , H_3^+ , N^+ , N_2^+ , N_4^+ , NH^+ , NH_2^+ , NH_3^+ , NH_4^+ , O_2^+ , H^- , O^- , O_2^- , $N(^2D)$, $N(^2P)$, $N_2(A^3\Sigma_u^+)$, $N_2(B^3\Pi_g)$, $N_2(a^1\Sigma_u^-)$, $N_2(C^3\Pi_u)$, $O(^1S)$, $O(^1D)$, $O_2(a)$, $O(^1S)N_2$, $NO(A)$, $NO(B)$, H , H_2 , H_2O , H_2O_2 , HNO , N , N_2 , NH , NH_2 , NH_3 , N_2H , N_2H_2 , N_2H_3 , N_2H_4 , NO , N_2O , NO_2 , O , O_2 , O_3 , and OH) and 235 reaction channels which are summarized in [Table 7](#), providing an extensive consideration of complexity of the related chemical processes. The 235 reaction channels which include 37 electron-molecular reactions, 5 electron-ion reactions, 37 positive ion-molecular reactions, 15 negative ion-molecular reactions, 10 positive ion-negative ion reactions, 124 neutral-neutral reactions and 7 excited species radiation reactions. Physically, this set of $N_2/O_2/NH_3$ plasma chemistry includes momentum transfer collision; electron-impact electronic excitation; electron-impact ionization; electron-impact dissociation; electron-impact dissociative ionization; electron-impact attachment; electron-ion dissociation; electron-ion dissociation from the ground state into an excited state; electron-ion dissociative recombination; positive ion-molecular charge exchange; negative ion-molecular detachment; positive ion-negative ion dissociation; positive ion-negative ion dissociative recombination; metastable-metastable associative ionization; excited/metastable-molecular excitation into an excited or metastable state; excited/metastable-molecular de-excitation into an excited,

metastable, or ground state; and light emission from an excited or metastable state. The light emission of excited species of nitrogen and nitrogen oxide, and electronegative ions are all considered in the model. For NO- γ emission bands, direct electron impact excitation ($e+\text{NO}\rightarrow\text{NO}(\text{A})+e$) is negligible compared to the $\text{N}_2(\text{A})$ quenching channel ($\text{N}_2(\text{A})+\text{NO}\rightarrow\text{N}_2+\text{NO}(\text{A})$) [33]. Thus, we do not consider the reaction of $e+\text{NO}\rightarrow\text{NO}(\text{A})+e$ in this model. The mobilities of O_2^+ and O_x^- ($x=1, 2$) are taken from the literature [60], and the corresponding diffusivities are calculated using the Einstein relation. The transport properties for the other species are described in section 3.1.

5.2 Simulation Conditions

All of the experiments and simulated results presented in this chapter are performed under the conditions of 30 kHz (power supply), 8 kV (voltage), 1 mm (gap distance), 25 cm² (electrode area), 4.76 (quartz plate having measured relative permittivity), 1 mm (quartz thickness), 400 K (temperature of background gas), 30 ppm (oxygen impurity), and 0-1% NH₃. Note we have used the results obtained at the 20th cycle for presentation and discussion throughout this chapter.

5.3 Optical Emission Spectra Measurements

Figure 28 shows the optical emission spectra of the OES measurements for the wavelength range of 180-900 nm in the discharge region under different concentrations of ammonia addition, ranging from 0 to 1%. In the OES measurements, the emission bands of the N₂ second positive system (SPS) (313.6-466.7 nm), NO- γ (220-280 nm) and NO- β (280-380 nm) were detected. Detection of optical emissions

containing O, such as NO- γ and NO- β , in a mixture of pure N₂ and NH₃ is unlikely. The reason for acquiring measurements of NO- γ and NO- β emissions in our experiment was based on the presence of impurities in commercial bottles of nitrogen (99.99% in Taiwan), such as O₂ (~30 ppm), which was verified by the gas chromatography in our laboratory. The results show that the intensities of NO- γ , NO- β and N₂-SPS decrease with increasing amount of NH₃. Furthermore, the emission of NO- γ diminished rapidly and vanished upon reaching a NH₃ concentration of 0.5%. In contrast, the other two emission lines decreased slightly with increasing NH₃ levels. The decreasing intensities of these emission lines due to the addition of ammonia were predicted using the self-consistent fluid model, which are presented next.

5.4 Validation with the Experimental Results

To demonstrate the accuracy of the 1-D self-consistent fluid model for N₂/NH₃ AP-DBD considering oxygen impurity that predicts the light emissions from NO- γ , NO- β and N₂-SPS, we first compared the simulations with earlier experimental data [34]. Figure 29 shows the simulated spatiotemporal density distributions of N₂(C) and N₂(A) along with the applied voltages (black solid line) and conduction currents (red dashed line) in a cycle with a gas mixture of 300 ppm O₂ in N₂ and an estimated oxygen impurity level of 15 ppm under Brandenburg's experimental conditions [34]. These conditions corresponded to a frequency of 6.94 kHz, a sinusoidal voltage of amplitude of 9.7 kV, a gap of 1.1 mm, dielectric barriers with thicknesses of 2.05 mm and 2.3 mm and a permittivity of 4.6, a pressure of 1 atm and a gas temperature of 300 K. The simulated spatiotemporal density distributions of N₂(C) and N₂(A) agree reasonably well with the results from Brandenburg's experiments (Figure 30), although there is a time delay (~ 15 μ s) between the simulated and measured major

breakdowns for the maximal level of contour. The density distributions of $N_2(C)$ and $N_2(A)$ can be compared directly with the measured intensity distributions because the effective lifetimes of $N_2(C)$ and $NO(A)$ are much shorter than the timescale of the density evolution and also because $NO(A)$ is mainly generated by the reaction R111 ($N_2(A)+NO\rightarrow N_2+NO(A)$) [34].

Figure 31 shows the comparison between the predicted and measured light intensities in the discharge. The simulated light intensity of N_2 -SPS was adjusted to match the measurements without ammonia addition. For a better visual arrangement of the data, we have shifted both data points to 0.001% of ammonia addition. We then scaled all of the simulated light intensities, including N_2 -SPS, $NO-\gamma$ and $NO-\beta$, proportionally. For the discussion, specific wavelengths of the emitted light were selected: 337.1 nm (N_2 -SPS), 236 nm ($NO-\gamma$) and 316 nm ($NO-\beta$). The results show that all of the measured light intensities of the discharges decrease with increasing concentration of ammonia, particularly $NO-\gamma$, which decreased dramatically. All of the trends of the three major emission lines were captured by the simulations, and this indicates that the current fluid modeling is reasonably faithful in reproducing the physics of the gas discharge. The spectral intensities in the discharges are dominated by N_2 -SPS, which is induced by electron impact excitation of ground-state nitrogen, whose effective lifetime is on the order of nanoseconds. Additional details about these emission lines will be explained by exploring the discharge properties and are presented next.

5.5 Distributions of Number Densities of Discharged Properties

Figure 32 shows several typical spatiotemporal averaged number densities of charged, excited and neutral species as a function of the amount of added ammonia

under the same test conditions as presented in Figure 31. Figure 32a shows that the densities of the electrons and most ionic species decrease with increasing amounts of added NH₃, except NH₄⁺ and H⁻. The decrease in the electron density is caused by direct electron attachment (R22: e+NH₃→NH₂+H⁻) [61] because NH₃ is an electronegative gas that has high electron affinity. This also induces a rapid increase in the production of negative atomic hydrogens with increasing amounts of NH₃. For added NH₃ concentrations less than 0.1%, the dominant charged species is N₄⁺, which is produced by a charge-exchange reaction (R46: N₂⁺+N₂+N₂→N₄⁺+N₂). This process becomes less efficient as N₂⁺ decreases with increasing NH₃. For NH₃ concentrations greater than 0.1%, the dominant charged species becomes NH₄⁺, caused by charge exchange with NH₂⁺ and NH₃⁺ through the reactions of R58 (NH₂⁺+NH₃→NH₄⁺+NH) and R61 (NH₃⁺+NH₃→NH₄⁺+NH₂). In addition, NH₄⁺ rapidly increases with increasing NH₃ initially, and it then becomes saturated with further increases in NH₃. In fact, NH₃⁺ and NH₂⁺ are generated through the reactions of R47 (N₂⁺+NH₃→NH₃⁺+N₂), R52 (N₄⁺+NH₃→NH₃⁺+2N₂), and R60 (NH₃⁺+NH₃→NH₂⁺+H₂+NH₂), in which N₂⁺ and N₄⁺ are exchanged with NH₃, respectively, to form NH₃⁺. Therefore, N₂⁺ and N₄⁺ are both effectively transformed into NH₄⁺ and decrease with increasing amounts of NH₃.

Figure 32b shows that the number densities of all of the excited species decrease with increasing amounts of ammonia. As expected, N₂(A) remains the dominant excited species in nitrogen with oxygen impurities (without the addition of ammonia) as in a pure nitrogen DBD [62]; however, N₂(A) undergoes a 10-fold decrease when 1% of ammonia is added. Note N₂(A) is mainly generated by excited/neutral de-excitation of N₂(B) by ground-state N₂ (R116: N₂(B)+N₂→N₂(A)+N₂) and is removed by the metastable-metastable excitation (R106: N₂(A)+N₂(A)→N₂(C)+N₂), the metastable-neutral de-excitation (R112:

$N_2(A)+NH_3 \rightarrow N_2+NH_2+H$), and the metastable-neutral de-excitation dissociation (R113: $N_2(A)+NH_3 \rightarrow N_2+NH+H_2$). N_2 -SPS is primarily produced by the de-excitation of $N_2(C)$ (R230), which is also generated by the electronic excitation of nitrogen (R9: $e+N_2 \rightarrow N_2(C)+e$) and removed by the metastable-neutral de-excitation mechanism (R127: $N_2(C)+N_2 \rightarrow N_2(a^1)+N_2$). This leads to a decrease in $N_2(C)$ that is caused by the decrease of electrons due to the addition of ammonia as mentioned earlier. N_2 -SPS emission is proportional to the amount of $N_2(C)$, which explains the slight decrease in N_2 -SPS emission with increasing amounts of NH_3 (Figure 31). In addition, NO - γ emission is produced by de-excitation of $NO(A)$ (R233), which is generated by the two-body collision reaction R111 ($N_2(A)+NO \rightarrow N_2+NO(A)$) and destroyed by the reaction R150 ($NO(A)+NH_3 \rightarrow NO+NH_3$), whose destruction rate is proportional to the amount of ammonia added. $N_2(A)$ is removed via R106, R112 and R113, leading to the decrease of $NO(A)$ through R111. These findings explain the rapid decrease of NO - γ emission as presented in Figure 31. Moreover, NO - β is destroyed through the reaction R234 ($NO(B) \rightarrow NO+h\nu$) and is created by the three-body reactions R156 ($N+O+N_2 \rightarrow NO(B)+N_2$) and R157 ($N+O+NH_3 \rightarrow NO(B)+NH_3$), which are two competing reactions because atomic oxygen decreases rapidly with increasing amounts of NH_3 . This leads to a slight decrease in NO - β emission with increasing amounts of NH_3 (Figure 31).

Figure 32c shows the number densities of the neutral and radical species as a function of the amount of added NH_3 . One immediate observation is that the amount of all of the neutral species containing H atoms initially increases up to 0.1% upon addition of NH_3 and levels off afterwards. As mentioned earlier, the concentrations of N, O and NO, affecting the generation and removal of NO - γ and NO - β , decrease with increasing amounts of NH_3 . For concentrations of NH_3 less than 0.1%, atomic nitrogen is the dominant neutral species, which is generated through the electron

impact dissociation of N_2 (R10: $e+N_2 \rightarrow N+N+e$) and removed through the following reactions: R156 ($N+O+N_2 \rightarrow NO(B)+N_2$), R157 ($N+O+NH_3 \rightarrow NO(B)+NH_3$), R183 ($NH_2+N \rightarrow N_2+2H$) and R211 ($NO+N \rightarrow N_2+O$). For concentrations of NH_3 greater than 0.1%, the dominant neutral species becomes H_2 produced by the reactions of R60 and R113. The results mean that a small amount of the added ammonia into a nitrogen (with oxygen impurities) APDBD can be used to produce abundant hydrogen. Similar results were also observed in a numerical study on H_2 generation in an Ar/ NH_3 microdischarge [4]. The amount of atomic nitrogen decreases with increasing amounts of NH_3 and becomes saturated as more ammonia is added. The trend of N with increasing amounts of NH_3 was similar to that of the electrons (as shown in Figure 32a because it is mostly generated by the direct electron impact dissociation nitrogen and the number of electrons decreases due to reactions R10 ($e+N_2 \rightarrow N+N+e$) and R22 ($e+NH_3 \rightarrow NH_2+H$), respectively.

In addition, the number density of atomic oxygen is decreased by approximately two to three orders of magnitude with an increase in NH_3 concentration from 0% to 1%, mainly through the destructive reactions R108 ($N_2(A)+O \rightarrow O(^1S)+N_2$), R156 ($N+O+N_2 \rightarrow NO(B)+N_2$) and R157 ($N+O+NH_3 \rightarrow NO(B)+NH_3$). This may explain the experimental results of Yang *et al.* [26] showing that the surface roughness of PLA surfaces treated with $N_2/5\% NH_3$ and $N_2/0.1\% O_2$ AP-DBD with an oxygen impurity level of 30 ppm in nitrogen is 1.5 nm and 50.16 nm, respectively. This indicates that the discharge of $N_2/0.1\% O_2$ has a higher etch rate because the etch rate is proportional to the amount of atomic oxygen [63]. Moreover, NO is generated by the reactions R150 ($NO(A)+NH_3 \rightarrow NO+NH_3$), R233 ($NO(A) \rightarrow NO+h\nu$) and R234 ($NO(B) \rightarrow NO+h\nu$), and it is lost by the reactions R111 ($N_2(A)+NO \rightarrow NO(A)+N_2$), R211 ($NO+N \rightarrow N_2+O$) and R213 ($NO+NH_2 \rightarrow N_2+H_2O$). NH_2 is generated by the reactions R60

($\text{NH}_3^+ + \text{NH}_3 \rightarrow \text{NH}_2^+ + \text{H}_2 + \text{NH}_2$) and R112 ($\text{N}_2(\text{A}) + \text{NH}_3 \rightarrow \text{N}_2 + \text{NH}_2 + \text{H}$), and it is lost by the reactions R183 ($\text{NH}_2 + \text{N} \rightarrow \text{N}_2 + 2\text{H}$), R186 ($\text{NH}_2 + \text{NH} \rightarrow \text{H} + \text{N}_2\text{H}_2$), and R188 ($\text{NH}_2 + \text{H} + \text{N}_2 \rightarrow \text{NH}_3 + \text{N}_2$). The densities of NH and NH_2 are approximately constant with NH_3 addition in the range 0.1-1%.

5.6 Discharge Structure in the N_2/O_2 and $\text{N}_2/\text{O}_2/\text{NH}_3$ Discharges

Figure 33 shows snapshots of the spatial distributions of various plasma properties of the N_2/O_2 and $\text{N}_2/\text{O}_2/1\% \text{NH}_3$ discharges at the maximum current density, in which oxygen with an oxygen impurity level of 30 ppm are considered. The results show that the number density of electrons grows rapidly from the cathode to the anode, ions outnumber electrons, except at the anode, and the electric field increases slightly from the anode to the cathode for both discharges. These are typical features of a Townsend-like discharge [7][33][38][40]. The features show that N_2^+ and N_4^+ are the two most dominant species during the breakdown period in the N_2/O_2 discharge. The amount of N_4^+ is slightly more abundant than N_2^+ at the instant when the current density is maximal. Figure 34a shows the temporal distributions of the number densities for N_2^+ and N_4^+ . The amount of N_2^+ approaches that of N_4^+ during the breakdown period because the direct ionization of nitrogen by the electron impact becomes a dominant channel for ionization. As shown in Figure 33b and Figure 34b, NH_4^+ becomes the most dominant species in the $\text{N}_2/\text{O}_2/1\% \text{NH}_3$ AP-DBD because N_2^+ and N_4^+ are exchanged with NH_3 to form NH_4^+ indirectly and effectively, as described in Section 5.5. In the previous experimental studies, the homogeneous discharges for nitrogen with oxygen impurities (less than 400 ppm [34][35][36]) also showed typical Townsend-like discharges. The numerical results for the N_2/O_2 discharge are also consistent with several similar experimental observations [33][34][36].

Figure 35 shows the spatiotemporal distributions of N₂-SPS light emission with the temporal current density in a cycle for the N₂/O₂ and N₂/O₂/1% NH₃ discharges. The period with the highest intensity in the spatial distribution of the N₂-SPS light emission in the N₂/O₂ DBD becomes narrower temporally and elongated spatially compared to that of the N₂/O₂/1% NH₃ DBD during the breakdown period. In addition, the results showing the maximal light emission near the anode are characteristic of Townsend-like discharges [33][34][38]. Thus, all of the results indicate that the discharges are typical Townsend-like discharges even with the ammonia added into the nitrogen with oxygen impurity discharges.

5.7 Power Absorption in the N₂/O₂ and N₂/O₂/NH₃ Discharges

To understand the change in the discharge structure of N₂/O₂ DBD due to the addition of ammonia, we investigated the related power absorptions in the following. Figure 36a shows the temporal distributions of power absorption of the charged species and the displacement current in the N₂/O₂ DBD in a cycle. The results show that the dominant species for power absorption are electrons and N₂⁺ during the gas breakdown. In Figure 33a, N₂⁺ and N₄⁺ are the dominant species with similar levels during the breakdown period in the N₂/O₂ DBD. This is in contrast to the case for the pure N₂ DBD in which the N₄⁺ is the dominant charged species [62]. Because N₂⁺ is much lighter than N₄⁺ (thus, higher mobility), the former absorbs more power than the latter.

Figure 36b shows the temporal distributions of the power absorbed by the charged species and the displacement current in a cycle when 1% NH₃ is added into the N₂/O₂ DBD. The results show that the dominant species for power absorption becomes NH₄⁺ in both gas breakdowns in a cycle, rather than electrons or N₂⁺. The

major cause is that a large amount of NH_4^+ is generated through reactions R58 ($\text{NH}_2^+ + \text{NH}_3 \rightarrow \text{NH}_4^+ + \text{NH}$) and R61 ($\text{NH}_3^+ + \text{NH}_3 \rightarrow \text{NH}_4^+ + \text{NH}_2$) during the gas breakdowns, while the production of N_2^+ and N_4^+ is strongly suppressed because N_2^+ and N_4^+ charge exchange with NH_3 to form NH_3^+ via reactions R47 and R52, respectively. In addition, NH_4^+ is lighter than N_2^+ and N_4^+ . Comparing [Figure 36a](#) and [Figure 36b](#), we have found that the power absorbed by the ionic species increases appreciably as 1% NH_3 is added into the N_2/O_2 DBD. At the same time, the power absorbed by the electrons decreases greatly (~40%) due to the reduced electron number density with increasing NH_3 concentration.

[Figure 37](#) shows the spatiotemporal distributions of the power absorbed by the electrons along with the simulated temporal current densities in the N_2/O_2 and $\text{N}_2/\text{O}_2/1\% \text{NH}_3$ DBDs. The results show that the power absorbed by the electrons decreases with increasing NH_3 because the number of electron decreases with increasing NH_3 . This finding reveals that the light emission weakens with increasing NH_3 because there are fewer electrons that can excite the molecules. Most importantly, the trend of the simulated light intensities agrees with the experimental results shown in [Figure 28](#).

5.8 Summary

In this chapter, we numerically investigated the mechanisms of light emission ($\text{NO-}\gamma$, $\text{NO-}\beta$ and $\text{N}_2\text{-SPS}$) in a planar N_2/NH_3 AP-DBD and included the effects of oxygen impurities using self-consistent 1-D fluid model. The simulated results were validated by their agreement with the OES measurements. The results show that all of the emission intensities decrease as NH_3 increases. The decrease of the $\text{N}_2\text{-SPS}$ line intensity is caused by electrons binding to NH_3 , which weakens the direct electron

impact excitation. The decrease of the NO- γ line intensity is caused by decreases in the amounts of N₂(A) and NO(A), and the decrease of the NO- β line intensity is caused by decreases in both N and O. The simulated results show that the discharges are typical Townsend-like discharges with the nitrogen having oxygen impurities with ammonia addition ranging from 0 to 1%. The power absorbed by the ions for the N₂/O₂ DBD are smaller compared to that for the N₂/O₂ DBD with a small amount of ammonia addition because N₂⁺ and N₄⁺ are exchanged with NH₃ indirectly and effectively to form NH₄⁺, which is lighter than N₂⁺ and N₄⁺. Lastly, the simulated results show that the amount of atomic oxygen decreases rapidly with increasing ammonia addition, which leads to less etching on PLA surfaces, and the simulated results agree with the experimental observations [26].

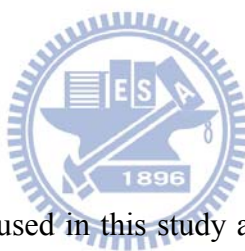


Chapter 6 A Reduced Chemical Kinetics for Atmospheric-Pressure Nitrogen/Oxygen/Ammonia Dielectric Barrier Discharge

6.1 Plasma chemistry

A set of plasma chemistry of $N_2/O_2/NH_3$, namely complete chemistry, used in this study is the same as that summarized in [Table 7](#), including 48 species and 235 reactions. The goal of this chapter is to develop a general method in deducing reduced plasma chemistry from complex plasma chemistry and to apply it to the $N_2/O_2/NH_3$ discharge as mentioned in the above.

6.2 Simulation Conditions



The simulated conditions used in this study are the same as those presented in Chapter 5.

6.3 Algorithm of Reducing Chemical Kinetics

[Figure 38](#) shows the flowchart of how to deduce the reduced chemical kinetics from a set of more complete plasma chemistry by combining Chemikin with 1-D fluid model. Firstly, the global model (0-D) using chemical kinetics is performed via the Plasma PSR module of Chemkin Version 4.1.1 [\[46\]](#) using the simulated results with the more complete plasma chemistry from 1-D fluid modeling as the initial conditions.

Secondly, we select the dominant species (neutral densities more than 10^{-18} m^{-3}

in the case of N₂/O₂/NH₃ discharge. By reducing the number of species, one can reduce the number of continuity equations to be solved in fluid modeling. Fewer species implies that the number of reactions can be also reduced. Therefore, reducing the number of reactions and species can reduce the computational time in the fluid modeling. All the reactions that produce and consume the unselected species can be removed from the reduced set of plasma chemistry. The reduced kinetics is formed by the analysis of the species sensitivity and rate-of-production (ROP) based on the Chemkin simulation. The sensitivity analysis is employed to determine the influential reactions that will be the most relevant to the interesting species. In general, the sensitivity analysis provides complementary information to the ROP analysis. The ROP analysis is employed to determine the major reactions that produce and consume the selected species. ROP can be calculated as

$$ROP_{i,k} = \frac{R_{i,k}}{\sum_{j=1}^m R_{j,k}} \times 100\% \quad (19)$$

where $R_{i,k} = k_i N_A N_B$ denotes the reaction rate of the i^{th} reaction channel related to the k^{th} selected species, which has units 1/m³-s; k_i denotes the rate constant in the i^{th} reaction channel related to the k^{th} selected species; N_A and N_B denote the densities of the reactants or products A and B in the i^{th} reaction channel related to the k^{th} selected species; and m denotes the total number of reaction channels related to the k^{th} selected species. Moreover, a reaction channel can be removed based on the ROP analysis if its contribution to the ROP of each selected species is relatively small. For example, [Figure 39](#) shows the ROP of the reaction channels related to atomic oxygen for different ammonia concentrations in a N₂/O₂ discharge. We select related reactions of O with the ROP larger than 1%, which include R108, R109, R123, R128, R156, R157, R158, and R211. In addition, one needs to re-include the unselected species in a reaction channel, if its exclusion induces a substantial error of the selected species. For

example, OH (whose density is less than 10^{-18} m^{-3}) is not considered in the preliminary list of selected species, which leads to a relative error of H_2O of more than 20% because the reactions R221: $\text{OH} + \text{NH}_3 \rightarrow \text{H}_2\text{O} + \text{NH}_2$ and R137: $\text{O}(^1\text{S}) + \text{H}_2\text{O} \rightarrow 2\text{OH}$ are both dominant reactions for the production and loss of H_2O . Thus, OH should be considered and added to the list of selected species to reduce the error for the prediction of H_2O concentration.

Thirdly, plasma simulation using the results of the simplified plasma chemistry reduced by Chemkin is carried out in 1-D fluid modeling. The results of the concentrations of the selected species are then compared with those obtained by the more complete plasma chemistry. Their relative differences should be smaller than the preset error criteria. Otherwise, the above procedure should be repeated until the differences are smaller than the preset error criteria. Finally, to produce the simplified mechanism, we select the dominant sensitivity coefficient and reactions contributing more than 1% for inclusion for a given species.

6.4 Proposed Reduced Chemical Kinetics of the $\text{N}_2/\text{O}_2/\text{NH}_3$

Discharges

For $\text{N}_2/\text{O}_2/\text{NH}_3$ mixtures, we have obtained two sets of simplified plasma chemistry consisting of 31 species and 79 reactions as the Simplified Chemistry 1 (S1) and 33 species and 87 reactions as the Simplified Chemistry 2 (S2). [Table 8](#) summarizes the comparison of the selected species in the two sets of simplified chemistry. [Table 9](#) summarizes the comparison of the accuracy and computational time using 1-D fluid modeling with various levels of chemical kinetics. The accuracy of the number density of the selected species is quantified by the root mean squared error (RMSE) as

$$RMSE = \sqrt{\frac{1}{N} \sum_{i=1}^N \left(\frac{n_{is} - n_{ic}}{n_{ic}} \right)^2} \times 100\% \quad (20)$$

where N denotes the total number of selected species in the simplified chemistry; n_{ic} denotes the number density of the i^{th} selected species obtained using the more complete chemistry; and n_{is} denotes the number density of the i^{th} selected species obtained using the simplified chemistry. The calculated results show that the root mean squared error of the selected species is strikingly less than 1.8%, and the computation time is reduced by a factor of 2.1 using the Simplified Chemistry 2 compared to that using the more complete chemistry. The computational efficiency is improved because the numbers of species and reactions are reduced dramatically. In addition, [Figure 40](#) shows that the current densities obtained using the Simplified Chemistry 1 and 2 are both in agreement with the current densities using the more complete chemistry. Thus, the current simplified chemistry enables the accurate reproduction of the current density profile of the complete chemistry. [Figure 41](#) and [Figure 42](#) compare the densities of the charged and excited species obtained from calculations using the complete chemistry and the simplified chemistry. In general, the Simplified Chemistry 1 and 2 are both able to capture the change in the density of the selected species as a function of the ammonia concentration with an error that could be ignored in practice. Finally, the Simplified Chemistry 2 is chosen as the reduced chemical kinetics for modeling $N_2/O_2/NH_3$ AP-DBD because of its better accuracy and acceptable computational time. This Simplified Chemistry 2 will be applied for the simulation of a practical two-dimensional $N_2/O_2/NH_3$ AP-DBD jet that one could expect it can save an appreciable amount of computational time.

6.5 Summary

In this chapter, the one-dimensional self-consistent fluid modeling of a planar atmospheric-pressure $N_2/O_2/NH_3$ dielectric barrier discharge with reduced chemical kinetics is performed and compared with the results of modeling with a more complete representation of the kinetics. The reduced chemical kinetics is justified by the good agreement of the simulation results with the results obtained using the more complete chemical kinetics. The complete chemistry, including 48 species and 235 reactions, has been reduced to 33 species and 87 reactions with only slight deviation in the simulation results. With the choice of this set of reduced chemical kinetics, the computational time decreases 2.1 times with essentially the same electrical properties and less than 1.8% root mean squared error for the selected species compared to that using the complete chemistry, when oxygen (impurity) is fixed at 30 ppm and ammonia varies in the range from 0-1%. This set of simplified chemistry will be used in a more detailed parametric study of both 1-D fluid modeling and a 2-D AP-DBD jet considering gas flow and gas discharge simultaneously [64].

Chapter 7 Conclusion and Recommendations for Future Work

In this chapter, we present the major findings in this thesis and the followed by the recommendations of future work in the research of $N_2/O_2/NH_3$ discharge.

7.1 Summaries of the Thesis

7.1.1 One-Dimensional Fluid Modeling of Nitrogen/Ammonia Dielectric Barrier

Discharge

In this study, we have employed one-dimensional self-consistent fluid modeling for simulating a parallel-plate atmospheric-pressure dielectric barrier discharge (AP-DBD, driven by a 30 kHz power source) of nitrogen added with small amount of ammonia (0-2%). Major findings can be summarized as follows:

1. The plasma chemistry of N_2/NH_3 , including 23 species and 141 reactions, was developed to describe the behavior of the gas discharge very well. A 1-D fluid modeling with the N_2/NH_3 plasma chemistry was validated by good agreement between predicted and experimental current densities.
2. The discharges of N_2 mixed with NH_3 (0-2%) are all typical Townsend-like discharges because the ions always outnumber the electrons to a large extent which leads to no quasi-neutral region in the gap throughout the cycle.
3. N_2^+ and N_4^+ are found to be the most abundant charged species during and after the breakdown process, respectively, like a pure nitrogen DBD. NH_4^+ increases rapidly initially, respectively, with increasing addition of NH_3 and levels off eventually.

4. N is the most dominant neutral species, except the background species, N_2 and NH_3 , and NH_2 and H are the second dominant species, which increase with increasing added NH_3 in the range of added ammonia. Abundant H, NH, and NH_2 in a discharge of N_2 mixed with NH_3 may play a critical role in some applications which require functional group incorporation.
5. The primary source of NH_2 generation is by electron impact dissociation with ammonia because of low threshold energy of 5.72 eV for dissociation. N generation is by electron impact dissociation with nitrogen. The dominant reaction channels for generating the dominant species are summarized in [Table 10](#).

7.1.2 Parametric Study of One-Dimensional Fluid Modeling of Nitrogen/Ammonia

Dielectric Barrier Discharge



In this study, we have employed one-dimensional self-consistent fluid modeling in simulating a parallel-plate atmospheric-pressure dielectric barrier discharge (driven by a sinusoidal voltage source) of nitrogen mixed with a small amount of ammonia. An extensive parametric study of N_2/NH_3 AP-DBD by varying the five major parameters (amplitude of voltage, frequency, dielectric material, dielectric thickness, and gap distance) has been performed systematically. Major findings can be summarized as follows:

1. Discharge current density and densities of charged and neutral species increase with: 1) increasing amplitude of applied voltage; 2) increasing frequency of applied voltage; 3) increasing permittivity of dielectric material; 4) decreasing dielectric thickness; 5) increasing gap distance from 0.1 to 1.2 mm.
2. All of the simulated results demonstrate that the discharges are typically

Townsend-like because the ions outnumber the electrons and the electric field across the gap is distorted only slightly by the charged particles during the breakdown.

3. N_2^+ , N_4^+ and NH_4^+ are found to be the most dominant ions species; N , N_2^* , NH_2 , and H are found to be the most dominant neutral species, except background gas, N_2 and NH_3 . These results are important in understanding the mechanism of several recent applications of improvement of biocompatibility of PLA by applying N_2/NH_3 dielectric barrier discharge jet.

7.1.3 One-Dimensional Fluid Modeling of Nitrogen/Ammonia Dielectric Barrier

Discharge Considering Oxygen Impurity

In this study, we investigate the mechanism of the light emissions (NO- γ , NO- β and N₂-SPS) in a planar N_2/NH_3 AP-DBD considering the oxygen impurity level. Major findings can be summarized as follows:

1. The plasma chemistry of $N_2/O_2/NH_3$, including 48 species and 235 reactions, was developed to describe the behavior of the gas discharge very well. A self-consistent 1-D fluid modeling with the $N_2/O_2/NH_3$ plasma chemistry was validated by reasonable agreement with the OES measurements and discharge current densities.
2. All of the predicted intensities of NO- γ , NO- β and N₂-SPS decreased with increasing NH_3 due to various reaction mechanisms. The former is due to the loss of N₂(A) and NO(A) by the reaction of NH_3 with N₂(A) and NO(A), respectively. The decrease of NO- β is due to the depletion of N and O because of NH_3 , and the decrease of N₂-SPS is due to electron attachment to NH_3 and a weaker metastable-metastable associative ionization of N₂.

3. All of the simulated results demonstrate that the discharges are typically Townsend-like because the ions outnumber the electrons and the electric field across the gap is distorted only slightly by the charged particles during the breakdown.
4. The power absorbed by the ions for the N₂/O₂ DBD are smaller compared to that for the N₂/O₂ DBD with a small amount of ammonia addition because N₂⁺ and N₄⁺ are exchanged with NH₃ indirectly and effectively to form NH₄⁺ which is lighter compare to N₂⁺ and N₄⁺. In addition, the power absorbed by the electrons decreases with increasing NH₃ because the number of electron decreases with increasing NH₃. This finding reveals that the light emission weakens with increasing NH₃ because there are fewer electrons that can excite the molecules.
5. The amount of atomic oxygen decreases rapidly with increasing ammonia addition, which leads to less etching on a PLA surface and is in good agreement with the trend of the experimental observations [26]. In addition, the number density of atomic oxygen is decreased by approximately two to three orders of magnitude with an increase in NH₃ concentration from 0% to 1%, mainly through the destructive reactions R108 (N₂(A)+O→O(¹S)+N₂), R156 (N+O+N₂→NO(B)+N₂) and R157 (N+O+NH₃→NO(B)+NH₃).
6. NH₂ is generated by the reactions R60 (NH₃⁺+NH₃→NH₂⁺+H₂+NH₂) and R112 (N₂(A)+NH₃→N₂+NH₂+H), and it is lost by the reactions R183 (NH₂+N→N₂+2H), R186 (NH₂+NH→H+N₂H₂), and R188 (NH₂+H+N₂→NH₃+N₂). The amounts of NH and NH₂ initially increases up to 0.1% upon addition of NH₃ and levels off afterwards. The dominant reaction channels for generating the dominant species are summarized in Table 11.

7.1.4 A Reduced Chemical Kinetics for Atmospheric-Pressure

Nitrogen/Oxygen/Ammonia Dielectric Barrier Discharge

In this study, one-dimensional self-consistent fluid modeling of a planar atmospheric-pressure $N_2/O_2/NH_3$ dielectric barrier discharge with reduced chemical kinetics is performed and compared with that with a more complete one. Major findings can be summarized as follows:

1. The reduced chemical kinetics is justified by the good agreement of the simulation results with the results obtained using the complete chemical kinetics. The complete chemistry, including 48 species and 235 reactions, has been reduced to 33 species and 87 reactions with only slight deviation in the simulation results.
2. With the choice of this set of reduced chemical kinetics, the computational time is 2.1 times shorter with essentially the same electrical properties and less than 1.8% root mean squared error for the selected species compared to using the complete chemistry, when oxygen (impurity) is fixed at 30 ppm and ammonia varies in the range from 0-1%.

7.2 Recommendations for Future Work

The recommendations for future work are summarized as follows:

1. To study the effect of operating parameters of 1-D fluid modeling of $N_2/O_2/NH_3$ AP-DBD including voltage amplitudes of power source, driving frequencies of power source, dielectric materials, dielectric thickness, and discharge gas distances, among others.
2. In Chapter 6, one can apply the set of the Simplified Chemistry 2 for the realistic modeling of a two-dimensional AP-DBD jet considering gas flow and gas

discharge at the same time [64].

3. To perform parametric studies of $N_2/O_2/NH_3$ AP-DBDJ including the voltage amplitudes of power source, the driving frequencies of power source, the dielectric materials, the dielectric thickness and the discharge gap distances, to name a few, which affect the properties of species on the surface of PLA in the post-discharge jet region.
4. To perform 1-D and 2-D fluid modeling to reach a truly quasi-steady-state using a recently developed temporal multi-scale method in our group by Gu and Wu [personal communication, 2013].



References

- [1] F. Barbir and T. Gomez, *Int. J. Hydrogen Energy* **22**, 1027 (1997)
- [2] J. Klemberg-Sapieha, O. Kuttel, L. Martinu, and M. Wertheimer, *J. Vac. Sci. Technol. A* **9**, 2975 (1991)
- [3] M. Losurdo, P. Capezzuto, G. Bruno, and E. Irene, *Phys. Rev. B* **58**, 15878 (1998)
- [4] R.A. Arakoni, A.N. Bhoj, and M.J. Kushner, *J. Phys. D: Appl. Phys.* **40**, 2476 (2007)
- [5] P.R. McCurdy, C.I. Butoi, K.L. Williams, and E.R. Fisher, *J. Phys. Chem. B* **103**, 6919 (1999)
- [6] Y.B. Golubovskii, V.A. Maiorov, J. Behnke, and J.F. Behnke, *J. Phys. D: Appl. Phys.* **35**, 751 (2002)
- [7] Y. Choi, J. Kim, and Y. Hwang, *Thin solid films* **506**, 389 (2006)
- [8] E. Panousis, L. Papageorghiou, N. Spyrou, J.F. Loiseau, B. Held, and F. Clement, *J. Phys. D: Appl. Phys.* **40**, 4168 (2007)
- [9] F. Massines, A. Rabehi, P. Decomps, R.B. Gadri, P. Segur, and C. Mayoux, *J. Appl. Phys.* **83**, 2950 (1998)
- [10] F. Tochikubo, T. Chiba, and T. Watanabe, *Jpn. J. Appl. Phys.* **38**, 5244 (1999)
- [11] Y.B. Golubovskii, V.A. Maiorov, J. Behnke, and J.F. Behnke, *J. Phys. D: Appl. Phys.* **36**, 39 (2003)
- [12] Q. Wang, J. Sun, and D. Wang, *Phys. Plasmas* **16**, 043503 (2009)
- [13] N. Naudé, J.P. Cambronne, N. Gherardi, and F. Massines, *J. Phys. D: Appl. Phys.* **38**, 530 (2005)
- [14] F. Massines, N. Gherardi, N. Naudé, and P. Ségur, *Plasma Phys. Control Fusion* **47**, B577 (2005)
- [15] H. Luo, Z. Liang, X. Wang, Z. Guan, and L. Wang, *J. Phys. D: Appl. Phys.* **43**,

155201 (2010)

- [16] M. Mao and A. Bogaerts, *J. Phys. D: Appl. Phys.* **43**, 205201 (2010)
- [17] W.D. Yang, P.N. Wang, Z.P. Liu, L. Mi, S.C. Chen, and F.M. Li, *J. Phys. D: Appl. Phys.* **33**, 3223 (2000)
- [18] H. Nagai, S. Takashima, M. Hiramatsu, M. Hori, and T. Goto, *J. Appl. Phys.* **91**, 2615 (2002)
- [19] Y. Morikawa, S. Yasunami, W. Chen, T. Hayashi, and T. Uchida, *J. Vac. Sci. Technol. A* **19**, 1747 (2001)
- [20] S. Panda, R. Wise, A. Mahorowala, V. Balasubramaniam, and K. Sugiyama, *J. Vac. Sci. Technol. B* **23**, 900 (2005)
- [21] M. Nishida, K. Yukimura, S. Kambara, and T. Maruyama, *J. Appl. Phys.* **90**, 2672 (2001)
- [22] G. Wan, P. Yang, R.K.Y. Fu, Z.Q. Yao, N. Huang, and P.K. Chu, *J. Vac. Sci. Technol. A* **23**, 1346 (2005)
- [23] M. Akhrrarov, B. Vasil'ev, A.Z. Grasyuk, and A. Yastrebkov, *Sov. J. Quant. Electron* **12**, 1326 (1982)
- [24] C.P. Klages and A. Grishin, *Plasma Process Polymer* **5**, 368 (2008)
- [25] Y.W. Yang, C.L. Kuo, C.C. Wen, J.Y. Wu, H.Y. Huang, M.H. Chiang, and J.S. Wu, in *Proceedings of the 7th International Conference on Flow Dynamics*, Sendai, Japan (2010)
- [26] Y.W. Yang, C.L. Kuo, C.C. Wen, J.Y. Wu, H.Y. Huang, M.H. Chiang, and J.S. Wu, in *Proceedings of the 8th International Conference on Flow Dynamics*, Sendai, Japan (2011)
- [27] A. Fridman, A. Chirokov, and A. Gutsol, *J. Phys. D: Appl. Phys.* **38**, R1 (2005)
- [28] U. Kogelschatz, B. Eliasson, and W. Egli, *Pure Appl. Chem.* **71**, 1819 (1999)
- [29] F. Massines, N. Gherardi, N. Naudé, and P. Ségur, *Eur. Phys. J. Appl. Phys.* **47**,

22805 (2009)

- [30] Kanazawa, M. Kogoma, T. Moriwaki, and S. Okazaki, *J. Phys. D: Appl. Phys.* **21**, 838 (1988)
- [31] U. Kogelschatz, *J. Phys. Conf. Ser.* **257**, 012015 (2010)
- [32] A. Sublet, C. Ding, J.L. Dorier, C. Hollenstein, P. Fayet, and F. Coursimault, *Plasma Sources Sci. Technol.* **15**, 627 (2006)
- [33] N. Gherardi, E. Gat, F. Massines, S. Lemoing, and P. Ségur, *Proc. 15th Int. Symp. on Plasma Chemistry (Orleans, France)*, **1**, 97 (2001)
- [34] R. Brandenburg, V.A. Maiorov, Y.B. Golubovskii, H.E. Wagner, J. Behnke, and J.F. Behnke, *J. Phys. D: Appl. Phys.* **38**, 2187 (2005)
- [35] F. Massines, G. Gouda, N. Gherardi, M. Duran, and E. Croquesel, *Plasmas Polym.* **6**, 35 (2001)
- [36] H.E. Wagner, R. Brandenburg, K.V. Kozlov, A.M. Morozov, and P. Michel, *Contrib. Plasma Phys.* **45**, 338 (2005)
- [37] G. Dilecce, P.F. Ambrico, and S.D. Benedictis, *Plasma Sources Sci. Technol.* **16**, 511 (2007)
- [38] F. Massines, P. Ségur, N. Gherardi, C. Khamphan, and A. Ricard, *Surf. Coat. Technol.* **174-175**, 8 (2003)
- [39] K.M. Lin, C.T. Hung, F.N. Hwang, M.R. Smith, Y.W. Yang, and J.S. Wu, *Comput. Phys. Commun.* **183**, 1225 (2012)
- [40] F.L. Li, K.M. Lin, Y.W. Yang, C.T. Hung, J.S. Wu, and J.P. Yu, *Plasma Chem. Plasma Process* **32**, 547 (2012)
- [41] F.L. Li, Y.W. Yang, K.M. Lin, and J.S. Wu, Paper presented at the *9th International Conference on Flow Dynamics*, Sendai, Japan (2012)
- [42] I.P. Androulakis, *AIChE Journal* **46**, 361 (2000)
- [43] D.X. Liu, P. Bruggeman, F. Iza, M.Z. Rong, and M.G. Kong, *Plasma Sources Sci.*

- Technol. **19**, 025018 (2010)
- [44] D.X. Liu, M.Z. Rong, X.H. Wang, F. Iza, M. G. Kong, and P. Bruggeman, *Plasma Process. Polym.* **7**, 846 (2010)
- [45] G.Y. Park, Y.J. Hong, H.W. Lee, J. Y. Sim, J.K. Lee, *Plasma Process. Polym.* **7**, 281 (2010)
- [46] R.J. Kee, F.M. Rupley, J.A. Miller, *et al.*, CHEMKIN Release 4.1.1, Reaction Design, San Diego, CA (2007)
- [47] C.T. Hung, Y.M. Chiu, F.N. Hwang, M.H. Chiang, J.S. Wu, and Y.C. Wang, *Plasma Chem. Plasma Process.* **31**, 1 (2011)
- [48] G. Grubert, M. Becker, and D. Loffhagen, *Phys. Rev. E* **80**, 036405 (2009)
- [49] G. Hagelaar and L. Pitchford, *Plasma Sources Sci. Technol.* **14**, 722 (2005)
- [50] R.J. LeVeque, *Finite volume methods for hyperbolic problems*, Cambridge University Press, Cambridge (2002)
- [51] D. Scharfetter and H. Gummel, *IEEE Trans. Electron Dev.* **16**, 64 (1969)
- [52] S. Balay, K. Buschelman, W.D. Gropp, D. Kaushik, M.G. Knepley, L.C. McInnes, B.F. Smith, and H. Zhang, (2009) <http://www.mcs.anl.gov/petsc>
- [53] Y. Saad and M.H. Schultz, *SIAM J. Sci. Stat. Comput.* **7**, 856 (1986)
- [54] H.W. Ellis, R.Y. Pai, E.W. McDaniel, E.A. Mason, and L.A. Viehland, *At. Data Nucl. Data Tables* **17**, 177 (1976)
- [55] H.W. Ellis, E.W. McDaniel, D.L. Albritton, L.A. Viehland, S.L. Lin, and E.A. Mason, *At. Data Nucl. Data Tables* **22**, 179 (1978)
- [56] R.B. Bird, W.E. Stewart, and E.N. Lightfoot, *Transport Phenomena*, John Wiley & Sons, New York, pp 525 (2007)
- [57] M.H. Chiang, K.C. Liao, I.M. Lin, C.C. Lu, H.Y. Huang, C.L. Kuo, J.S. Wu, C.C. Hsu, and S.H. Chen, *Plasma Chem. Plasma Process.* **30**, 553 (2010)
- [58] E. Panousis, A. Ricard, J.F. Loiseau, F. Clement, and B. Held, *J. Phys. D: Appl. Phys.* **42**, 205201 (2009)
- [59] N. Leoni and B. Paradkar, in *Proceedings of NIP 25: International Conference*

on Digital Printing Technologies, Louisville, KY, 2009

- [60] F. Tochikubo, S. Uchida, H. Yasui, and K. Sato, *Jpn. J. Appl. Phys.* **48**, 076507 (2009)
- [61] A. Fateev, F. Leipold, Y. Kusano, B. Stenum, E. Tsakadze, and H. Bindslev, *Plasma Process. Polym.* **2**, 193 (2005)
- [62] K.W. Cheng, C.T. Hung, K.M. Lin, Y.M. Chiu, J.S. Wu, and J.P. Yu, *Jpn. J. Appl. Phys.* **51**, 116001 (2012)
- [63] M. Moravej, X. Yang, R.F. Hicks, J. Penelon, and S.E. Babayan, *J. Appl. Phys.* **99**, 093305 (2006)
- [64] K.M. Lin, M.H. Hu, C.T. Hung, J.S. Wu, F. N. Hwang, Y.S. Chen, and G. Cheng, *Comput. Phys. Commun.* **183**, 2550 (2012)
- [65] M. Hayashi, In: Capitelli M, Bardley J (eds) *Nonequilibrium Processes in Partially Ionized Gases*, New York: Plenum, pp 333-340 (1990)
- [66] D.X.Liu, *Plasma Sources Sci. Technol.* **19**, 025018 (2010)
- [67] H. Mätzing, *Chemical Kinetics of Flue Gas Cleaning by Irradiation with Electrons*, in *Adv. Chem. Phys.* 80 (eds I Prigogine and S A Rice), John Wiley & Sons (2007)
- [68] E. Tatarova, F.M. Dias, E. Felizardo, J. Henriques, M.J. Pinheiro, et al., *J. Appl. Phys.* **108**, 123305 (2010)
- [69] B. Gordiets, C.M. Ferreira, M.J. Pinheiro, and A. Ricard, *Plasma Sources Sci. Technol.* **7**, 363 (1998)
- [70] D.Smith, N.G. Adams, and T.M. Miller, *J. Chem. Phys.* **69**, 308 (1978)
- [71] R.Dorai and M.J., *Kushner J. Phys. D: Appl. Phys.* **36**, 666 (2003)
- [72] F.Tochikubo, *Jpn. J. Appl. Phys.* **41**, 844 (2002)
- [73] I.A. Kossyi, A.Y. Kostinsky, A.A. Matveyev, and V.P. Silakov, *Plasma Sources Sci. Technol.* **1**, 207 (1992)
- [74] J.T. Herron, *J. Phys. Chem. Ref. Data* **28**, 1453 (1999)

- [75] Y. Mirokin and G. Mallard, The NIST Chemical Kinetics Database (1998)
- [76] C.D. Pintassilgo, J. Phys. D: Appl. Phys. **38**, 417 (2005)
- [77] A.N. Bhoj and M.J. Kushner, Plasma Sources Sci. Technol. **17**, 035025 (2008)
- [78] M. Capitelli, C.M. Ferreira, B.F. Gordiets, and A.I. Osipov, Plasma Phys. Control. Fusion **43**, 371 (2001)
- [79] G.E. Gadd and T.G. Slinger, J. Chem. Phys. **92**, 2194 (1990)
- [80] BOLSIG⁺ [<http://www.bolsig.laplace.univ-tlse.fr/>]



Tables

Table 1. Order of magnitude of the different species in the two well characterized homogeneous DBD regimes [29].

	APTD - TDBD	APGD - GDBD
Electron density maximum (cm^{-3})	10^7 - 10^8	10^{10} - 10^{11}
Ions density maximum (cm^{-3})	10^{10}	10^{11}
Neutral plasma formation ($n_+ = n_-$)	No	Yes (positive column)
Metastable of the dilution gas	10^{13}	10^{11}
Current density (mA/cm^2)	0.1 to 10	10 to 100
Gas voltage variation around the current maximum	Constant (Townsend plateau)	Decrease (cathode fall formation)
Dilution gases	N_2 , Air, N_2O	Penning mixture in He, Ar, Ne
Typical gas gap	<2mm	>2mm
Typical frequency range	<10kHz	> 1kHz
Power for a 10kHz excitation	Some W/cm^3	Some $0.1\text{W}/\text{cm}^3$
Solutions to observe micro-discharge	Current (Cf Fig.3), optical method	Photomultiplier, ICCD



Table 2. Electron-Impact Collisions include N₂/NH₃ plasma chemistry. All rate constants are adopted from [49][65].

No	Reaction	Threshold energy(eV)	Reaction type	Reference
1	$NH_3 + e^- \rightarrow NH_3 + e^-$	0.0	Momentum	[16]
2	$NH_3 + e^- \rightarrow NH_3 + e^-$	0.12	Vibrational excitation	[16]
3	$NH_3 + e^- \rightarrow NH_3 + e^-$	0.2	Vibrational excitation	[16]
4	$NH_3 + e^- \rightarrow NH_3 + e^-$	0.42	Vibrational excitation	[16]
5	$NH_3 + e^- \rightarrow NH_2 + H + e^-$	5.72	Dissociation	[16]
6	$NH_3 + e^- \rightarrow NH + H + H + 2e^-$	8.65	Dissociation	[16]
7	$NH_3 + e^- \rightarrow NH_3^+ + 2e^-$	10.2	Ionization	[16]
8	$NH_3 + e^- \rightarrow NH_2^+ + H + 2e^-$	16.0	Dissociative ionization	[16]
9	$NH_2 + e^- \rightarrow NH_2 + e^-$	0.0	Momentum	[16]
10	$NH_2 + e^- \rightarrow NH_2 + e^-$	0.12	Vibrational excitation	[16]
11	$NH_2 + e^- \rightarrow NH_2 + e^-$	0.2	Vibrational excitation	[16]
12	$NH_2 + e^- \rightarrow NH_2 + e^-$	0.42	Vibrational excitation	[16]
13	$NH_2 + e^- \rightarrow NH + H + e^-$	5.72	Dissociation	[16]
14	$NH_2 + e^- \rightarrow N + H + H + 2e^-$	8.65	Dissociation	[16]
15	$NH_2 + e^- \rightarrow NH_2^+ + 2e^-$	11.14	Ionization	[16]
16	$NH_2 + e^- \rightarrow NH^+ + H + 2e^-$	17.6	Dissociative ionization	[16]

17	$NH + e^- \rightarrow NH + e^-$	0.0	Momentum	[16]
18	$NH + e^- \rightarrow NH + e^-$	0.12	Vibrational excitation	[16]
19	$NH + e^- \rightarrow NH + e^-$	0.2	Vibrational excitation	[16]
20	$NH + e^- \rightarrow NH + e^-$	0.42	Vibrational excitation	[16]
21	$NH + e^- \rightarrow N + H + e^-$	5.72	Dissociation	[16]
22	$NH + e^- \rightarrow NH^+ + 2e^-$	13.49	Ionization	[16]
23	$N_2 + e^- \rightarrow N_2 + e^-$	0.0	Momentum	[16]
24	$N_2 + e^- \rightarrow N_2 + e^-$	0.02	Rotational excitation	[16]
25	$N_2 + e^- \rightarrow N_2 + e^-$	0.291	Vibrational excitation	[16]
26	$N_2 + e^- \rightarrow N_2 + e^-$	0.59	Vibrational excitation	[16]
27	$N_2 + e^- \rightarrow N_2 + e^-$	0.88	Vibrational excitation	[16]
28	$N_2 + e^- \rightarrow N_2 + e^-$	1.47	Vibrational excitation	[16]
29	$N_2 + e^- \rightarrow N_2 + e^-$	1.76	Vibrational excitation	[16]
30	$N_2 + e^- \rightarrow N_2 + e^-$	2.06	Vibrational excitation	[16]
31	$N_2 + e^- \rightarrow N_2 + e^-$	2.35	Vibrational excitation	[16]
32	$N_2 + e^- \rightarrow N_2^* + e^-$	6.17	Electronic excitation	[16]
33	$N_2 + e^- \rightarrow N_2^* + e^-$	7.0	Electronic Excitation	[16]
34	$N_2 + e^- \rightarrow N_2^* + e^-$	7.35	Electronic Excitation	[16]
35	$N_2 + e^- \rightarrow N_2^* + e^-$	8.16	Electronic Excitation	[16]



36	$N_2 + e^- \rightarrow N_2^* + e^-$	8.4	Electronic Excitation	[16]
37	$N_2 + e^- \rightarrow N_2^* + e^-$	11.03	Electronic Excitation	[16]
38	$N_2 + e^- \rightarrow N + N + e^-$	13.0	Dissociation	[16]
39	$N_2 + e^- \rightarrow N_2^+ + 2e^-$	15.8	Ionization	[16]
40	$N + e^- \rightarrow N + e^-$	0.0	Momentum	[16]
41	$N + e^- \rightarrow N^* + e^-$	2.38	Electronic Excitation	[16]
42	$N + e^- \rightarrow N^* + e^-$	3.58	Electronic Excitation	[16]
43	$N + e^- \rightarrow N^+ + 2e^-$	14.54	Ionization	[16]
44	$H_2 + e^- \rightarrow H_2 + e^-$	0.0	Momentum	[16]
45	$H_2 + e^- \rightarrow H_2 + e^-$	0.044	Rotational excitation	[16]
46	$H_2 + e^- \rightarrow H_2 + e^-$	0.073	Rotational excitation	[16]
47	$H_2 + e^- \rightarrow H_2 + e^-$	0.516	Vibrational excitation	[16]
48	$H_2 + e^- \rightarrow H_2 + e^-$	1.0	Vibrational excitation	[16]
49	$H_2 + e^- \rightarrow H_2 + e^-$	1.5	Vibrational excitation	[16]
50	$H_2 + e^- \rightarrow H_2 + e^-$	11.3	Electronic Excitation	[16]
51	$H_2 + e^- \rightarrow H_2 + e^-$	11.75	Electronic Excitation	[16]
52	$H_2 + e^- \rightarrow H_2 + e^-$	11.8	Electronic Excitation	[16]
53	$H_2 + e^- \rightarrow H_2 + e^-$	12.4	Electronic Excitation	[16]
54	$H_2 + e^- \rightarrow H_2 + e^-$	14.0	Electronic Excitation	[16]



55	$H_2 + e^- \rightarrow H + H + e^-$	8.9	Dissociation	[16]
56	$H_2 + e^- \rightarrow H_2^+ + 2e^-$	15.43	Ionization	[16]



Table 3. Ion-Molecular Collisions include N₂/NH₃ plasma chemistry. T_e is the electron temperature, and T_g is the background gas temperature. Both are in Kelvin.

No	Reaction	Rate constant (cm ³ s ⁻¹)	Reference
1	$N_2^+ + N \rightarrow N^+ + N_2$	5.0×10^{-12}	[16]
2	$N_2^+ + N^* \rightarrow N^+ + N_2$	1.0×10^{-10}	[16]
3	$N_2^+ + N_2^* \rightarrow N_2^+ + N_2$	1.0×10^{-9}	[16]
4	$N_2^+ + N_2^* \rightarrow N_2^+ + N_2$	1.0×10^{-9}	[16]
5	$N_4^+ + e^- \rightarrow N_2^* + N_2$	$2.0 \times 10^{-6} (T_g / T_e)^{0.5}$	[7]
6	$N^+ + N \rightarrow N^+ + N$	1.0×10^{-9}	[16]
7	$N^+ + N^* \rightarrow N^+ + N$	1.0×10^{-9}	[16]
8	$N^+ + N_2 \rightarrow N^+ + N_2$	1.0×10^{-9}	[16]
9	$N^+ + N_2^* \rightarrow N^+ + N_2$	1.0×10^{-9}	[16]
10	$H_2^+ + NH \rightarrow NH^+ + H_2$	5.0×10^{-10}	[16]
11	$H_2^+ + NH \rightarrow NH_2^+ + H$	5.0×10^{-11}	[16]
12	$H_2^+ + NH_2 \rightarrow NH_2^+ + H_2$	5.0×10^{-10}	[16]
13	$H_2^+ + NH_2 \rightarrow NH_3^+ + H$	5.0×10^{-11}	[16]
14	$H_2^+ + NH_3 \rightarrow NH_3^+ + H_2$	5.7×10^{-9}	[16]
15	$H_2^+ + NH_3 \rightarrow NH_4^+ + H$	5.0×10^{-11}	[16]
16	$H^+ + NH_3 \rightarrow NH_3^+ + H$	5.0×10^{-11}	[16]

17	$H^+ + NH_2 \rightarrow NH_2^+ + H$	5.0×10^{-11}	[16]
18	$H^+ + NH \rightarrow NH^+ + H$	5.0×10^{-11}	[16]
19	$NH^+ + NH_3 \rightarrow NH_3^+ + NH$	2.4×10^{-9}	[16]
20	$NH^+ + NH_3 \rightarrow NH_4^+ + N$	1.8×10^{-9}	[16]
21	$NH^+ + H_2 \rightarrow NH_2^+ + H$	1.0×10^{-9}	[16]
22	$NH_2^+ + NH_3 \rightarrow NH_3^+ + NH_2$	2.2×10^{-9}	[16]
23	$NH_2^+ + NH_3 \rightarrow NH_4^+ + NH$	2.2×10^{-9}	[16]
24	$NH_2^+ + H_2 \rightarrow NH_3^+ + H$	1.0×10^{-9}	[16]
25	$NH_3^+ + NH_3 \rightarrow NH_4^+ + NH_2$	2.2×10^{-9}	[16]
26	$NH_3^+ + H_2 \rightarrow NH_4^+ + H$	4.0×10^{-13}	[16]
27	$NH_3^+ + H_2 \rightarrow H_2^+ + NH_3$	9.63×10^{-13} $(T_g / 298)^{-0.25} \exp(-14.6 / T_g)$	[16]
28	$NH_3^+ + NH_3 \rightarrow H^+ + NH_2 + NH_3$	6.87×10^{-10} $(T_g / 298)^{-0.17} \exp(-4.6 / T_g)$	[16]
29	$NH_3^+ + H_2 \rightarrow H_2^+ + NH_2 + H$	2.18×10^{-9} $(T_g / 298)^{-0.2} \exp(-9.9 / T_g)$	[16]
30	$NH_3^+ + NH_3 \rightarrow NH_2^+ + H_2 + NH_2$	6.12×10^{-7} $(T_g / 298)^{-0.44} \exp(-3.8 / T_g)$	[16]
31	$NH_3^+ + H_2 \rightarrow H^+ + NH_3 + H$	8.46×10^{-10} $(T_g / 298)^{-0.39} \exp(-14.8 / T_g)$	[16]
32	$NH_4^+ + e^- \rightarrow NH_3 + H$	$9.0 \times 10^{-7} T_e^{-0.6}$	[4]

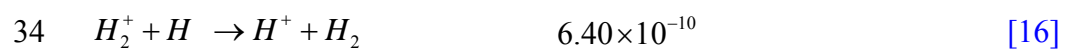
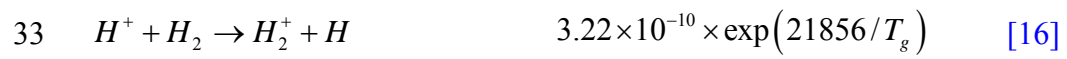


Table 4. Neutral-Neutral Collisions include N₂/NH₃ plasma chemistry. The rate constants are calculated by $k = k_0 \times (T_g / 298)^n \times \exp(-E_a / RT_g)$ where T_g is the background gas temperature (K).

No	Reaction	Rate constant			Reference
		k ₀ (cm ³ s ⁻¹)	n	E _a /R (K)	
1	$NH_3 + H \rightarrow H_2 + NH_2$	1.34×10^{-10}	0	7352	[16]
2	$NH_3 + NH + H_2 \rightarrow N_2H_4 + H_2$	5.0×10^{-35}	0	0	[16]
3	$NH_2 + H \rightarrow H_2 + NH$	4.81×10^{-12}	0	0	[16]
4	$NH_2 + H_2 \rightarrow H + NH_3$	2.09×10^{-12}	0	4277	[16]
5	$NH_2 + NH_2 \rightarrow H_2 + N_2H_2$	8.31×10^{-11}	0	0	[16]
6	$NH_2 + NH_2 \rightarrow NH_3 + NH$	8.31×10^{-11}	0	5100	[16]
7	$NH_2 + N \rightarrow N_2 + H + H$	1.2×10^{-10}	0	0	[16]
8	$NH_2 + NH \rightarrow H + N_2H_2$	2.49×10^{-9}	-0.5	0	[16]
9	$NH_2 + NH \rightarrow N_2H_3$	1.16×10^{-10}	0	0	[16]
10	$NH + N \rightarrow N_2 + H$	2.5×10^{-11}	0	0	[16]
11	$NH_2 + NH + H_2 \rightarrow NH_3 + H_2$	6.06×10^{-30}	0	0	[16]
12	$NH + H \rightarrow H_2 + N$	5.98×10^{-11}	0	166	[16]
13	$NH + H_2 \rightarrow H + NH_2$	5.96×10^{-11}	0	7782	[16]
14	$NH + NH \rightarrow N_2 + H + H$	1.16×10^{-9}	0	0	[16]

15	$NH + NH \rightarrow N_2H_2$	3.49×10^{-12}	0	0	[16]
16	$NH + NH \rightarrow NH_2 + N$	1.40×10^{-14}	2.89	-1015	[16]
17	$N + H_2 \rightarrow NH + H$	2.66×10^{-10}	0	12609	[16]
18	$H + H + NH_3 \rightarrow H_2 + NH_3$	1.40×10^{-31}	0	0	[16]
19	$H + H + NH_2 \rightarrow H_2 + NH_2$	1.40×10^{-31}	0	0	[16]
20	$N + H + NH_3 \rightarrow NH + NH_3$	5.00×10^{-32}	0	0	[16]
21	$H + N + H \rightarrow H + NH$	5.00×10^{-32}	0	0	[16]
22	$H + NH_2 + NH_3 \rightarrow NH_3 + NH_3$	6.00×10^{-30}	0	0	[16]
23	$N + H + H \rightarrow NH + H$	5.00×10^{-32}	0	0	[16]
24	$H + NH_2 + H \rightarrow H + NH_3$	6.00×10^{-30}	0	0	[16]
25	$H + NH_2 + NH_2 \rightarrow NH_3 + NH_2$	6.00×10^{-30}	0	0	[16]
26	$N_2H_2 + H \rightarrow N_2 + H + H_2$	4.53×10^{-13}	2.63	-115	[16]
27	$N_2H_2 + NH_2 \rightarrow N_2 + H + NH_3$	1.53×10^{-13}	4.05	-810.7	[16]
28	$N_2H_3 + H \rightarrow NH_2 + NH_2$	2.66×10^{-12}	0	0	[16]
29	$N_2H_3 + N_2H_3 \rightarrow NH_3 + NH_3 + N_2$	5.0×10^{-12}	0	0	[16]
30	$N_2H_3 + N_2H_3 \rightarrow N_2H_4 + N_2H_2$	2.0×10^{-11}	0	0	[16]
31	$N_2H_4 + N \rightarrow NH_2 + N_2H_2$	1.25×10^{-13}	0	0	[16]
32	$N_2H_4 + H \rightarrow N_2H_3 + H_2$	1.17×10^{-13}	0	1260.5	[16]
33	$N_2H_4 + NH_2 \rightarrow NH_3 + N_2H_3$	5.15×10^{-13}	0	0	[16]
34	$N_2H_2 + H \rightarrow N_2H + H_2$	8.31×10^{-11}	0	510	[16]

35	$N_2H_2 + NH \rightarrow N_2H + NH_2$	1.66×10^{-11}	0	510	[16]
36	$N_2H_2 + NH_2 \rightarrow N_2H + NH_3$	1.66×10^{-11}	0	510	[16]
37	$N_2H + H \rightarrow N_2 + H_2$	6.64×10^{-11}	0	1531	[16]
38	$N_2H + NH \rightarrow N_2 + NH_2$	8.31×10^{-11}	0	0	[16]
39	$N_2H + NH_2 \rightarrow N_2 + NH_3$	8.31×10^{-11}	0	0	[16]
40	$N_2^* + N_2 \rightarrow N_2 + N_2$	1.9×10^{-13}	0	0	[16]
41	$N_2^* + N \rightarrow N + N_2$	1.0×10^{-13}	0	0	[16]
42	$N_2^* + N^* \rightarrow N + N_2$	1.0×10^{-13}	0	0	[16]
43	$N^* + N_2 \rightarrow N + N_2$	2.0×10^{-14}	0	0	[16]
44	$N^* + N + NH_3 \rightarrow N_2^* + NH_3$	2.0×10^{-32}	0	0	[16]
45	$N + N + NH_3 \rightarrow N_2^* + NH_3$	1.0×10^{-32}	0	0	[16]
46	$N + N + NH_3 \rightarrow N_2 + NH_3$	1.0×10^{-32}	0	0	[16]
47	$N_2^* + N_2 \rightarrow N_2 + N_2^*$	1.36×10^{-9}	0	0	[16]
48	$N_2 + N_2 \rightarrow N + N + N_2$	4.29×10^{-10}	0	86460	[16]
49	$N_2^* + N_2^* \rightarrow N_4^+ + e^-$	2.0×10^{-10}	0	0	[7]
50	$H + H + N_2 \rightarrow H_2 + N_2$	1.9×10^{-31}	-1.32	0	[16]
51	$H + H + NH_3 \rightarrow H_2 + NH_3$	1.9×10^{-31}	-0.06	0	[16]

Table 5. The test grid convergence for $N_2/0.01\%NH_3$ AP-DBD as the applied voltage of 8 kV and the frequency of 30 kHz.

Cell No.	e^- (N/m^3)	NH_2^+ (N/m^3)	NH_4^+ (N/m^3)	N_2^+ (N/m^3)	H^+ (N/m^3)	N_2^* (N/m^3)	NH_2 (N/m^3)	N (N/m^3)	H (N/m^3)
60	8.95E+12	1.16E+12	2.69E+11	2.49E+15	3.15E+09	7.93E+16	9.86E+15	8.98E+18	9.01E+15
130	1.86E+13	2.52E+12	5.73E+11	5.68E+15	6.72E+09	1.54E+17	8.49E+15	7.97E+18	7.54E+15
370	1.90E+13	2.59E+12	5.92E+11	5.81E+15	6.92E+09	1.55E+17	8.58E+15	8.05E+18	7.61E+15



Table 6. Test conditions used for parametric study.

Amplitude (V_{amp})	Frequency (f)	Dielectric material* (ϵ)	Dielectric thickness (D_d)	Gap distance (D)
f: 30 kHz	V_{amp} : 8 kV	f: 30 kHz	f: 30 kHz	f: 30 kHz
D: 1 mm	D: 1 mm	V_{amp} : 8 kV	V_{amp} : 8 kV	V_{amp} : 8 kV
D_d : 1 mm	D_d : 1 mm	D: 1 mm	D: 1 mm	D_d : 1 mm
ϵ : quartz	ϵ : quartz	D_d : 1 mm	ϵ : quartz	ϵ : quartz
6-10 kV	10-100 kHz	Quartz & Ceramic	0.5-2 mm	0.1-1.2 mm

*Note that the measured relative permittivity of dielectric quartz and ceramic is 4.76 and 11.63 (F/m), respectively.



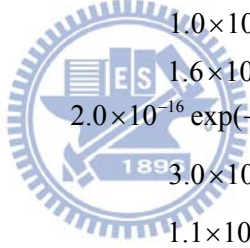
Table 7. Summary of N₂/O₂/NH₃ plasma chemistry.

No.	Reaction	Rate coefficient ^{a, b}	Threshold (eV)	Note ^c	Ref.
R1	$e + N \rightarrow N + e$	BOLSIG ⁺	0.0		[16]
R2	$e + N \rightarrow N(^2D) + e$	BOLSIG ⁺	2.38		[16]
R3	$e + N \rightarrow N(^2P) + e$	BOLSIG ⁺	3.58		[16]
R4	$e + N \rightarrow N^+ + 2e$	BOLSIG ⁺	14.54		[16]
R5	$e + N_2 \rightarrow N_2 + e$	BOLSIG ⁺	0.0	S1, S2	[60]
R6	$e + N_2 \rightarrow N_2(A^3\Sigma_u^+) + e$	BOLSIG ⁺	6.17	S1, S2	[60]
R7	$e + N_2 \rightarrow N_2(B^3\Pi_g) + e$	BOLSIG ⁺	7.35	S1, S2	[60]
R8	$e + N_2 \rightarrow N_2(a^1\Sigma_u^-) + e$	BOLSIG ⁺	8.40	S1, S2	[60]
R9	$e + N_2 \rightarrow N_2(C^3\Pi_u) + e$	BOLSIG ⁺	11.03	S1, S2	[60]
R10	$e + N_2 \rightarrow N + N + e$	BOLSIG ⁺	13.0	S1, S2	[16]
R11	$e + N_2 \rightarrow N_2^+ + 2e$	BOLSIG ⁺	15.58	S1, S2	[60]
R12	$e + O_2 \rightarrow O_2 + e$	BOLSIG ⁺	0.0	S1, S2	[60]
R13	$e + O_2 \rightarrow O^- + O$	BOLSIG ⁺	0.0		[60]
R14	$e + O_2 + O_2 \rightarrow O_2^- + O_2$	BOLSIG ⁺	0.0	S1, S2	[60]
R15	$e + O_2 \rightarrow O_2(a) + e$	BOLSIG ⁺	0.977		[60]
R16	$e + O_2 \rightarrow 2O + e$	BOLSIG ⁺	6.0		[60]
R17	$e + O_2 \rightarrow O + O(^1D) + e$	BOLSIG ⁺	8.4	S2	[60]
R18	$e + O_2 \rightarrow O + O(^1S) + e$	BOLSIG ⁺	10.0		[60]
R19	$e + O_2 \rightarrow O_2^+ + 2e$	BOLSIG ⁺	12.06		[60]
R20	$e + O_3 \rightarrow e + O + O_2$	5.88×10^{-15}	0.0		[66]
R21	$e + NH_3 \rightarrow NH_3 + e$	BOLSIG ⁺	0.0	S1, S2	[16]
R22	$e + NH_3 \rightarrow NH_2 + H^-$	BOLSIG ⁺	0.0	S1, S2	[65]
R23	$e + NH_3 \rightarrow NH_2 + H + e$	BOLSIG ⁺	5.72	S1, S2	[16]
R24	$e + NH_3 \rightarrow NH + H + H + 2e$	BOLSIG ⁺	8.65		[16]
R25	$e + NH_3 \rightarrow NH_3^+ + 2e$	BOLSIG ⁺	10.2	S1, S2	[16]
R26	$e + NH_3 \rightarrow NH_2^+ + H + 2e$	BOLSIG ⁺	16.0	S1, S2	[16]
R27	$e + NH_2 \rightarrow NH_2 + e$	BOLSIG ⁺	0.0		[16]
R28	$e + NH_2 \rightarrow NH + H + e$	BOLSIG ⁺	5.72		[16]
R29	$e + NH_2 \rightarrow N + H + H + 2e$	BOLSIG ⁺	8.65		[16]
R30	$e + NH_2 \rightarrow NH_2^+ + 2e$	BOLSIG ⁺	11.14		[16]
R31	$e + NH_2 \rightarrow NH^+ + H + 2e$	BOLSIG ⁺	17.6		[16]
R32	$e + NH \rightarrow NH + e$	BOLSIG ⁺	0.0		[16]
R33	$e + NH \rightarrow N + H + e$	BOLSIG ⁺	5.72		[16]
R34	$e + NH \rightarrow NH^+ + 2e$	BOLSIG ⁺	13.49		[16]

R35	$e + H_2 \rightarrow H_2 + e$	BOLSIG ⁺	0.0		[16]
R36	$e + H_2 \rightarrow H + H + e$	BOLSIG ⁺	8.9		[16]
R37	$e + H_2 \rightarrow H_2^+ + 2e$	BOLSIG ⁺	15.43		[16]
R38	$e + N_2^+ \rightarrow N(^2D) + N$	3.7×10^{-13}	0.0		[60]
R39	$e + N_2^+ \rightarrow 2N$	$2.8 \times 10^{-13} (T_g / T_e)^{0.5}$	0.0		[7]
R40	$e + N_4^+ \rightarrow N_2(C^3\Pi_u) + N_2$	$2.0 \times 10^{-12} (T_g / T_e)^{0.5}$	0.0		[7]
R41	$e + O_2^+ \rightarrow O(^1D) + O$	2.1×10^{-13}	0.0		[60]
R42	$e + NH_4^+ \rightarrow NH_3 + H$	$9.0 \times 10^{-13} T_e^{-0.6}$	0.0		[4]
R43	$N^+ + H_2 \rightarrow H_2^+ + N$	2.0×10^{-16}	0.0		[67]
R44	$N^+ + NH_3 \rightarrow NH_3^+ + N$	1.7×10^{-15}	0.0		[67]
R45	$N_2^+ + N \rightarrow N^+ + N_2$	5.0×10^{-18}	0.0		[16]
R46	$N_2^+ + N_2 + N_2 \rightarrow N_4^+ + N_2$	1.0×10^{-44}	0.0	S1, S2	[68]
R47	$N_2^+ + NH_3 \rightarrow NH_3^+ + N_2$	1.95×10^{-15}	0.0	S1, S2	[67]
R48	$N_2^+ + H \rightarrow H^+ + N_2$	2.5×10^{-16}	0.0		[67]
R49	$N_2^+ + H_2 \rightarrow H_2^+ + N_2$	4.0×10^{-16}	0.0		[67]
R50	$N_4^+ + N \rightarrow N^+ + 2N_2$	1.0×10^{-17}	0.0		[68]
R51	$N_4^+ + N_2 \rightarrow N_2^+ + 2N_2$	$2.1 \times 10^{-22} \exp(T_g / 120)$	0.0	S1, S2	[69]
R52	$N_4^+ + NH_3 \rightarrow NH_3^+ + 2N_2$	3.0×10^{-17}	0.0	S1, S2	[70]
R53	$N_4^+ + H_2 \rightarrow H_2^+ + 2N_2$	$3 \times 10^{-16} \exp(-1800 / T_g)$	0.0		[68]
R54	$O_2^+ + NH_3 \rightarrow NH_3^+ + O_2$	1.0×10^{-15}	0.0		[71]
R55	$NH^+ + NH_3 \rightarrow NH_4^+ + N$	1.8×10^{-15}	0.0		[16]
R56	$NH^+ + H_2 \rightarrow NH_2^+ + H$	1.0×10^{-15}	0.0		[16]
R57	$NH_2^+ + NH_3 \rightarrow NH_3^+ + NH_2$	2.2×10^{-15}	0.0	S1, S2	[16]
R58	$NH_2^+ + NH_3 \rightarrow NH_4^+ + NH$	2.2×10^{-15}	0.0	S1, S2	[16]
R59	$NH_2^+ + H_2 \rightarrow NH_3^+ + H$	1.0×10^{-15}	0.0	S1, S2	[16]
R60	$NH_3^+ + NH_3 \rightarrow NH_2^+ + H_2 + NH_2$	$6.12 \times 10^{-13} (T_g / 298)^{-0.44} \exp(-3.8 / T_g)$	0.0	S1, S2	[16]
R61	$NH_3^+ + NH_3 \rightarrow NH_4^+ + NH_2$	2.2×10^{-15}	0.0		[16]
R62	$NH_3^+ + NH_3 \rightarrow H^+ + NH_2 + NH_3$	$6.87 \times 10^{-16} (T_g / 298)^{-0.17} \exp(-4.6 / T_g)$	0.0		[16]
R63	$NH_3^+ + H_2 \rightarrow NH_4^+ + H$	4.0×10^{-19}	0.0		[16]
R64	$NH_3^+ + H_2 \rightarrow H^+ + NH_3 + H$	$8.46 \times 10^{-16} (T_g / 298)^{-0.39} \exp(-14.8 / T_g)$	0.0		[16]

R65	$NH_3^+ + H_2 \rightarrow H_2^+ + NH_3$	9.63×10^{-19} $(T_g / 298)^{-0.25} \exp(-14.6 / T_g)$	0.0		[16]
R66	$NH_3^+ + H_2 \rightarrow H_2^+ + NH_2 + H$	2.18×10^{-15} $(T_g / 298)^{-0.2} \exp(-9.9 / T_g)$	0.0		[16]
R67	$H^+ + NH_3 \rightarrow NH_3^+ + H$	5.0×10^{-17}	0.0		[16]
R68	$H^+ + NH_2 \rightarrow NH_2^+ + H$	5.0×10^{-17}	0.0		[16]
R69	$H^+ + NH \rightarrow NH^+ + H$	5.0×10^{-17}	0.0		[16]
R70	$H^+ + H_2 \rightarrow H_2^+ + H$	$3.22 \times 10^{-16} \exp(21856 / T_g)$	0.0		[16]
R71	$H_2^+ + NH_3 \rightarrow NH_3^+ + H_2$	5.7×10^{-15}	0.0		[16]
R72	$H_2^+ + NH_3 \rightarrow NH_4^+ + H$	5.0×10^{-17}	0.0		[16]
R73	$H_2^+ + NH_2 \rightarrow NH_2^+ + H_2$	5.0×10^{-16}	0.0		[16]
R74	$H_2^+ + NH_2 \rightarrow NH_3^+ + H$	5.0×10^{-17}	0.0		[16]
R75	$H_2^+ + NH \rightarrow NH^+ + H_2$	5.0×10^{-16}	0.0		[16]
R76	$H_2^+ + NH \rightarrow NH_2^+ + H$	5.0×10^{-17}	0.0		[16]
R77	$H_2^+ + H \rightarrow H^+ + H_2$	6.40×10^{-16}	0.0		[16]
R78	$H_2^+ + H_2 \rightarrow H_3^+ + H$	2.1×10^{-15}	0.0		[68]
R79	$H_3^+ + NH_3 \rightarrow NH_4^+ + H_2$	4.4×10^{-15}	0.0		[16]
R80	$O_2^- + N \rightarrow NO_2 + e$	5.0×10^{-16}	0.0		[72]
R81	$O_2^- + N_2(A^3\Sigma_u^+) \rightarrow O_2 + N_2 + e$	2.1×10^{-15}	0.0	S1, S2	[60]
R82	$O_2^- + N_2(B^3\Pi_g) \rightarrow O_2 + N_2 + e$	2.5×10^{-15}	0.0		[73]
R83	$O_2^- + O \rightarrow O_3 + e$	1.5×10^{-16}	0.0		[60]
R84	$O_2^- + O_2(a) \rightarrow 2O_2 + e$	2.0×10^{-16}	0.0		[60]
R85	$O_2^- + H_2 \rightarrow H_2O_2 + e$	1.0×10^{-15}	0.0		[67]
R86	$O^- + N \rightarrow NO + e$	2.6×10^{-16}	0.0		[60]
R87	$O^- + N_2(A^3\Sigma_u^+) \rightarrow O + N_2 + e$	2.2×10^{-15}	0.0		[60]
R88	$O^- + N_2(B^3\Pi_g) \rightarrow O + N_2 + e$	1.9×10^{-15}	0.0		[73]
R89	$O^- + O \rightarrow O_2 + e$	5.0×10^{-16}	0.0		[60]
R90	$O^- + O_2 \rightarrow O_3 + e$	5.0×10^{-21}	0.0		[73]
R91	$O^- + O_2(a) \rightarrow O_3 + e$	3.0×10^{-16}	0.0		[73]
R92	$O^- + NO \rightarrow NO_2 + e$	2.6×10^{-16}	0.0		[72]
R93	$O^- + H_2O \rightarrow H_2O_2 + e$	6.0×10^{-19}	0.0		[66]
R94	$H^- + H \rightarrow H_2 + e$	1.8×10^{-15}	0.0	S1, S2	[4]
R95	$N_2^+ + O^- \rightarrow N_2 + O$	7.8×10^{-12}	0.0		[60]
R96	$N_4^+ + O_2^- \rightarrow N_2 + N_2 + O_2$	$2.0 \times 10^{-12} (T_g / 300)^{-0.5}$	0.0	S1, S2	[71]
R97	$O_2^+ + O^- \rightarrow O_2 + O$	7.5×10^{-12}	0.0		[60]

R98	$O_2^+ + O_2^- \rightarrow 2O_2$	7.8×10^{-12}	0.0	[60]
R99	$NH_3^+ + O^- \rightarrow NH_3 + O$	$3.0 \times 10^{-12} (T_g / 300)^{-0.5}$	0.0	[71]
R100	$NH_3^+ + O_2^- \rightarrow NH_3 + O_2$	$2.0 \times 10^{-12} (T_g / 300)^{-0.5}$	0.0	[71]
R101	$NH_4^+ + O^- \rightarrow NH_3 + OH$	$3.0 \times 10^{-12} (T_g / 300)^{-0.5}$	0.0	[71]
R102	$NH_4^+ + O_2^- \rightarrow NH_3 + H + O_2$	$2.0 \times 10^{-12} (T_g / 300)^{-0.5}$	0.0	S1, S2 [71]
R103	$H^- + N_2^+ \rightarrow H + N_2$	$3.0 \times 10^{-12} (T_g / 300)^{-0.5}$	0.0	[71]
R104	$H^- + N_4^+ \rightarrow H + 2N_2$	1.5×10^{-13}	0.0	S1, S2 [69]
R105	$N_2(A^3\Sigma_u^+) + N_2(A^3\Sigma_u^+) \rightarrow N_2 + N_2(B^3\Pi_g)$	7.7×10^{-19}	0.0	[7]
R106	$N_2(A^3\Sigma_u^+) + N_2(A^3\Sigma_u^+) \rightarrow N_2 + N_2(C^3\Pi_u)$	3.0×10^{-16}	0.0	S1, S2 [7]
R107	$N_2(A^3\Sigma_u^+) + O \rightarrow N(^2D) + NO$	7.0×10^{-19}	0.0	[60]
R108	$N_2(A^3\Sigma_u^+) + O \rightarrow O(^1S) + N_2$	2.1×10^{-17}	0.0	S1, S2 [73]
R109	$N_2(A^3\Sigma_u^+) + O_2 \rightarrow 2O + N_2$	1.7×10^{-18}	0.0	S1, S2 [60]
R110	$N_2(A^3\Sigma_u^+) + O_2 \rightarrow O_2(a) + N_2$	7.5×10^{-19}	0.0	S1, S2 [60]
R111	$N_2(A^3\Sigma_u^+) + NO \rightarrow NO(A) + N_2$	6.6×10^{-17}	0.0	S1, S2 [58]
R112	$N_2(A^3\Sigma_u^+) + NH_3 \rightarrow N_2 + NH_2 + H$	3.0×10^{-19}	0.0	S1, S2 [74]
R113	$N_2(A^3\Sigma_u^+) + NH_3 \rightarrow N_2 + NH + H_2$	1.0×10^{-19}	0.0	S1, S2 [67]
R114	$N_2(A^3\Sigma_u^+) + NH_2 \rightarrow N_2 + NH + H$	1.6×10^{-17}	0.0	S1, S2 [67]
R115	$N_2(A^3\Sigma_u^+) + H_2 \rightarrow N_2 + 2H$	$2.0 \times 10^{-16} \exp(-3500/T_g)$	0.0	[68]
R116	$N_2(B^3\Pi_g) + N_2 \rightarrow N_2(A^3\Sigma_u^+) + N_2$	3.0×10^{-17}	0.0	S1, S2 [60]
R117	$N_2(B^3\Pi_g) + O_2 \rightarrow 2O + N_2$	1.1×10^{-16}	0.0	[60]
R118	$N_2(B^3\Pi_g) + H_2 \rightarrow N_2(A^3\Sigma_u^+) + H_2$	2.5×10^{-17}	0.0	[68]
R119	$N_2(a^1\Sigma_u^-) + N_2(A^3\Sigma_u^+) \rightarrow N_4^+ + e$	5.0×10^{-17}	0.0	S1, S2 [73]
R120	$N_2(a^1\Sigma_u^-) + N_2(a^1\Sigma_u^-) \rightarrow N_4^+ + e$	2.0×10^{-16}	0.0	S1, S2 [73]
R121	$N_2(a^1\Sigma_u^-) + N_2 \rightarrow N_2(B^3\Pi_g) + N_2$	2.0×10^{-19}	0.0	S1, S2 [7]
R122	$N_2(a^1\Sigma_u^-) + N_2 \rightarrow 2N_2$	2.0×10^{-19}	0.0	S1, S2 [7]
R123	$N_2(a^1\Sigma_u^-) + O_2 \rightarrow 2O + N_2$	2.8×10^{-17}	0.0	S1, S2 [60]
R124	$N_2(a^1\Sigma_u^-) + NO \rightarrow O + N + N_2$	3.6×10^{-16}	0.0	[60]
R125	$N_2(a^1\Sigma_u^-) + H \rightarrow N_2 + H$	1.5×10^{-16}	0.0	[68]
R126	$N_2(a^1\Sigma_u^-) + H_2 \rightarrow N_2 + 2H$	2.6×10^{-17}	0.0	[68]
R127	$N_2(C^3\Pi_u) + N_2 \rightarrow N_2(a^1\Sigma_u^-) + N_2$	1.0×10^{-17}	0.0	S1, S2 [60]
R128	$N_2(C^3\Pi_u) + O_2 \rightarrow N_2 + O + O(^1S)$	3.0×10^{-16}	0.0	S1, S2 [60]
R129	$N(^2D) + O_2 \rightarrow NO + O$	$1.5 \times 10^{-18} \times (T_g / 300)^{0.5}$	0.0	[73]
R130	$N(^2D) + O_2 \rightarrow NO + O(^1D)$	6.0×10^{-18}	0.0	[60]
R131	$N(^2D) + H_2 \rightarrow NH + H$	2.3×10^{-18}	0.0	[68]
R132	$N(^2D) + NH_3 \rightarrow NH + NH_2$	1.1×10^{-16}	0.0	[68]



R133	$N(^2D) + N_2O \rightarrow N_2 + NO$	3.61×10^{-18}	0.0		[75]
R134	$N(^2P) + NH_3 \rightarrow NH + NH_2$	7.0×10^{-17}	0.0		[67]
R135	$N(^2P) + H_2 \rightarrow H + NH$	2.5×10^{-20}	0.0		[68]
R136	$O(^1S) + N_2 + N_2 \rightarrow O(^1S)N_2 + N_2$	2.0×10^{-48}	0.0	S2	[58]
R137	$O(^1S) + H_2O \rightarrow OH + OH$	3.0×10^{-16}	0.0	S1, S2	[66]
R138	$O(^1D) + O_2 \rightarrow O + O_2(a)$	3.4×10^{-17}	0.0	S2	[60]
R139	$O(^1D) + O_2 \rightarrow O + O_2$	$6.4 \times 10^{-18} \times \text{Exp}(67/T_g)$	0.0		[73]
R140	$O(^1D) + NH_3 \rightarrow NH + H_2O$	2.9×10^{-17}	0.0	S2	[67]
R141	$O(^1D) + NH_3 \rightarrow OH + NH_2$	2.9×10^{-16}	0.0	S2	[67]
R142	$O(^1D) + H_2 \rightarrow OH + H$	1.1×10^{-16}	0.0		[71]
R143	$O(^1D) + H_2O \rightarrow OH + OH$	1.8×10^{-16}	0.0		[75]
R144	$O(^1D) + H_2O_2 \rightarrow H_2O + O_2$	5.2×10^{-16}	0.0		[66]
R145	$O_2(a) + NH_3 \rightarrow NH_3 + O_2$	8.92×10^{-24}	0.0		[75]
R146	$O_2(a) + NH_2 \rightarrow HNO + OH$	1.0×10^{-20}	0.0		[67]
R147	$O_2(a) + NH \rightarrow NO + OH$	1.0×10^{-20}	0.0		[67]
R148	$NO(A^2\Sigma^+) + N_2 \rightarrow NO + N_2$	5.0×10^{-20}	0.0	S1, S2	[58]
R149	$NO(A^2\Sigma^+) + O_2 \rightarrow NO + O_2$	1.5×10^{-16}	0.0		[76]
R150	$NO(A^2\Sigma^+) + NH_3 \rightarrow NO + NH_3$	4.5×10^{-15}	0.0	S1, S2	[41]
R151	$NO(B^2\Pi) + N_2 \rightarrow NO + N_2$	6.1×10^{-22}	0.0	S1, S2	[58]
R152	$NO(B^2\Pi) + O_2 \rightarrow NO + O_2$	1.5×10^{-17}	0.0	S1, S2	[76]
R153	$O(^1S)N_2 + N_2 \rightarrow O(^1S) + N_2 + N_2$	5.0×10^{-18}	0.0	S2	[58]
R154	$O(^1S)N_2 + NH_3 \rightarrow O(^1S) + N_2 + NH_3$	5.0×10^{-18}	0.0		[41]
R155	$N + N + NH_3 \rightarrow N_2 + NH_3$	1.0×10^{-44}	0.0		[16]
R156	$N + O + N_2 \rightarrow NO(B^2\Pi) + N_2$	$(1/35) \times 1.76 \times 10^{-39} \times T_g^{-0.5}$	0.0	S1, S2	[76]
R157	$N + O + NH_3 \rightarrow NO(B^2\Pi) + NH_3$	$(1/35) \times 1.76 \times 10^{-35} \times T_g^{-0.5}$	0.0	S1, S2	[76]
R158	$N + O + N_2 \rightarrow NO + N_2$	$1.76 \times 10^{-42} T_g^{-0.5}$	0.0	S1, S2	[73]
R159	$N + H + NH_3 \rightarrow NH + NH_3$	5.0×10^{-44}	0.0		[16]
R160	$N + H + H \rightarrow NH + H$	5.0×10^{-44}	0.0		[16]
R161	$N + H_2 \rightarrow NH + H$	$2.66 \times 10^{-16} \exp(-12609/T_g)$	0.0		[16]
R162	$N_2 + N_2 \rightarrow N + N + N_2$	$4.29 \times 10^{-16} \exp(-86460/T_g)$	0.0		[16]
R163	$O + O_2 + N_2 \rightarrow O_3 + N_2$	5.6×10^{-46}	0.0		[60]
R164	$O + NH_3 \rightarrow OH + NH_2$	3.59×10^{-21}	0.0	S1, S2	[75]
R165	$O + NH_2 \rightarrow H + HNO$	2.78×10^{-17}	0.0		[75]
R166	$O + NH_2 \rightarrow OH + NH$	1.2×10^{-17}	0.0	S1, S2	[75]
R167	$O + NH \rightarrow NO + H$	1.16×10^{-16}	0.0	S1, S2	[75]
R168	$O + N_2H_2 \rightarrow NH_2 + NO$	1.66×10^{-17}	0.0	S1, S2	[67]
R169	$O + N_2H_3 \rightarrow NH_2 + HNO$	1.66×10^{-17}	0.0	S1, S2	[67]

R170	$O + N_2H_4 \rightarrow N_2H_3 + OH$	5×10^{-18}	0.0		[67]
R171	$O + HNO \rightarrow OH + NO$	1.82×10^{-17}	0.0		[71]
R172	$O_2 + NH_2 \rightarrow HNO + OH$	1.0×10^{-24}	0.0		[67]
R173	$O_3 + H \rightarrow OH + O_2$	4.31×10^{-17}	0.0		[75]
R174	$H + H + N_2 \rightarrow H_2 + N_2$	$1.9 \times 10^{-43} (T_g / 298)^{-0.06}$	0.0	S1, S2	[16]
R175	$H + H + NH_3 \rightarrow H_2 + NH_3$	1.40×10^{-43}	0.0		[16]
R176	$H + H + NH_2 \rightarrow H_2 + NH_2$	1.40×10^{-43}	0.0		[16]
R177	$H + NH_2 + NH_3 \rightarrow NH_3 + NH_3$	6.0×10^{-42}	0.0		[16]
R178	$H + NH_2 + NH_2 \rightarrow NH_3 + NH_2$	6.0×10^{-42}	0.0		[16]
R179	$H + NH_2 + H \rightarrow H + NH_3$	6.0×10^{-42}	0.0		[16]
R180	$H + H_2O_2 \rightarrow H_2O + OH$	$4 \times 10^{-17} \exp(-2000 / T_g)$	0.0		[66]
R181	$NH_3 + H \rightarrow H_2 + NH_2$	$1.34 \times 10^{-16} \exp(-7352 / T_g)$	0.0		[16]
R182	$NH_3 + NH + N_2 \rightarrow N_2H_4 + N_2$	5.0×10^{-47}	0.0		[16]
R183	$NH_2 + N \rightarrow N_2 + H + H$	1.2×10^{-16}	0.0	S1, S2	[16]
R184	$NH_2 + NH_2 \rightarrow H_2 + N_2H_2$	8.31×10^{-17}	0.0	S1, S2	[16]
R185	$NH_2 + NH_2 \rightarrow NH_3 + NH$	$8.31 \times 10^{-17} \exp(-5100 / T_g)$	0.0		[16]
R186	$NH_2 + NH \rightarrow H + N_2H_2$	$2.49 \times 10^{-15} (T_g / 298)^{-0.5}$	0.0	S1, S2	[16]
R187	$NH_2 + NH \rightarrow N_2H_3$	1.16×10^{-16}	0.0	S1, S2	[16]
R188	$NH_2 + H + N_2 \rightarrow NH_3 + N_2$	6.06×10^{-42}	0.0	S1, S2	[16]
R189	$NH_2 + H \rightarrow H_2 + NH$	4.81×10^{-18}	0.0		[16]
R190	$NH_2 + H_2 \rightarrow H + NH_3$	$2.09 \times 10^{-18} \exp(-4277 / T_g)$	0.0		[16]
R191	$NH + N \rightarrow N_2 + H$	2.5×10^{-17}	0.0	S1, S2	[16]
R192	$NH + NH \rightarrow N_2 + H + H$	1.16×10^{-15}	0.0	S1, S2	[16]
R193	$NH + NH \rightarrow NH_2 + N$	$1.4 \times 10^{-20} (T_g / 298)^{2.89} \exp(1015 / T_g)$	0.0		[16]
R194	$NH + NH \rightarrow N_2H_2$	3.49×10^{-18}	0.0		[16]
R195	$NH + H \rightarrow H_2 + N$	$5.98 \times 10^{-17} \exp(-166 / T_g)$	0.0	S1, S2	[16]
R196	$NH + H_2 \rightarrow H + NH_2$	$5.96 \times 10^{-17} \exp(-7782 / T_g)$	0.0		[16]
R197	$N_2H + NH_2 \rightarrow N_2 + NH_3$	8.31×10^{-17}	0.0	S1, S2	[16]
R198	$N_2H + NH \rightarrow N_2 + NH_2$	8.31×10^{-17}	0.0	S1, S2	[16]
R199	$N_2H + H \rightarrow N_2 + H_2$	$6.64 \times 10^{-17} \exp(-1531 / T_g)$	0.0	S1, S2	[16]
R200	$N_2H_2 + NH_2 \rightarrow N_2 + H + NH_3$	$1.53 \times 10^{-19} (T_g / 298)^{4.05} \exp(810.7 / T_g)$	0.0		[16]
R201	$N_2H_2 + NH_2 \rightarrow N_2H + NH_3$	$1.66 \times 10^{-17} \exp(-510 / T_g)$	0.0	S1, S2	[16]

R202	$N_2H_2 + NH \rightarrow N_2H + NH_2$	$1.66 \times 10^{-17} \exp(-510/T_g)$	0.0		[16]
R203	$N_2H_2 + H \rightarrow N_2 + H + H_2$	$4.53 \times 10^{-19} (T_g/298)^{2.63} \exp(115/T_g)$	0.0		[16]
R204	$N_2H_2 + H \rightarrow N_2H + H_2$	$8.31 \times 10^{-17} \exp(-510/T_g)$	0.0	S1, S2	[16]
R205	$N_2H_3 + H \rightarrow NH_2 + NH_2$	2.66×10^{-18}	0.0	S1, S2	[16]
R206	$N_2H_3 + N_2H_3 \rightarrow NH_3 + NH_3 + N_2$	5.0×10^{-18}	0.0		[16]
R207	$N_2H_3 + N_2H_3 \rightarrow N_2H_4 + N_2H_2$	2.0×10^{-17}	0.0	S2	[16]
R208	$N_2H_4 + N \rightarrow NH_2 + N_2H_2$	1.25×10^{-19}	0.0		[16]
R209	$N_2H_4 + NH_2 \rightarrow NH_3 + N_2H_3$	5.15×10^{-19}	0.0		[16]
R210	$N_2H_4 + H \rightarrow N_2H_3 + H_2$	$1.17 \times 10^{-19} \exp(-1260.5/T_g)$	0.0		[16]
R211	$NO + N \rightarrow N_2 + O$	3.4×10^{-17}	0.0	S1, S2	[75]
R212	$NO + O + N_2 \rightarrow NO_2 + N_2$	8.4×10^{-44}	0.0		[72]
R213	$NO + NH_2 \rightarrow N_2 + H_2O$	1.2×10^{-17}	0.0	S1, S2	[75]
R214	$NO + NH_2 \rightarrow N_2 + H + OH$	1.7×10^{-18}	0.0	S1, S2	[77]
R215	$NO + NH \rightarrow H + N_2O$	3.03×10^{-17}	0.0		[75]
R216	$NO + H + N_2 \rightarrow HNO + N_2$	1.57×10^{-44}	0.0		[75]
R217	$NO_2 + N \rightarrow N_2O + O$	3.0×10^{-18}	0.0		[72]
R218	$NO_2 + O \rightarrow NO + O_2$	1.0×10^{-17}	0.0		[72]
R219	$NO_2 + NH_2 \rightarrow H_2O + N_2O$	3.27×10^{-18}	0.0		[75]
R220	$OH + N \rightarrow NO + H$	4.2×10^{-17}	0.0	S1, S2	[77]
R221	$OH + NH_3 \rightarrow H_2O + NH_2$	3.32×10^{-17}	0.0	S1, S2	[77]
R222	$OH + NH_2 \rightarrow H_2O + NH$	3.32×10^{-17}	0.0		[77]
R223	$OH + NH \rightarrow H + HNO$	3.0×10^{-18}	0.0		[77]
R224	$OH + N_2H \rightarrow N_2 + H_2O$	5.0×10^{-17}	0.0		[67]
R225	$OH + OH \rightarrow H_2O_2$	$1.5 \times 10^{-17} (T_g/300)^{-0.37}$	0.0		[66]
R226	$HNO + NH_2 \rightarrow NH_3 + NO$	5.36×10^{-18}	0.0		[71]
R227	$HNO + H \rightarrow H_2 + NO$	3.0×10^{-17}	0.0		[71]
R228	$HNO + OH \rightarrow H_2O + NO$	2.4×10^{-18}	0.0		[77]
R229	$N_2(B^3\Pi_g) \rightarrow N_2(A^3\Sigma_u^+) + hv(1045nm)$	$1.5 \times 10^5 s^{-1}$	0.0		[7]
R230	$N_2(C^3\Pi_u) \rightarrow N_2(B^3\Pi_g) + hv(337.1nm)$	$2.7 \times 10^7 s^{-1}$	0.0	S1, S2	[7]
R231	$N_2(a^1\Sigma_u^-) \rightarrow N_2 + hv(177nm)$	$1.0 \times 10^2 s^{-1}$	0.0		[78]
R232	$N_2(A^3\Sigma_u^+) \rightarrow N_2 + hv(293nm)$	$5.0 \times 10^{-1} s^{-1}$	0.0		[78]
R233	$NO(A^2\Sigma^+) \rightarrow NO + hv(236.3nm)$	$5.0 \times 10^6 s^{-1}$	0.0	S1, S2	[58]
R234	$NO(B^2\Pi) \rightarrow NO + hv(316nm)$	$5.0 \times 10^5 s^{-1}$	0.0	S1, S2	[79]
R235	$O(^1S)N_2 \rightarrow O(^1D) + N_2 + hv(557.7nm)$	$1.0 \times 10^7 s^{-1}$	0.0	S2	[58]

^a Rate coefficients have units of $\text{m}^3 \text{s}^{-1}$ for two-body reactions and $\text{m}^6 \text{s}^{-1}$ for three-body reactions; T_e has units eV; T_g has units K.

^b BOLSIG⁺ can be found in [\[80\]](#).

^c S1: Simplified Chemistry 1; S2: Simplified Chemistry 2.



Table 8. The summary of species with various reduced chemical kinetics.

Species ^a	Chemistry ^b	Species ^a	Chemistry ^b	Species ^a	Chemistry ^b
e	S1, S2	N(² P)		N ₂	S1, S2
O ⁻		N ₂ (A ³ Σ _u ⁺)	S1, S2	NO	S1, S2
O ₂ ⁻	S1, S2	N ₂ (B ³ Π _g)	S1, S2	NO ₂	
H ⁻	S1, S2	N ₂ (a ¹ Σ _u ⁻)	S1, S2	N ₂ O	
O ₂ ⁺		N ₂ (C ³ Π _u)	S1, S2	NH	S1, S2
N ⁺		NO(A)	S1, S2	NH ₂	S1, S2
N ₂ ⁺	S1, S2	NO(B)	S1, S2	NH ₃	S1, S2
N ₄ ⁺	S1, S2	O(¹ S)	S1, S2	N ₂ H	S1, S2
NH ⁺		O(¹ D)	S2	N ₂ H ₂	S1, S2
NH ₂ ⁺		O ₂ (a)	S1, S2	N ₂ H ₃	S1, S2
NH ₃ ⁺	S1, S2	O(¹ S)N ₂	S2	N ₂ H ₄	
NH ₄ ⁺	S1, S2	O	S1, S2	H	S1, S2
H ⁺		O ₂	S1, S2	H ₂	S1, S2
H ₂ ⁺		O ₃	S1, S2	HNO	
H ₃ ⁺		OH	S1, S2	H ₂ O	S1, S2
N(² D)		N	S1, S2	H ₂ O ₂	

^a All species are included in the complete chemistry.

^b S1: Simplified Chemistry 1; S2: Simplified Chemistry 2.

Table 9. Accuracy and computational time with various chemical kinetics.

	Complete Chemistry	Simplified Chemistry 1	Simplified Chemistry 2
Species	48	31	33
Reactions	235	79	87
Hours/Cycle	8.56	3.45	4.04
Max. relative error (%) (Charged+Metastables)	0	4.7%	4.6%
Max. relative error (%) (All selected species)	0	19.9%	4.6%
RMSE (%)	0	4.2%	1.8%



Table 10. The reaction paths for generating the dominant species in N₂/NH₃ discharge.

Species	Generated reactions	Destroyed reactions
Electron	$N_2 + e^- \rightarrow N_2^+ + 2e^-$	$N_4^+ + e^- \rightarrow N_2^* + N_2$
N ₂ ⁺	$N_2 + e^- \rightarrow N_2^+ + 2e^-$	$N_2^+ + N \rightarrow N^+ + N_2$
NH ₄ ⁺	$NH_2^+ + NH_3 \rightarrow NH_4^+ + NH$	$NH_4^+ + e^- \rightarrow NH_3 + H$
N ₂ [*]	$N_2 + e^- \rightarrow N_2^* + e^-$	$N_2^* + N_2 \rightarrow N_2 + N_2$
N	$N_2 + e^- \rightarrow N + N + e^-$	$NH_2 + N \rightarrow N_2 + H + H$
NH ₂	$NH_3 + e^- \rightarrow NH_2 + H + e^-$	$NH_2 + N \rightarrow N_2 + H + H$



Table 11. The reaction paths for generating the dominant species in N₂/O₂/NH₃ discharge.

Species	Generated reactions	Destroyed reactions
Electron	$e + N_2 \rightarrow N_2^+ + 2e$	$e + NH_3 \rightarrow NH_2 + H^-$ $e + O_2 + O_2 \rightarrow O_2^- + O_2$
N ₂ ⁺	$e + N_2 \rightarrow N_2^+ + 2e$	$N_2^+ + N_2 + N_2 \rightarrow N_4^+ + N_2$ $N_2^+ + NH_3 \rightarrow NH_3^+ + N_2$
N ₄ ⁺	$N_2^+ + N_2 + N_2 \rightarrow N_4^+ + N_2$	$N_4^+ + N_2 \rightarrow N_2^+ + 2N_2$ $N_4^+ + NH_3 \rightarrow NH_3^+ + 2N_2$
NH ₄ ⁺	$NH_2^+ + NH_3 \rightarrow NH_4^+ + NH$ $NH_3^+ + NH_3 \rightarrow NH_4^+ + NH_2$	$NH_4^+ + O_2^- \rightarrow NH_3 + H + O_2$
N ₂ (A)	$N_2(B^3\Pi_g) + N_2 \rightarrow N_2(A^3\Sigma_u^+) + N_2$	$N_2(A^3\Sigma_u^+) + N_2(A^3\Sigma_u^+) \rightarrow N_2 + N_2(C^3\Pi_u)$ $N_2(A^3\Sigma_u^+) + NH_3 \rightarrow N_2 + NH_2 + H$ $N_2(A^3\Sigma_u^+) + NH_3 \rightarrow N_2 + NH + H_2$
N ₂ (C)	$e + N_2 \rightarrow N_2(C^3\Pi_u) + e$	$N_2(C^3\Pi_u) + N_2 \rightarrow N_2(a^1\Sigma_u^-) + N_2$
NO(A)	$N_2(A^3\Sigma_u^+) + NO \rightarrow NO(A) + N_2$	$NO(A^2\Sigma^+) + NH_3 \rightarrow NO + NH_3$ $NO(A^2\Sigma^+) \rightarrow NO + hv$
NO(B)	$N + O + N_2 \rightarrow NO(B^2\Pi) + N_2$ $N + O + NH_3 \rightarrow NO(B^2\Pi) + NH_3$	$NO(B^2\Pi) \rightarrow NO + hv$
N	$e + N_2 \rightarrow N + N + e$	$N + O + N_2 \rightarrow NO(B^2\Pi) + N_2$ $N + O + NH_3 \rightarrow NO(B^2\Pi) + NH_3$ $NH_2 + N \rightarrow N_2 + H + H$ $NO + N \rightarrow N_2 + O$
O	$N_2(A^3\Sigma_u^+) + O_2 \rightarrow 2O + N_2$ $NO + N \rightarrow N_2 + O$	$N_2(A^3\Sigma_u^+) + O \rightarrow O(^1S) + N_2$ $N + O + N_2 \rightarrow NO(B^2\Pi) + N_2$ $N + O + NH_3 \rightarrow NO(B^2\Pi) + NH_3$
NH ₂	$NH_3^+ + NH_3 \rightarrow NH_2^+ + H_2 + NH_2$ $N_2(A^3\Sigma_u^+) + NH_3 \rightarrow N_2 + NH_2 + H$	$NH_2 + N \rightarrow N_2 + H + H$ $NH_2 + NH \rightarrow H + N_2H_2$ $NH_2 + H + N_2 \rightarrow NH_3 + N_2$
H ₂	$NH_3^+ + NH_3 \rightarrow NH_2^+ + H_2 + NH_2$ $N_2(A^3\Sigma_u^+) + NH_3 \rightarrow N_2 + NH + H_2$	$O_2^- + H_2 \rightarrow H_2O_2 + e$ $N_2(a^1\Sigma_u^-) + H_2 \rightarrow N_2 + 2H$

Figures

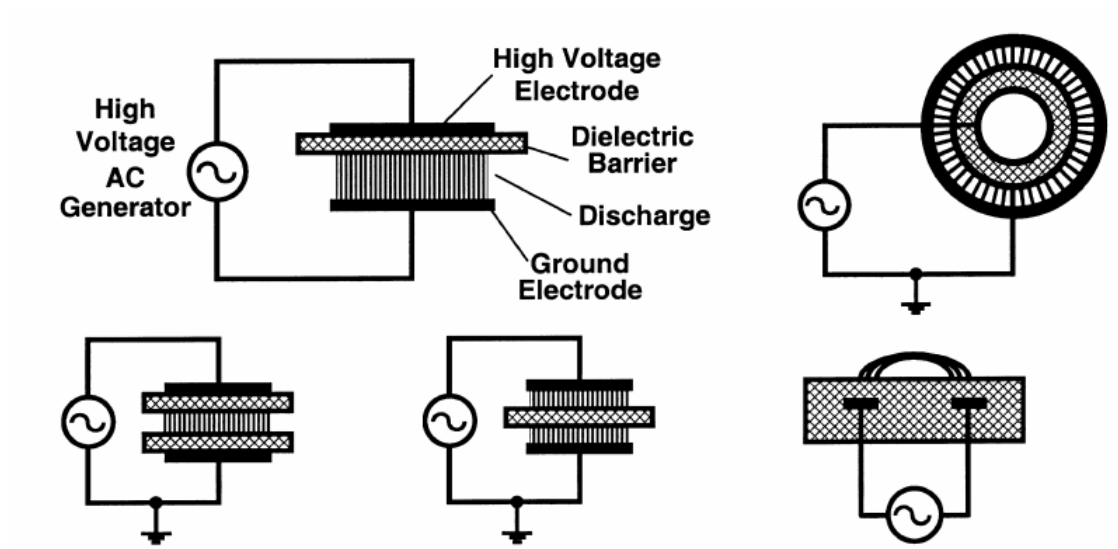
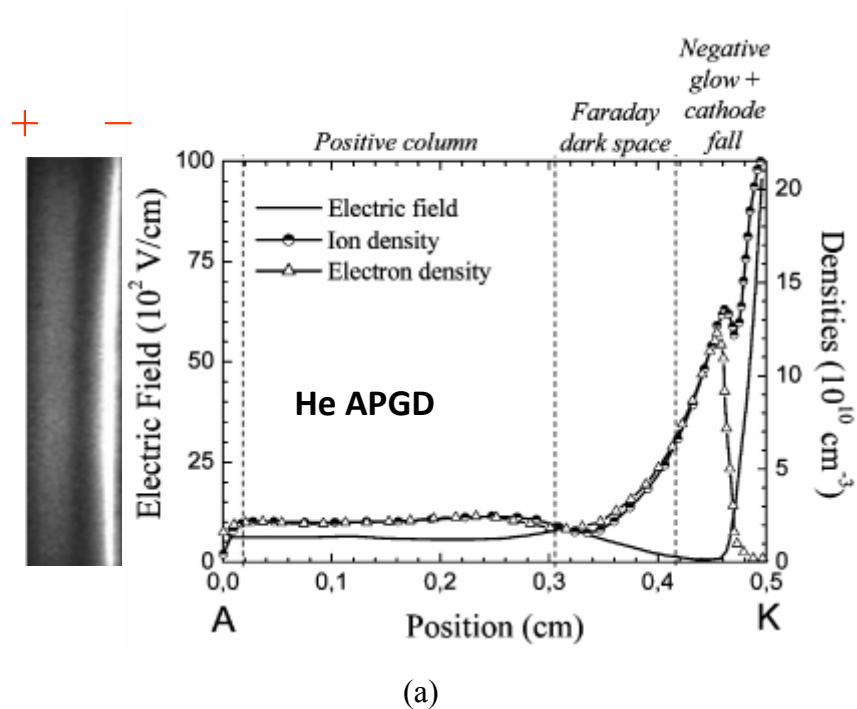
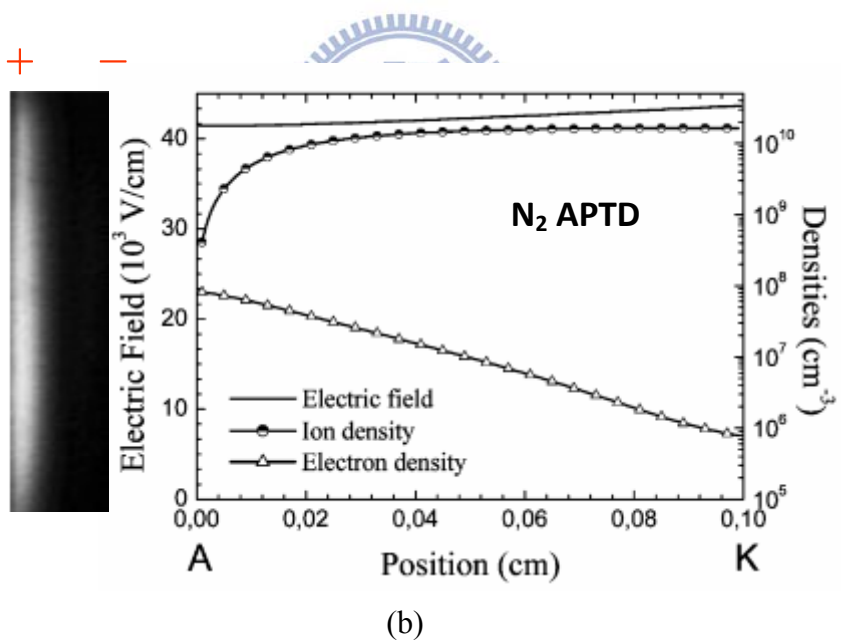


Figure 1. Common planar and cylindrical dielectric barrier discharge configurations

[28].



(a)



(b)

Figure 2. Measured light distribution and calculated space distribution from anode to cathode in (a) a He APGD and (b) a N₂ APTD when the discharge current intensity is maximum [38].

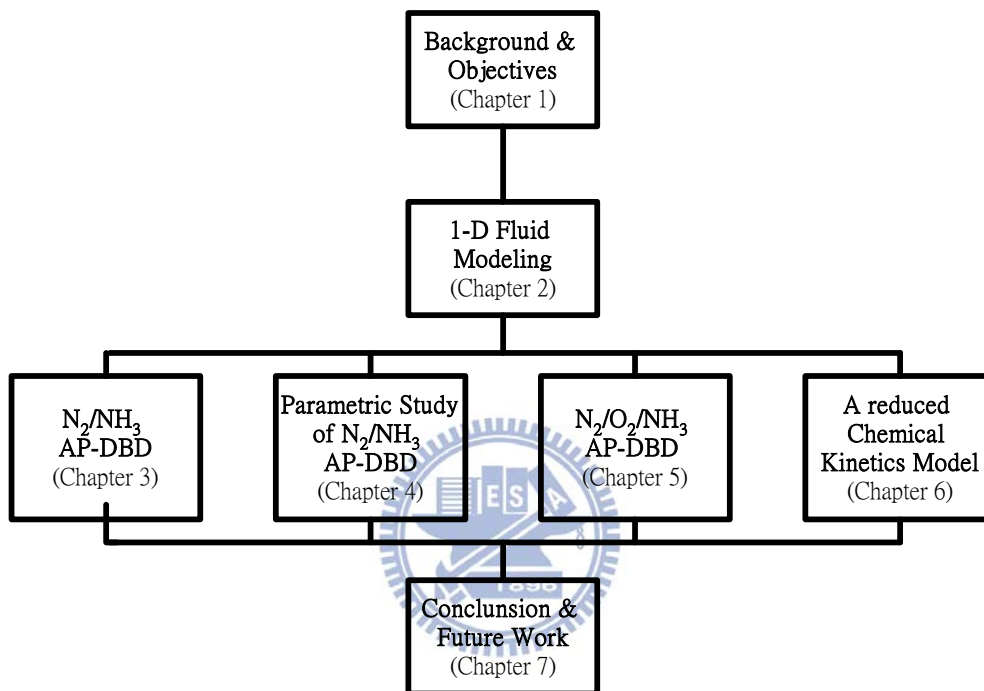


Figure 3. The schematic framework of the thesis.

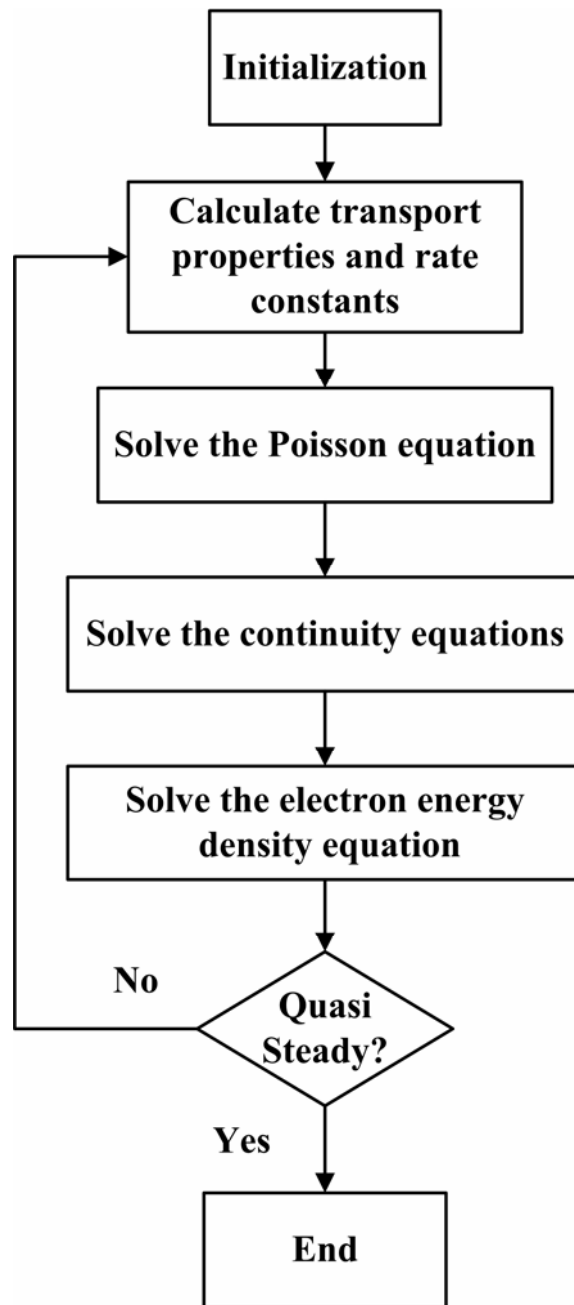


Figure 4. The flowchart of fluid modeling simulation.

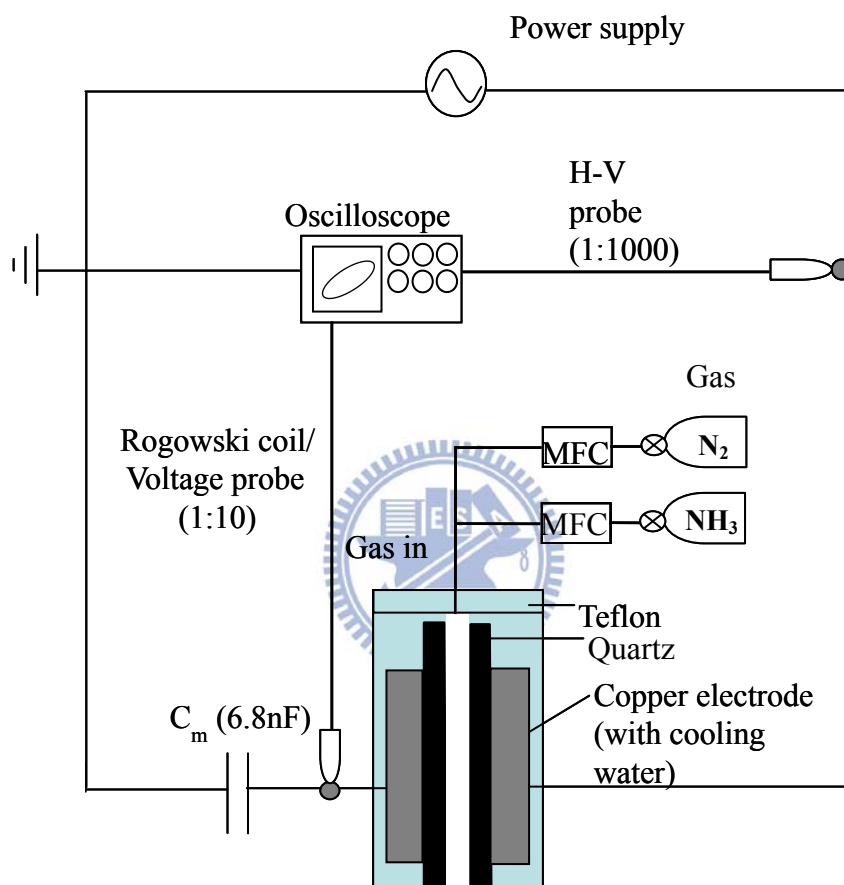


Figure 5. Sketch of a planar N_2/NH_3 atmospheric pressure dielectric barrier discharge system.

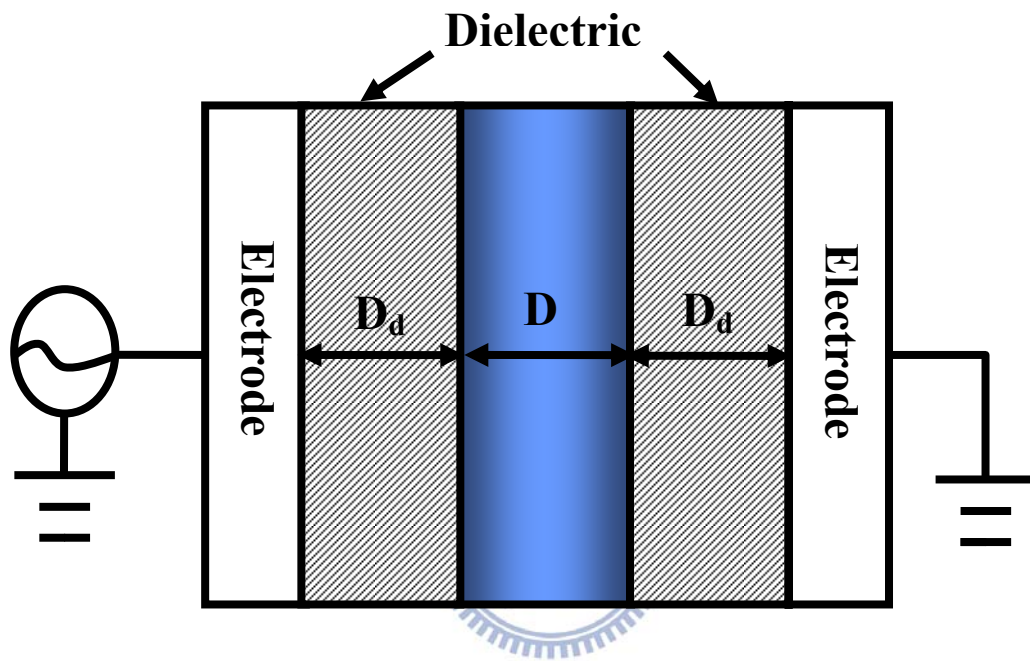


Figure 6. The schematic diagram of one-dimensional atmospheric pressure dielectric barrier discharge simulated in the study.

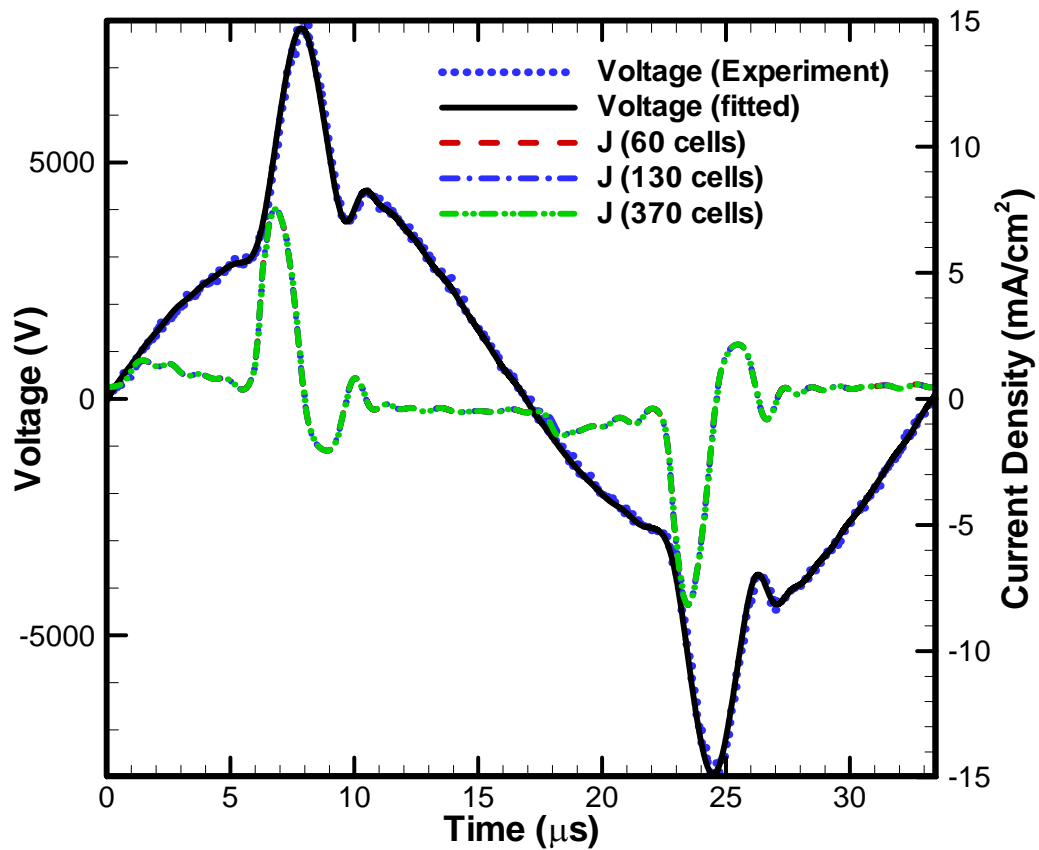


Figure 7. The test grid convergence for $N_2/0.01\% NH_3$ AP-DBD as the applied voltage of 8 kV and the frequency of 30 kHz.

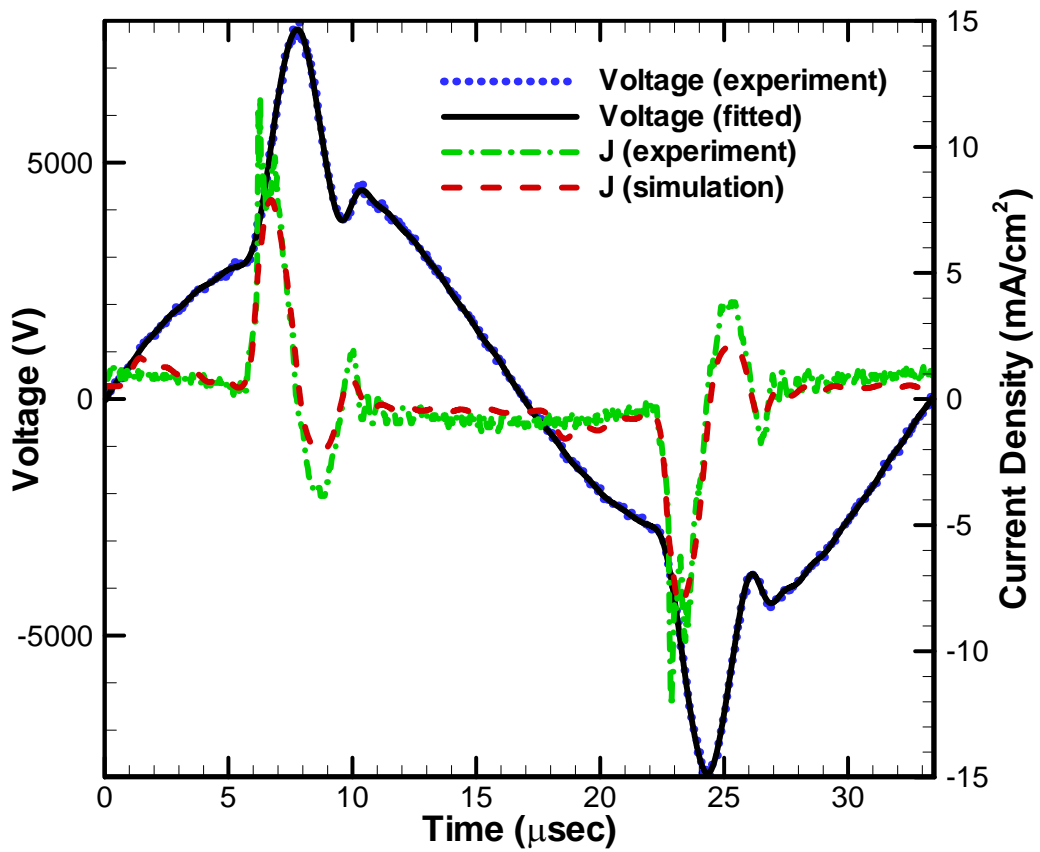
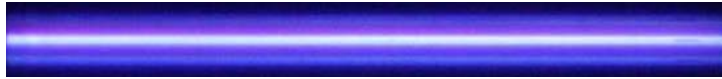


Figure 8. Comparison between the simulated and measured current density in pure nitrogen AP-DBD.

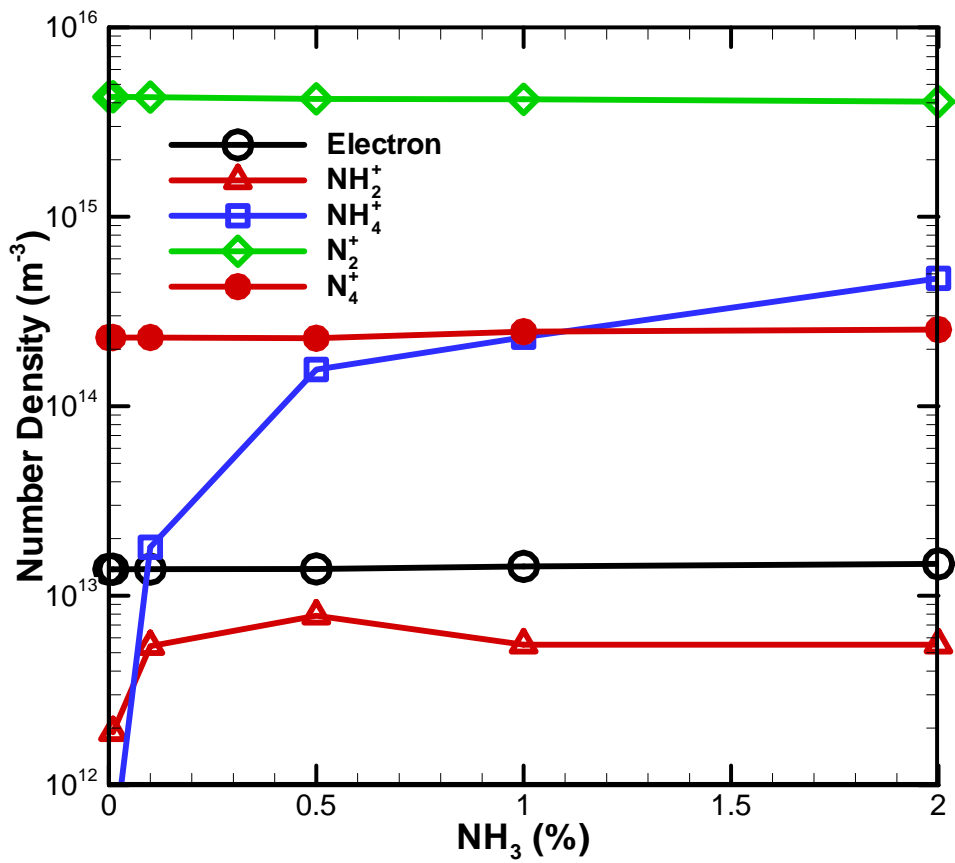


Figure 9. Spatiotemporal averaged number densities of charge species with concentration ratio of ammonia in AP-DBD.

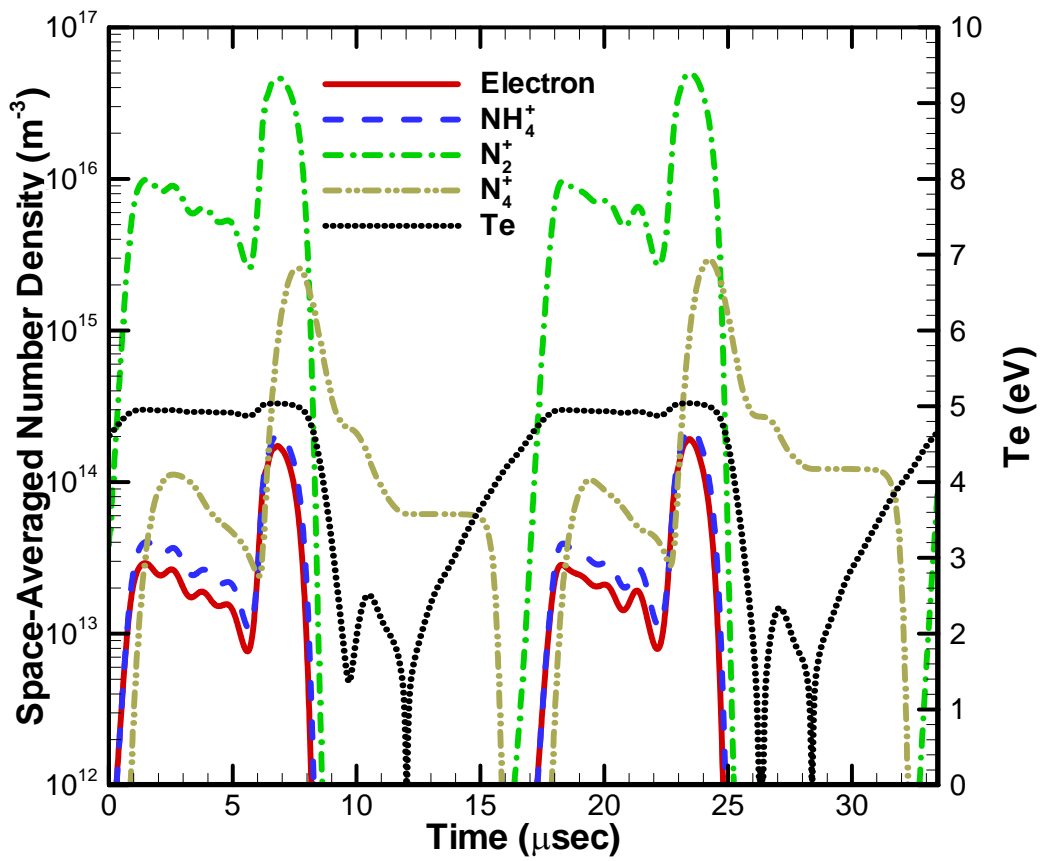


Figure 10. Temporal profiles of the space-averaged number densities of charge species for $N_2/0.1\%NH_3$ AP-DBD.

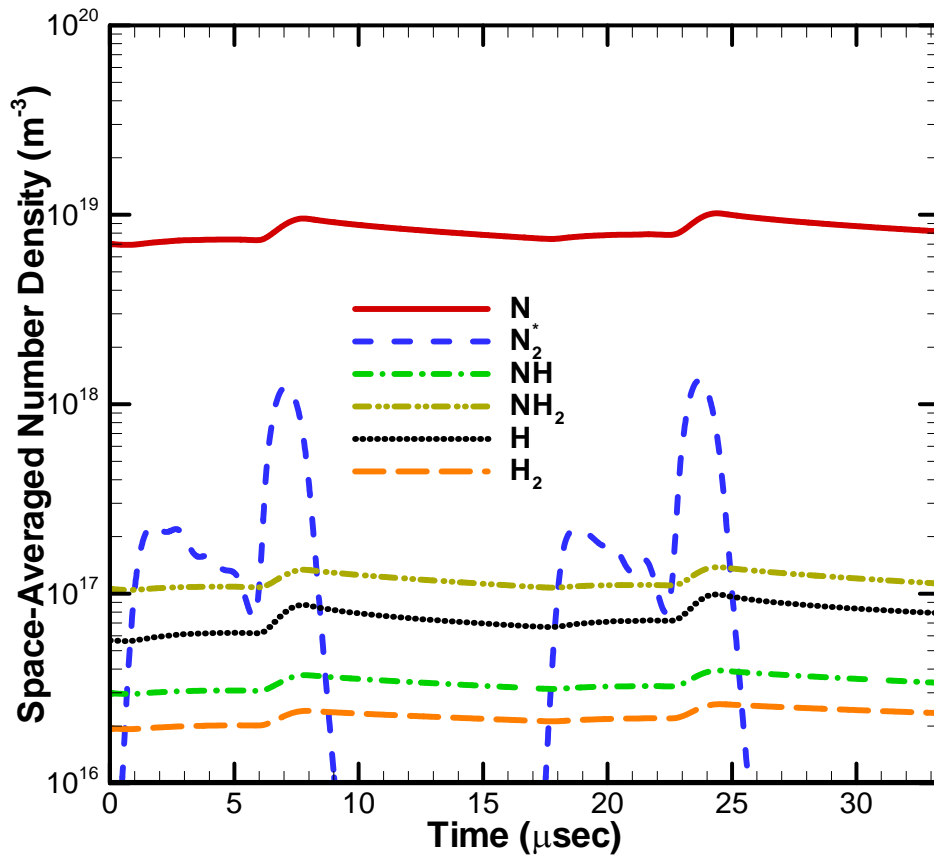


Figure 11. Temporal profiles of the space-averaged number densities of neutral species for $N_2/0.1\%NH_3$ AP-DBD.

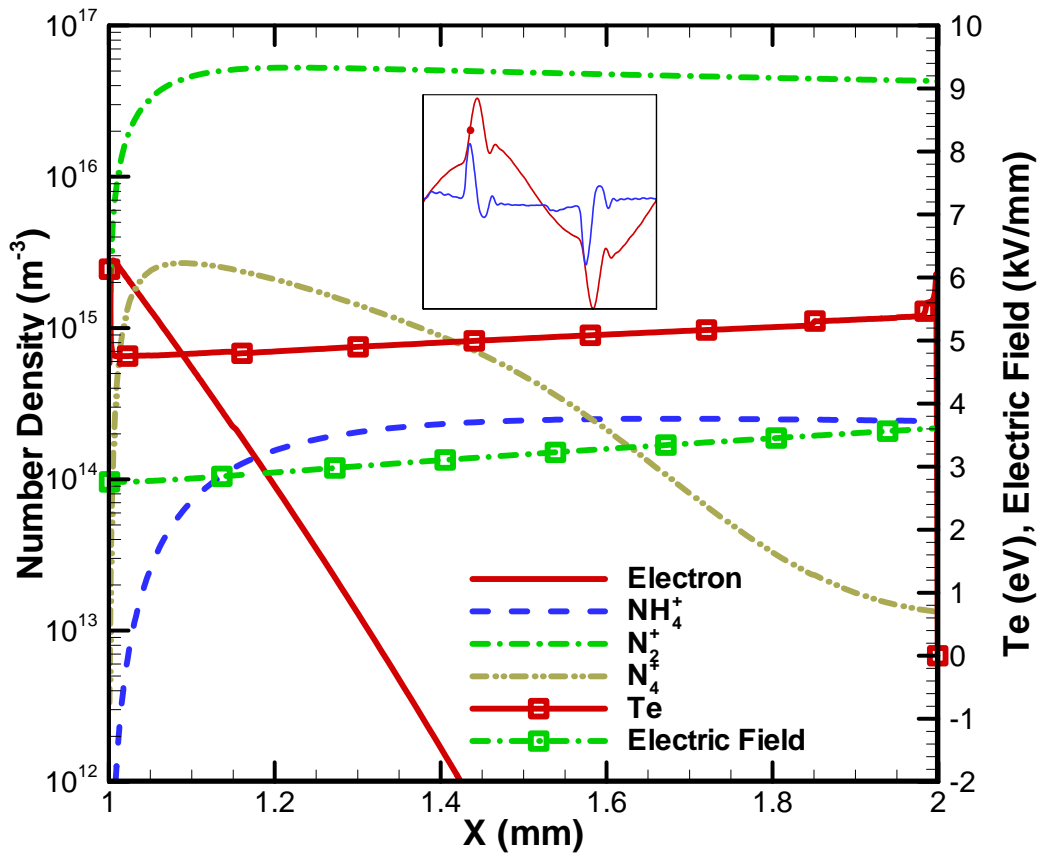


Figure 12. Distributions of charge species densities across the electrode gap for $\text{N}_2/0.1\%\text{NH}_3$ AP-DBD at the peak of discharge current density.

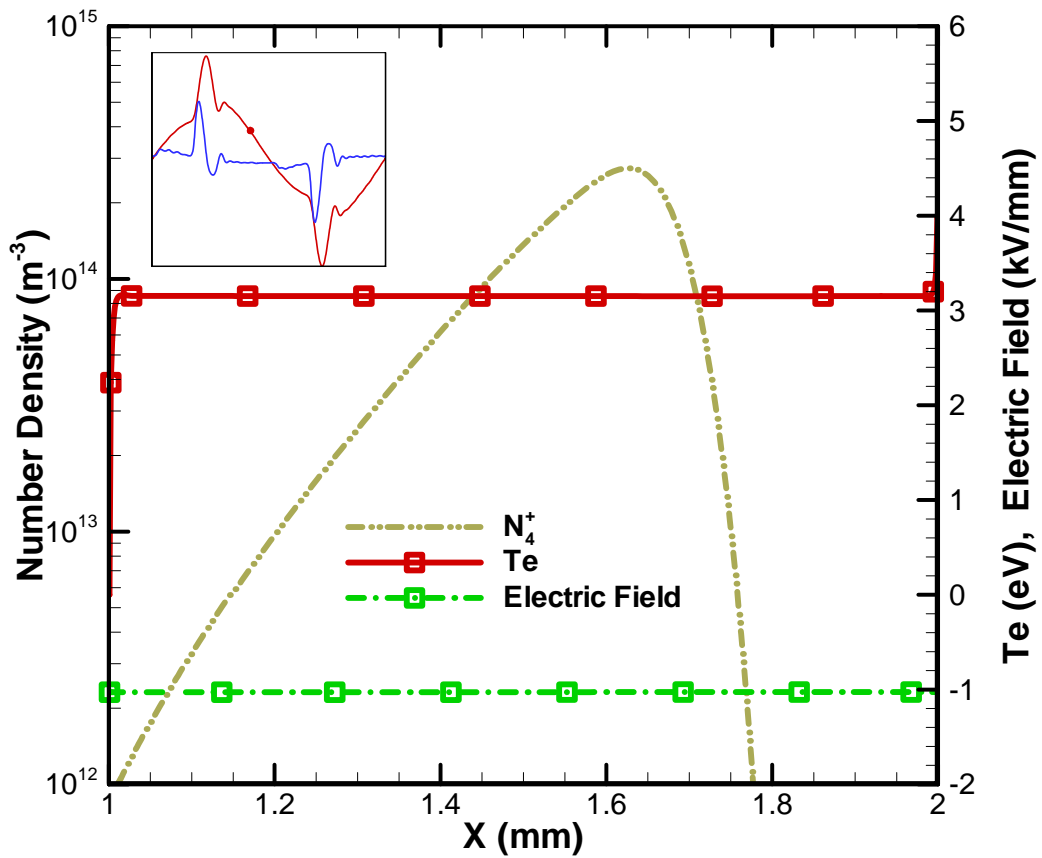


Figure 13. Distributions of charge species densities across the electrode gap for $N_2/0.1\%NH_3$ AP-DBD in the post-breakdown period.

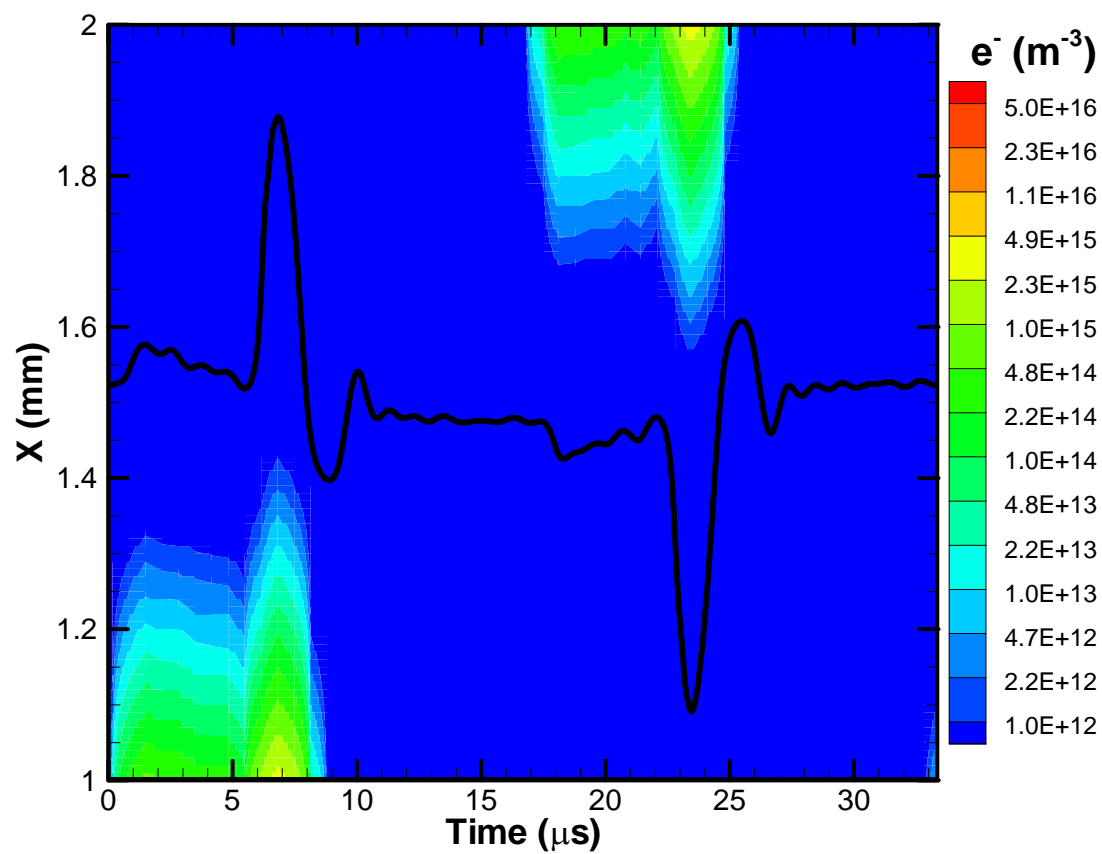


Figure 14. Spatiotemporal distribution of electron number density.

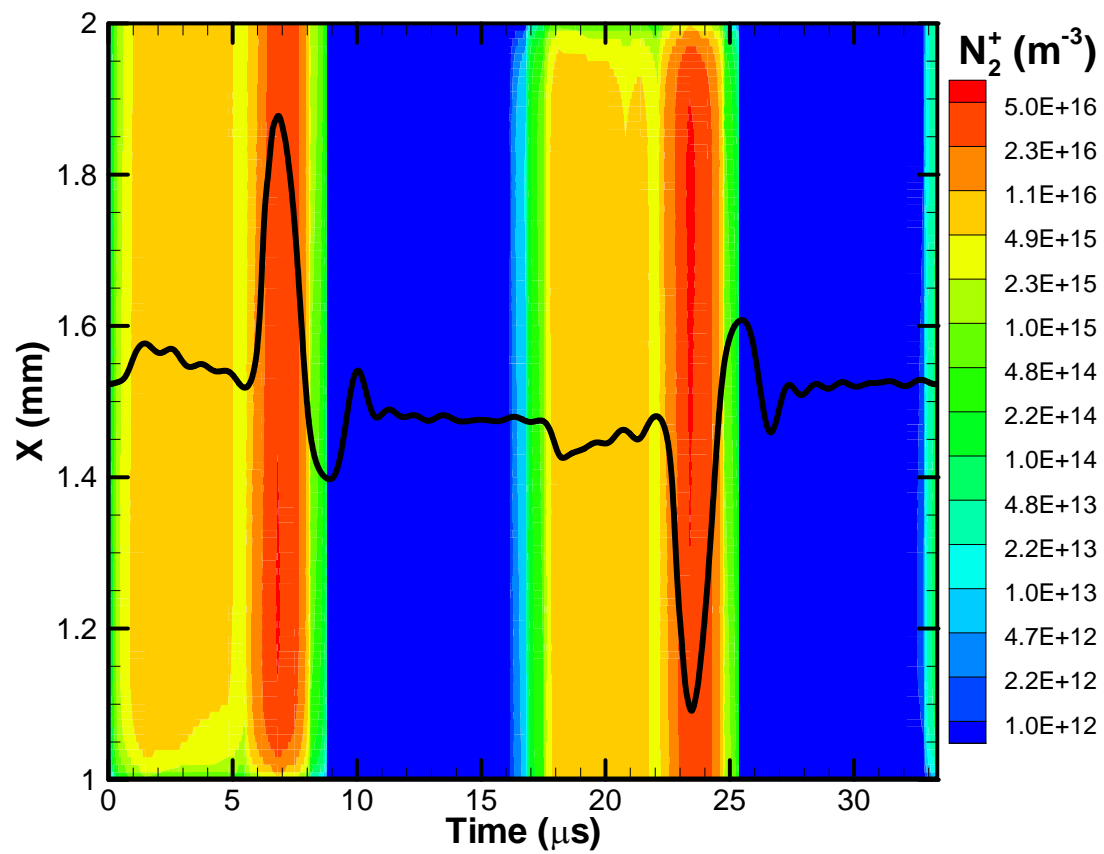


Figure 15. Spatiotemporal distribution of N_2^+ number density.

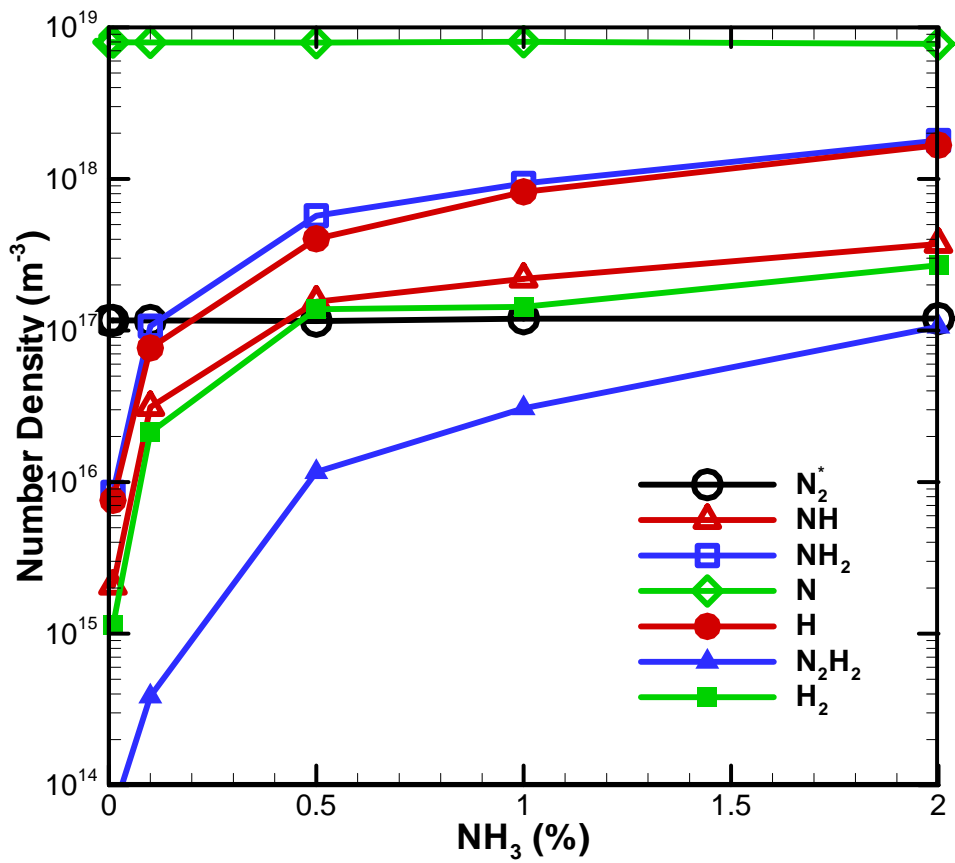
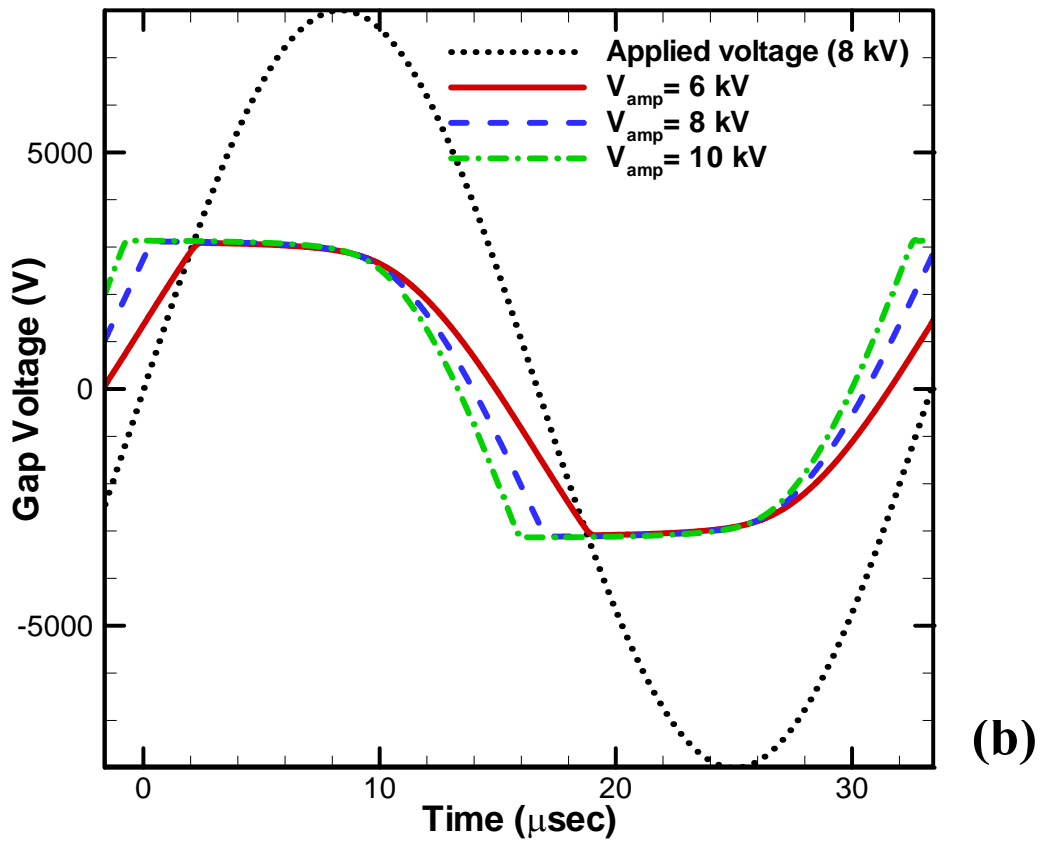
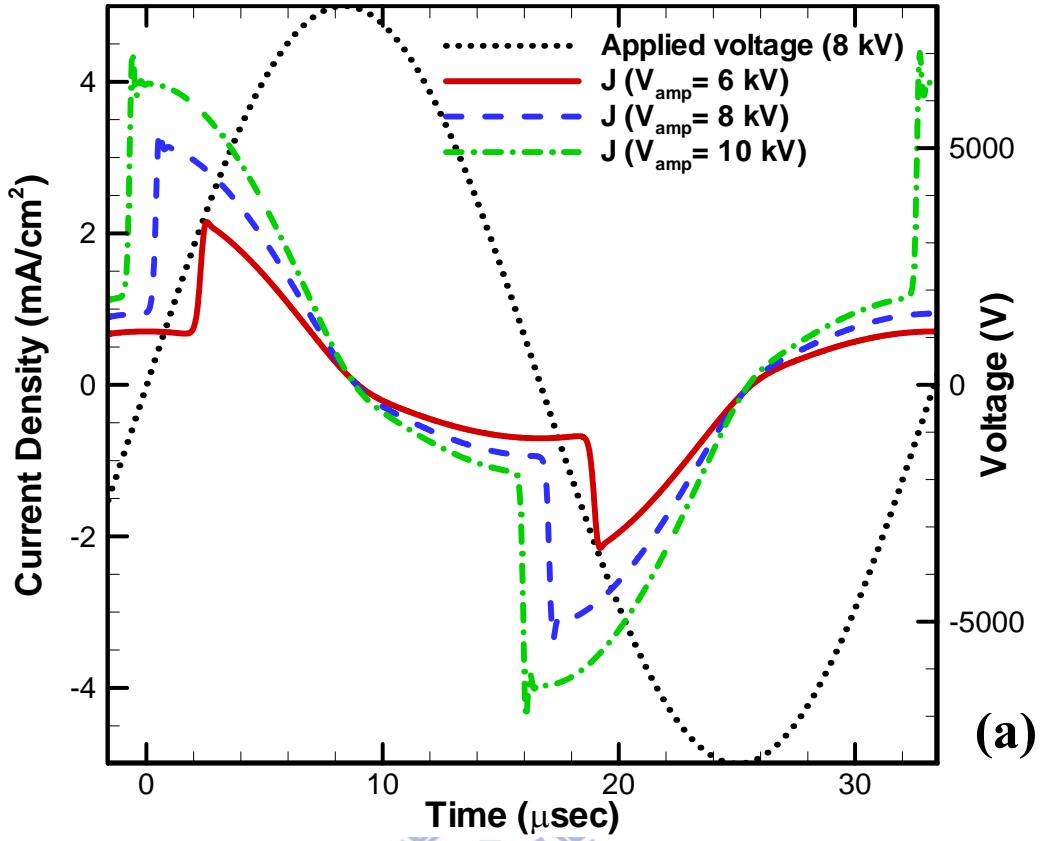


Figure 16. Spatiotemporal averaged number densities of neutral species with concentration ratio of ammonia in AP-DBD.



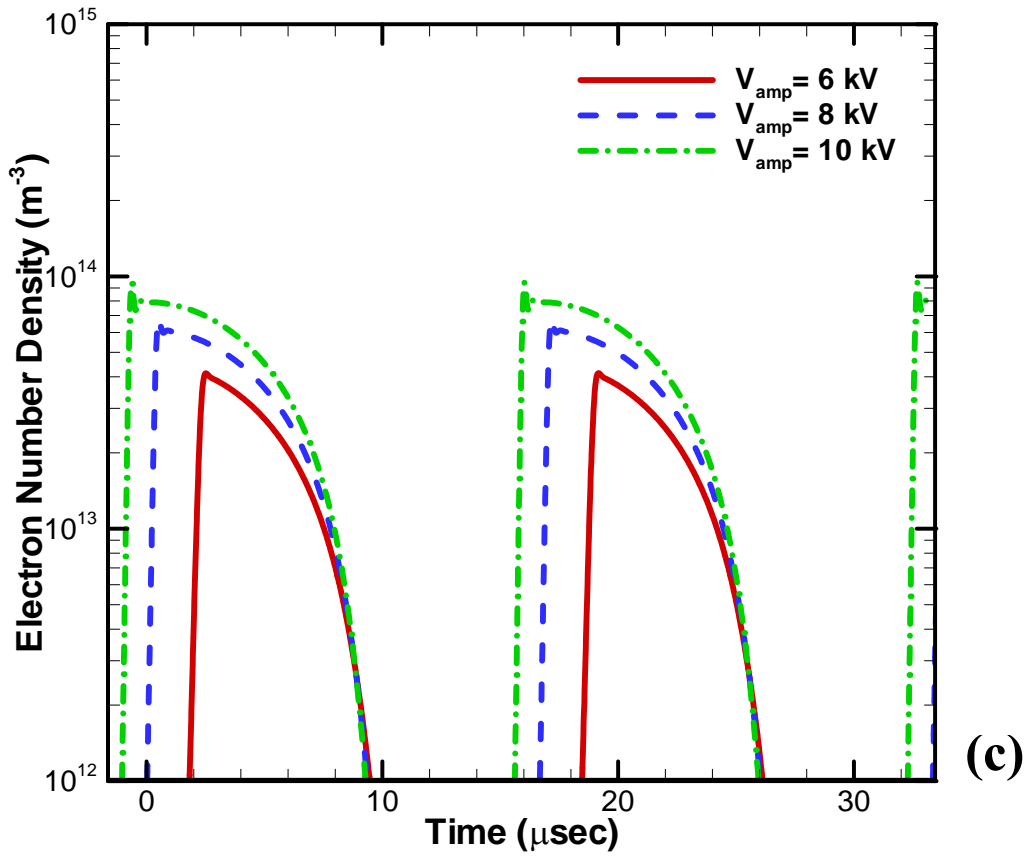
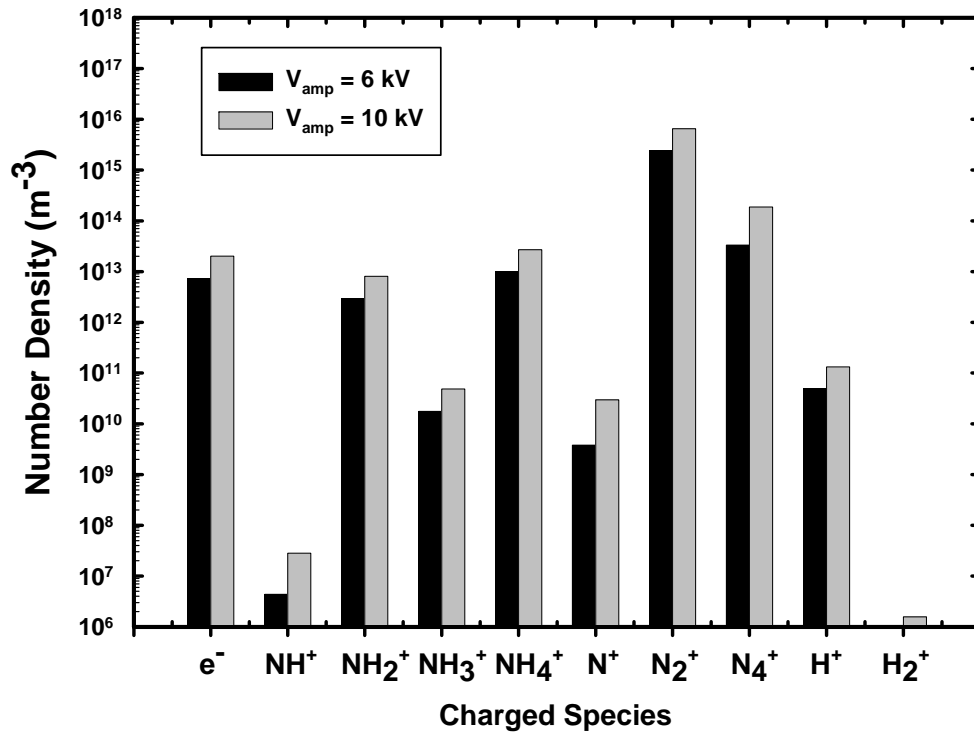
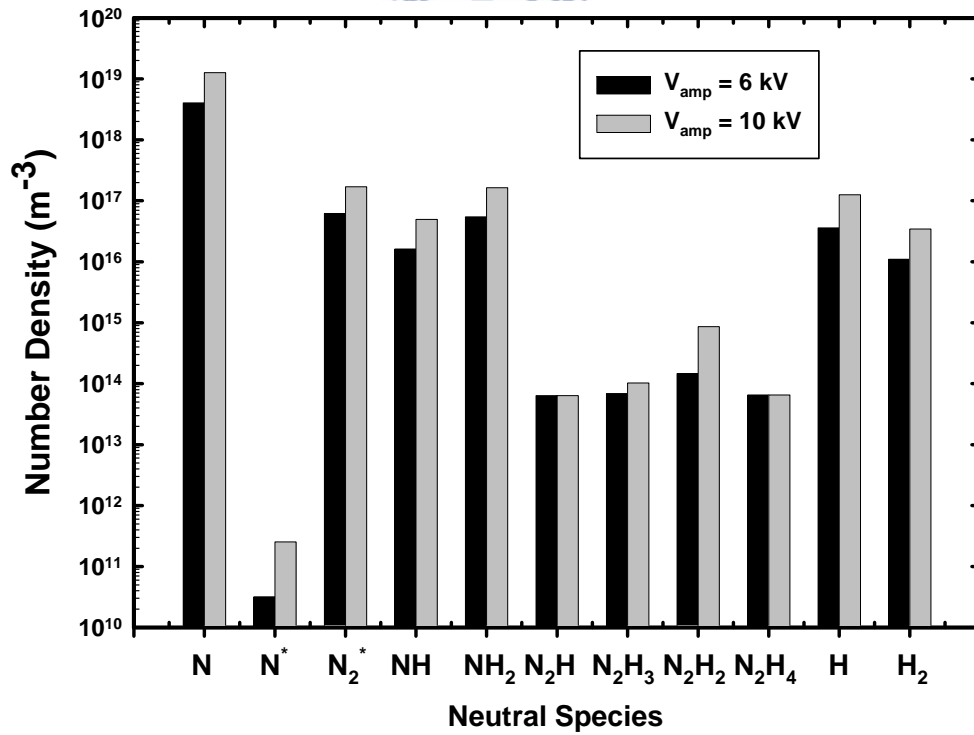


Figure 17. Temporal variation of discharge properties: (a) discharge current density, (b) gap voltage, and (c) electron number density with various amplitude of voltage.

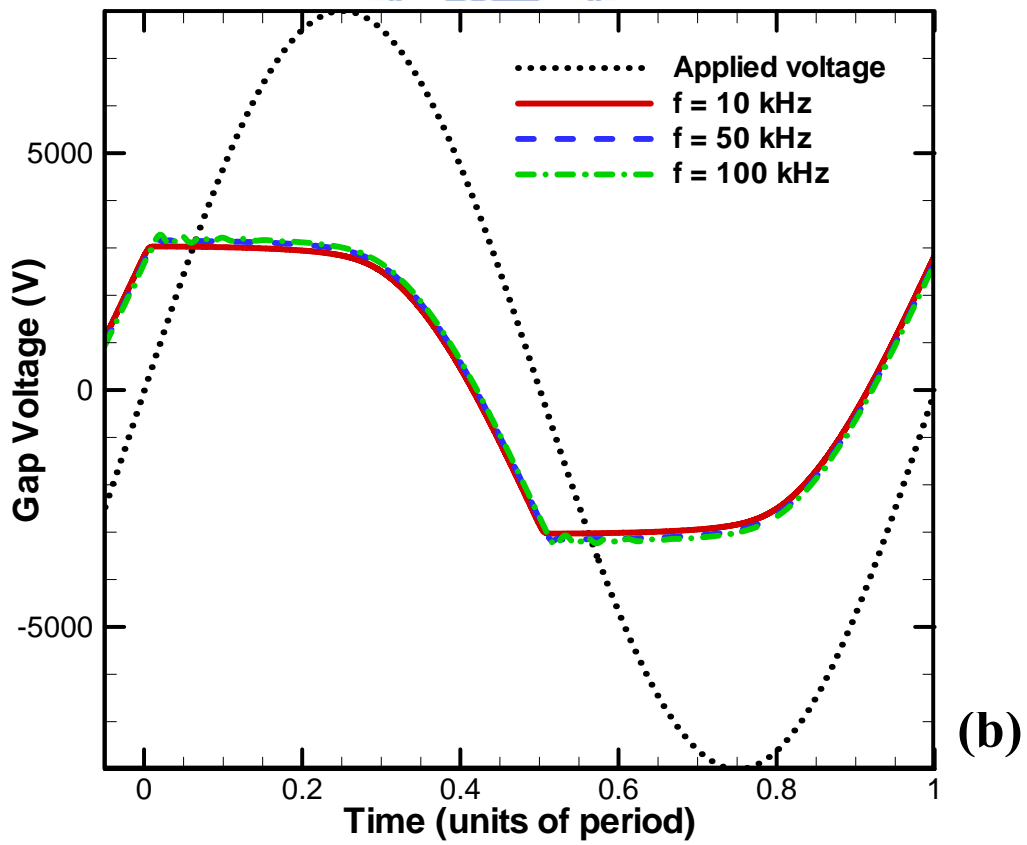
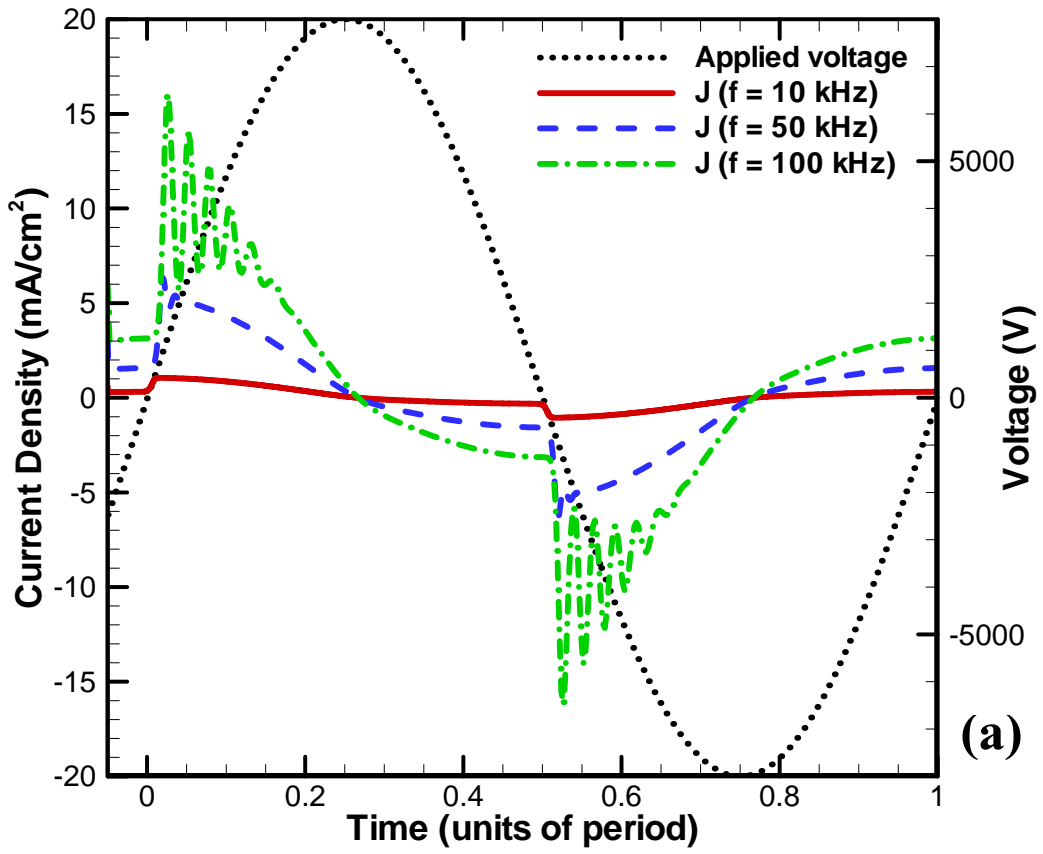


(a)



(b)

Figure 18. Spatiotemporal averaged number densities of (a) charged species and (b) neutrals with various amplitude of voltage.



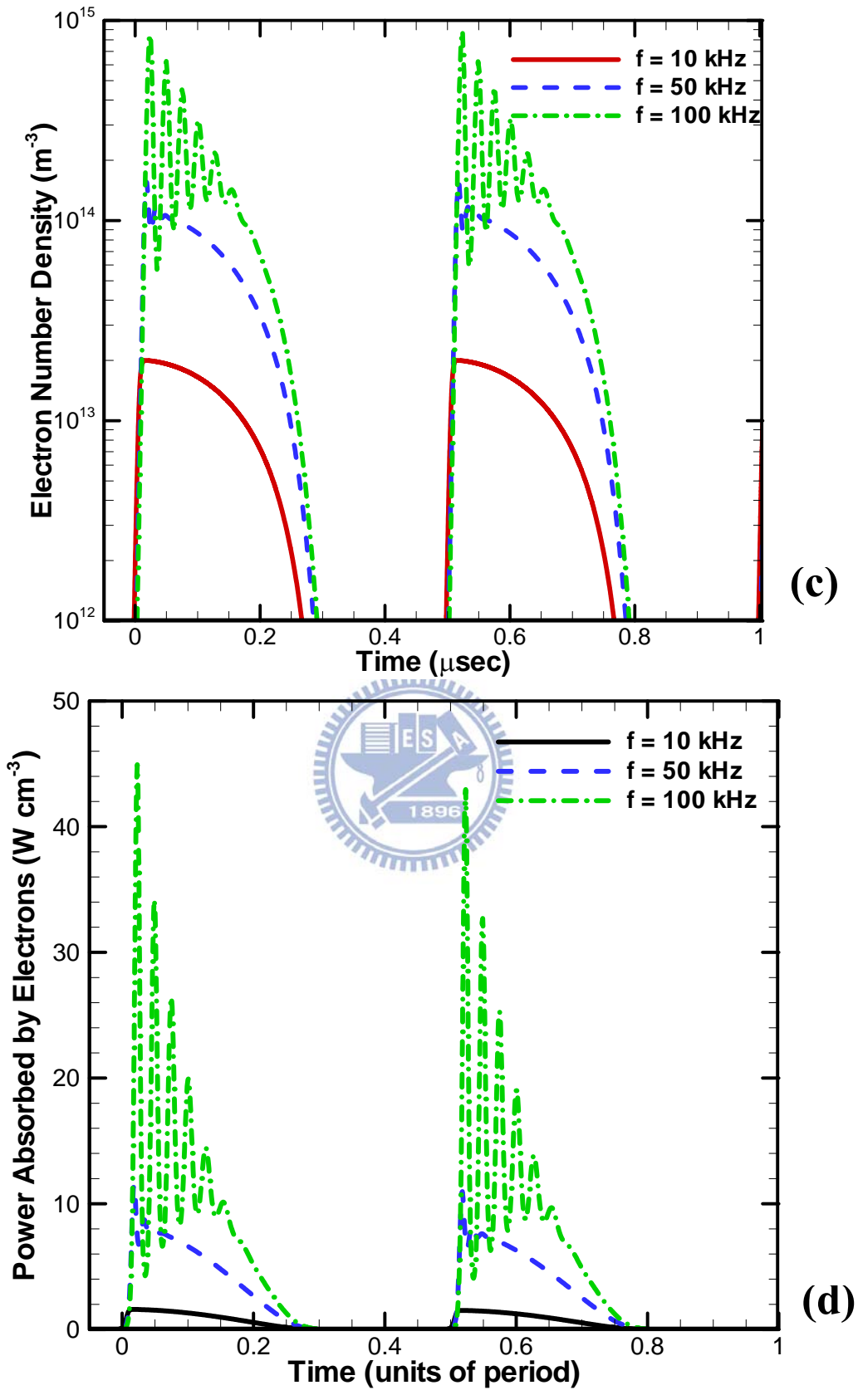


Figure 19. Temporal variation of discharge properties: (a) discharge current density, (b) gap voltage, (c) electron number density, and (d) power absorbed by electrons with various frequencies of applied voltage.

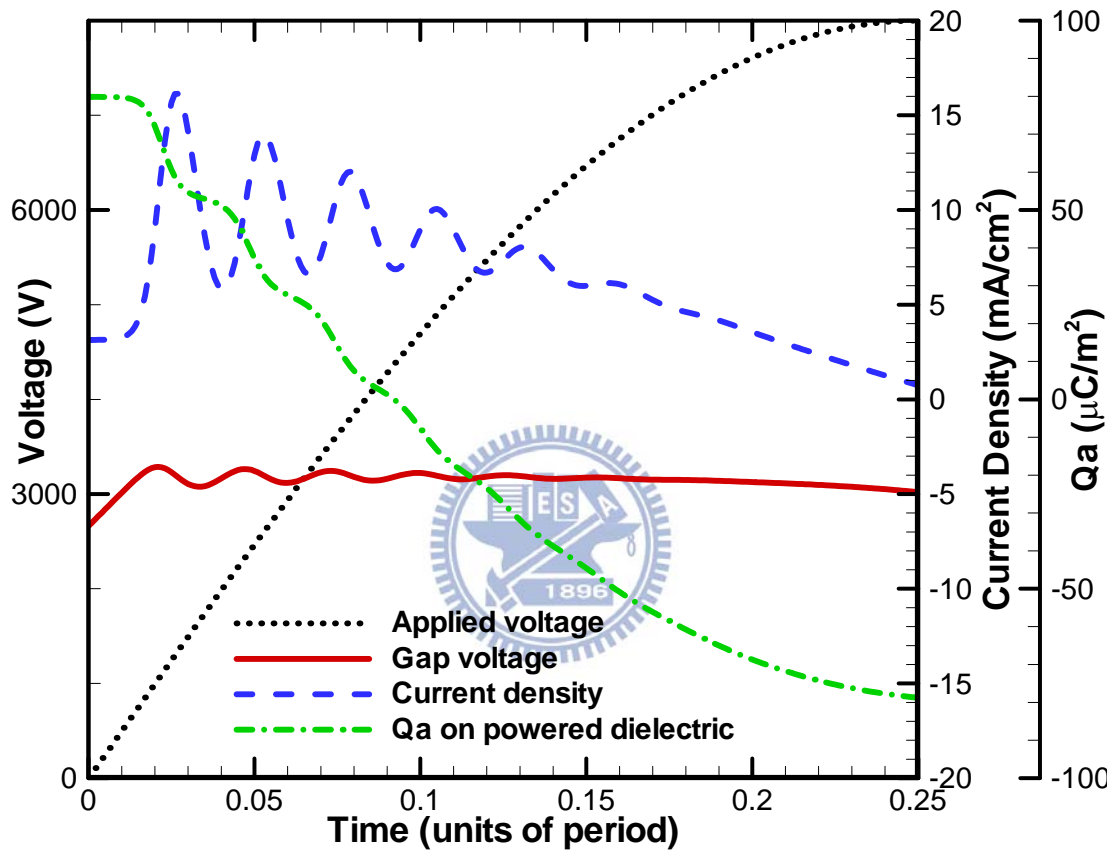
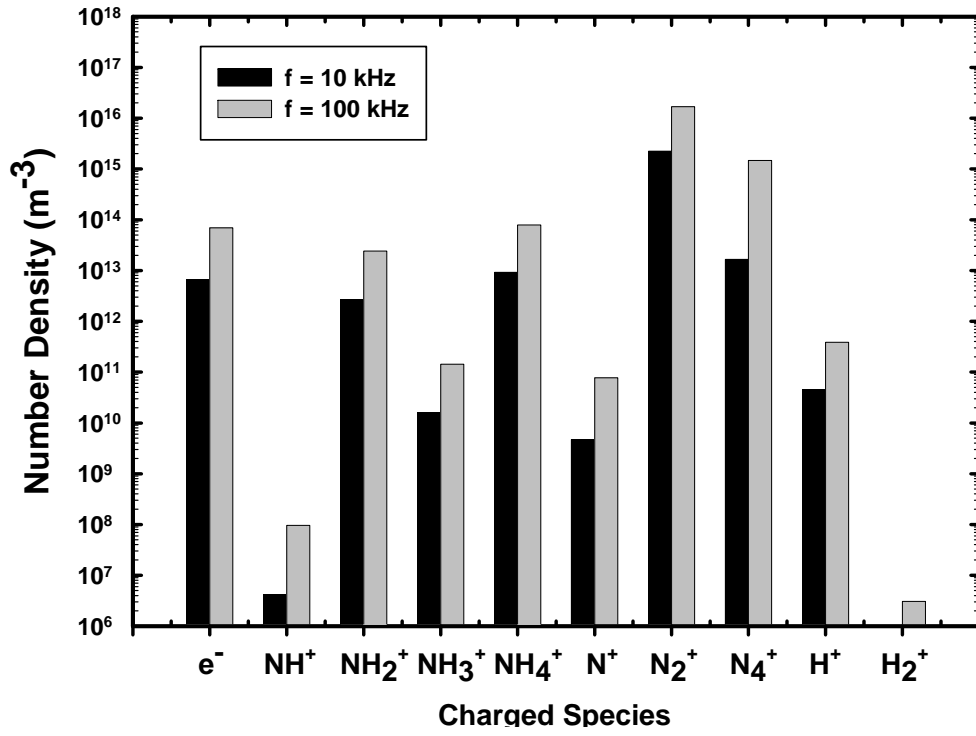
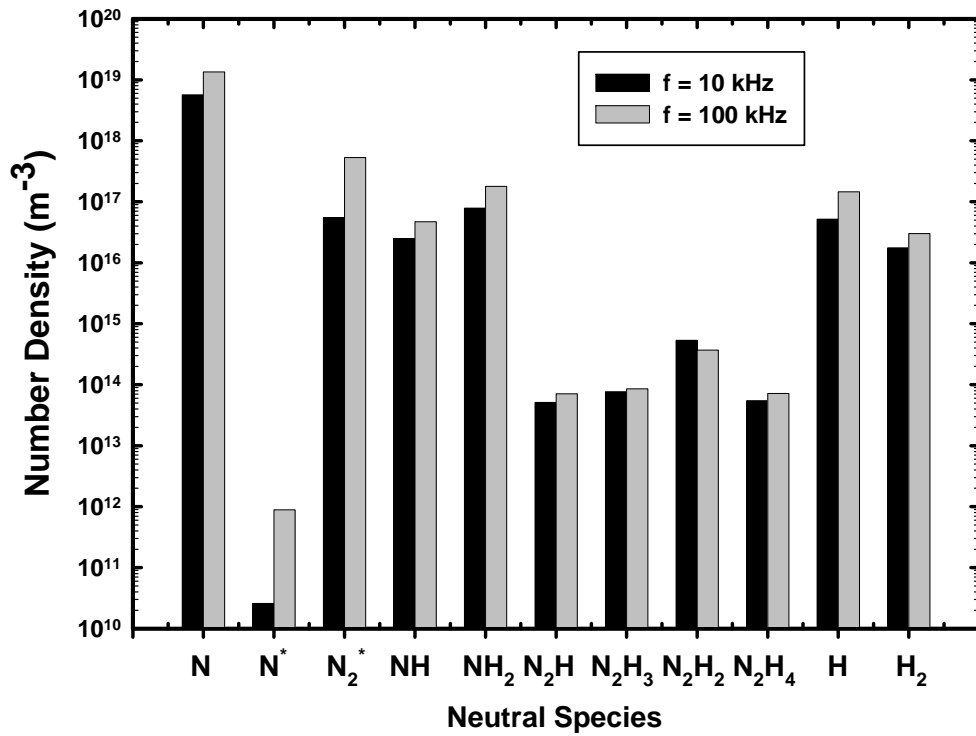


Figure 20. Temporal variation of accumulated charge on powered dielectric (Q_a) at 100 kHz of frequency of applied voltage.



(a)



(b)

Figure 21. Spatiotemporal averaged number densities of (a) charged species and (b) neutrals with various frequencies.

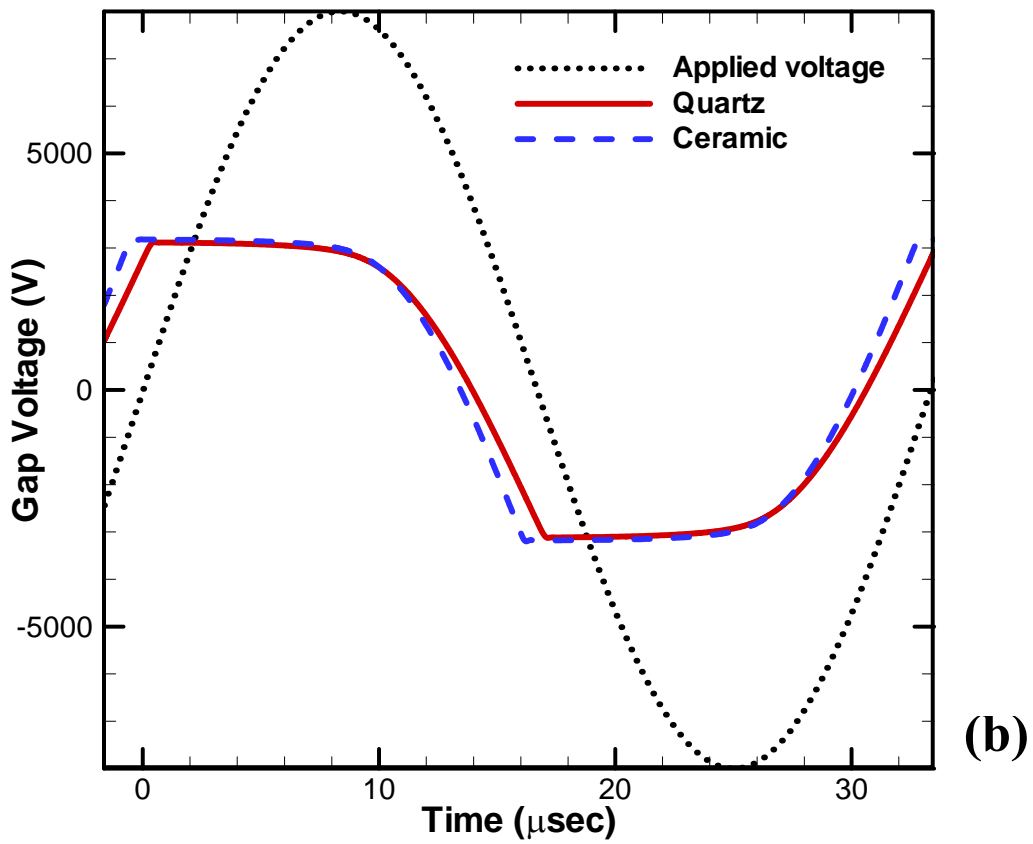
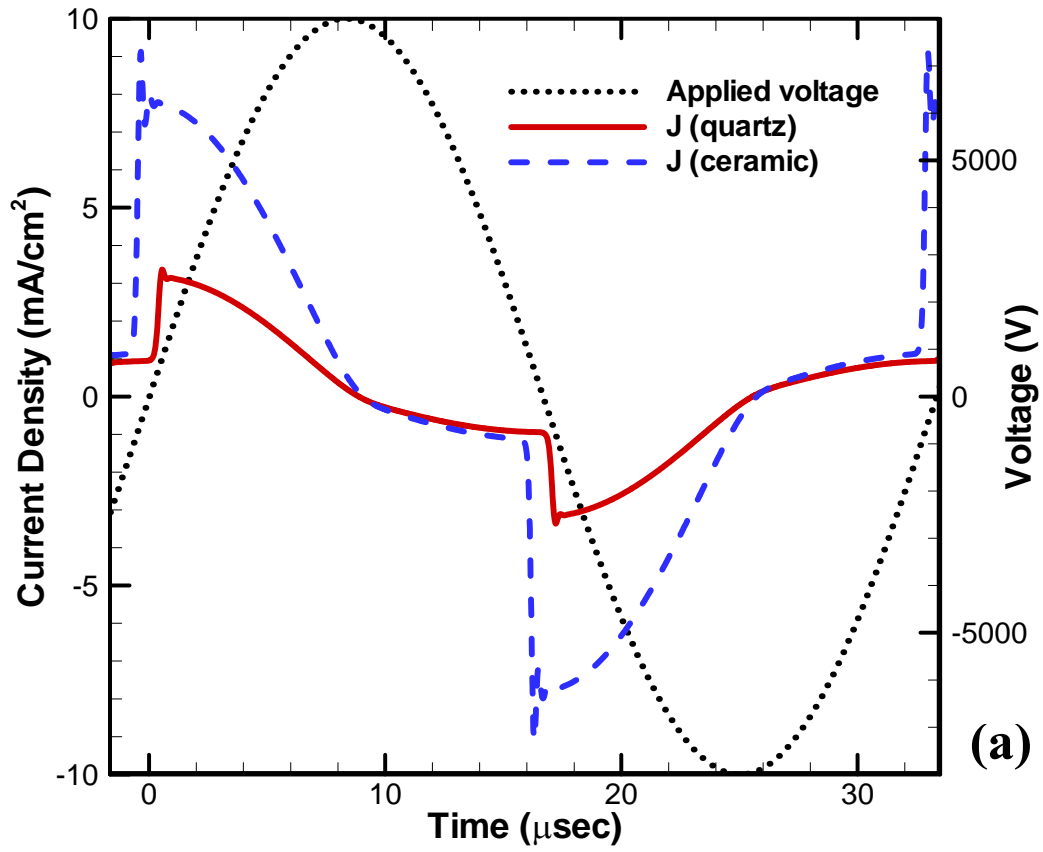
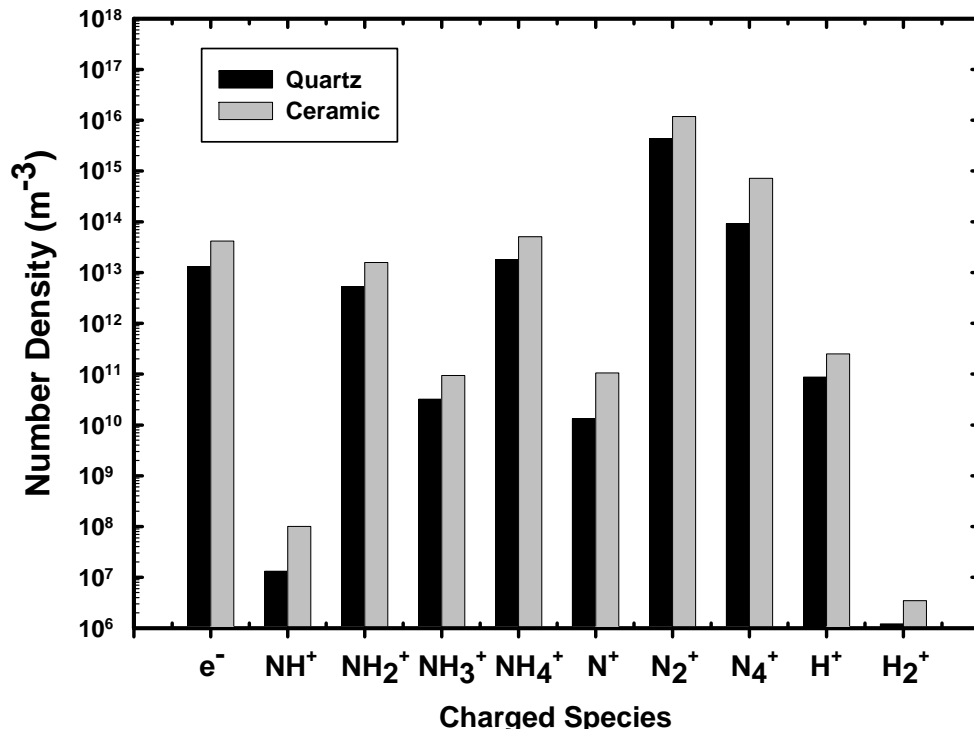
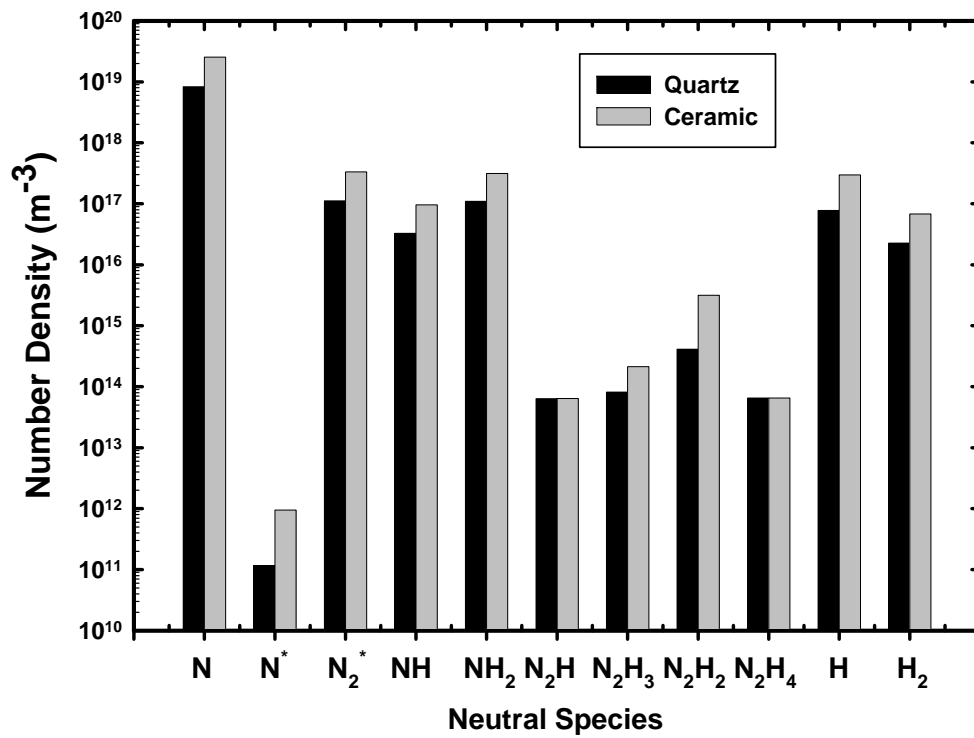


Figure 22. Temporal variation of (a) discharge current density and (b) gap voltage with various dielectric materials.



(a)



(b)

Figure 23. Spatiotemporal averaged number densities of (a) charged species and (b) neutrals with various dielectric materials.

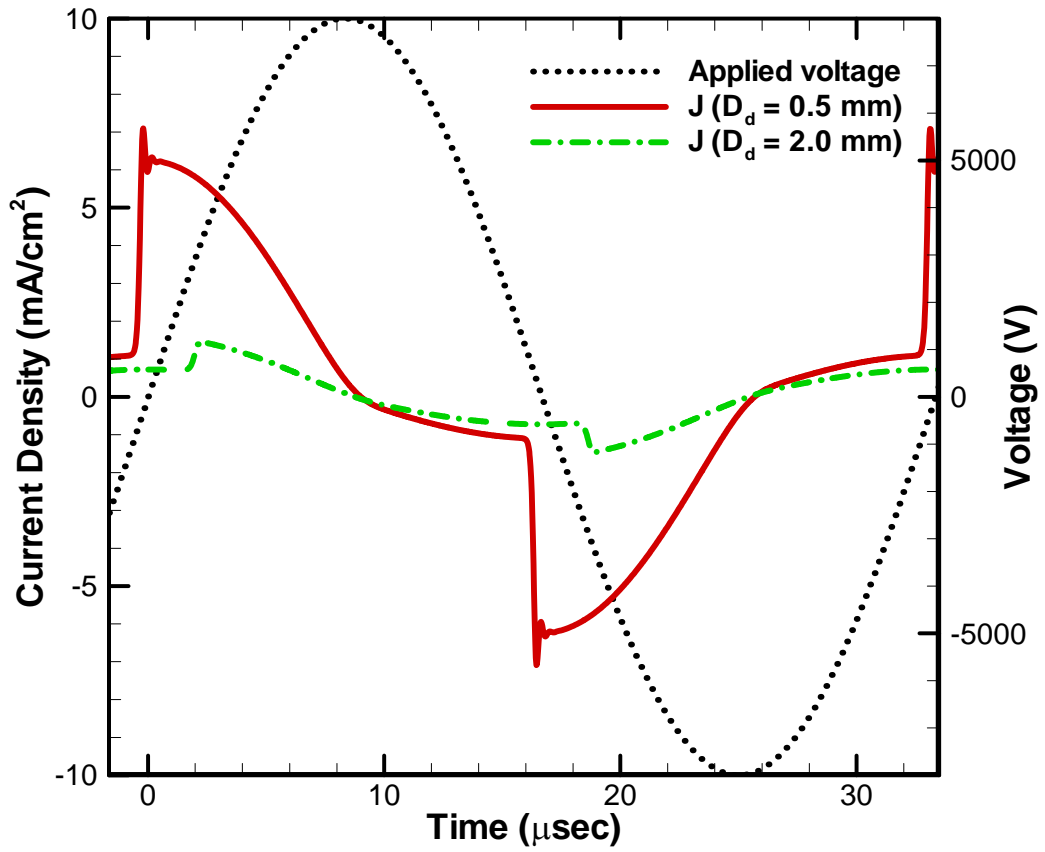
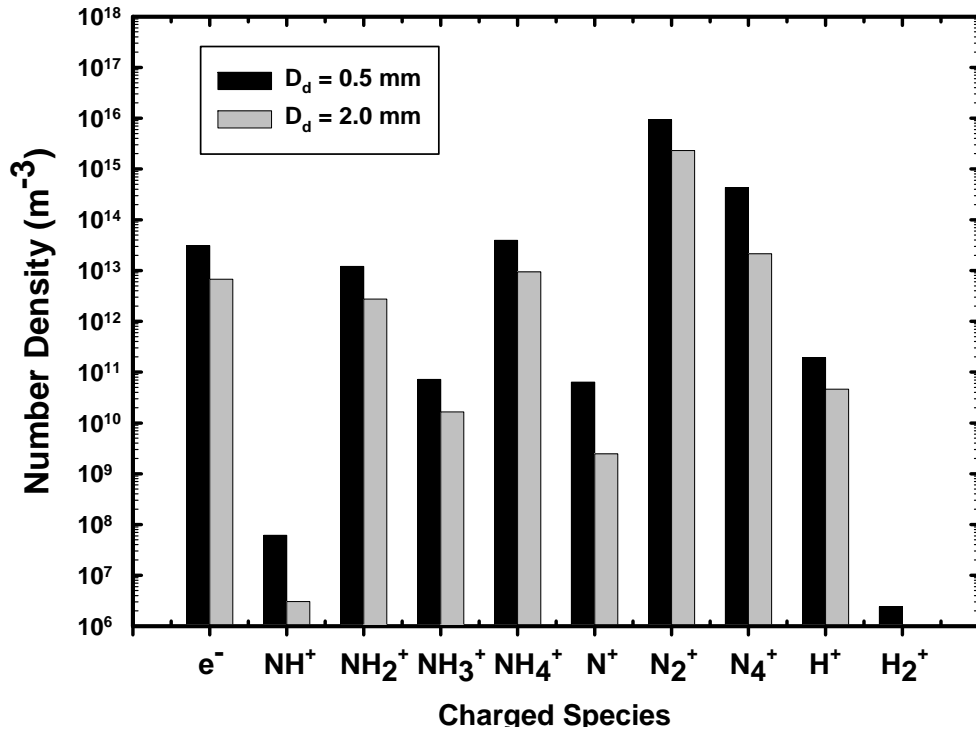
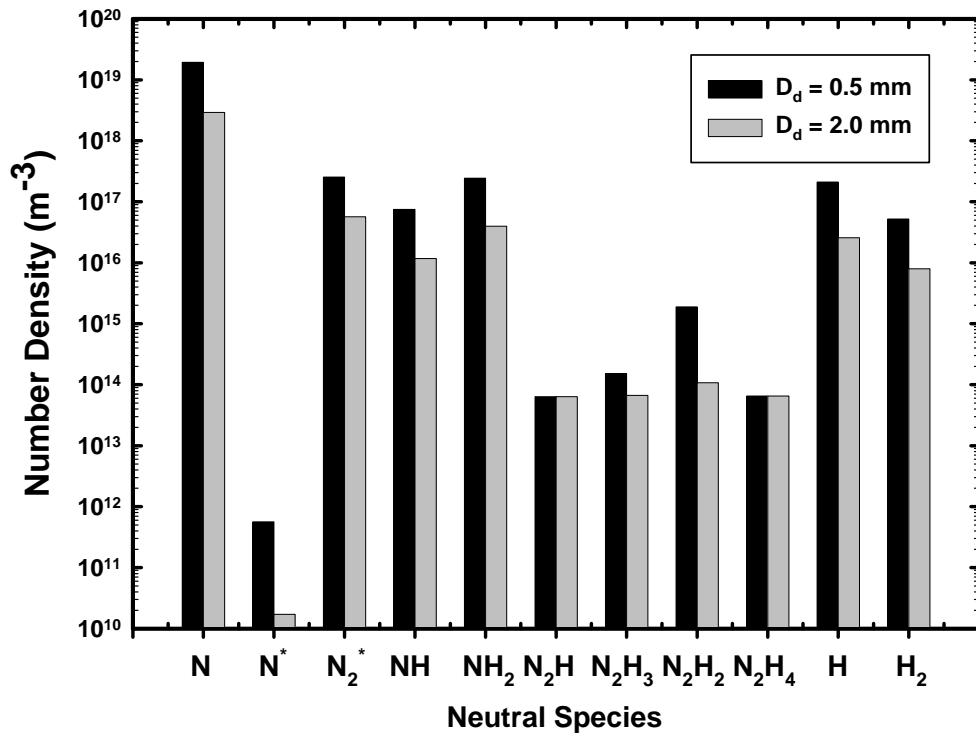


Figure 24. Temporal variation of discharge current density for various dielectric thicknesses.



(a)



(b)

Figure 25. Spatiotemporal averaged number densities of (a) charged species and (b) neutrals for various dielectric thicknesses.

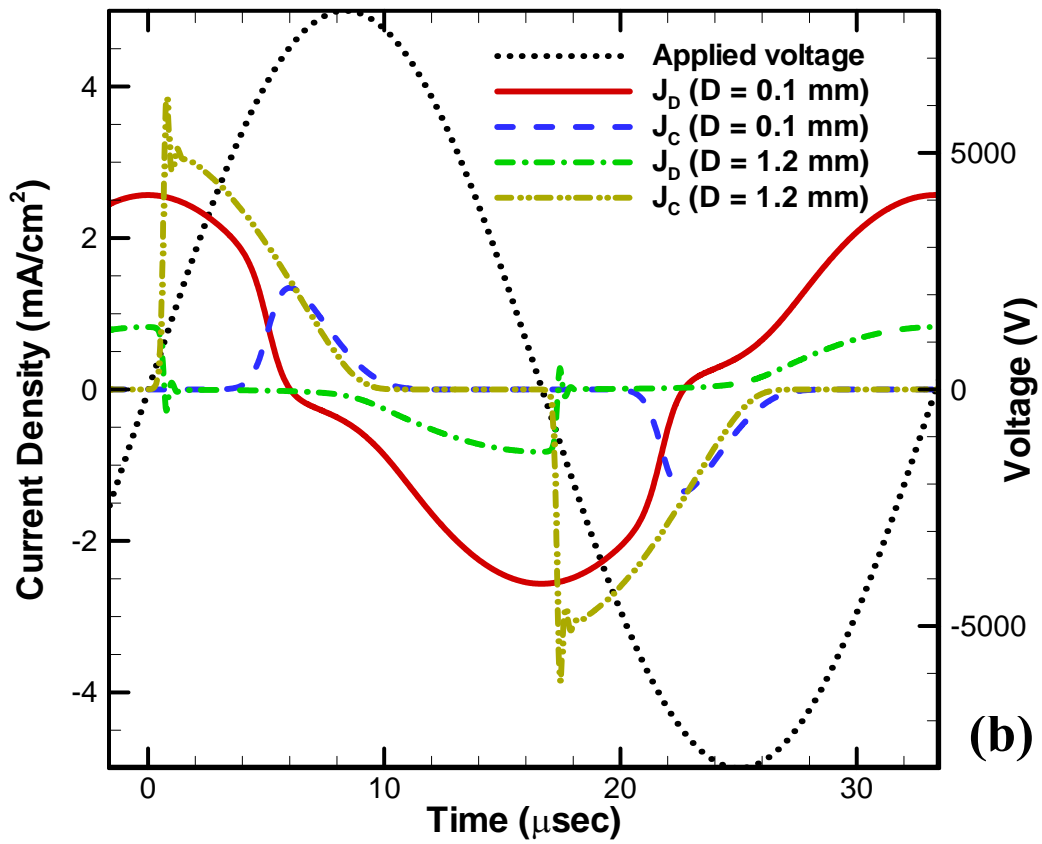
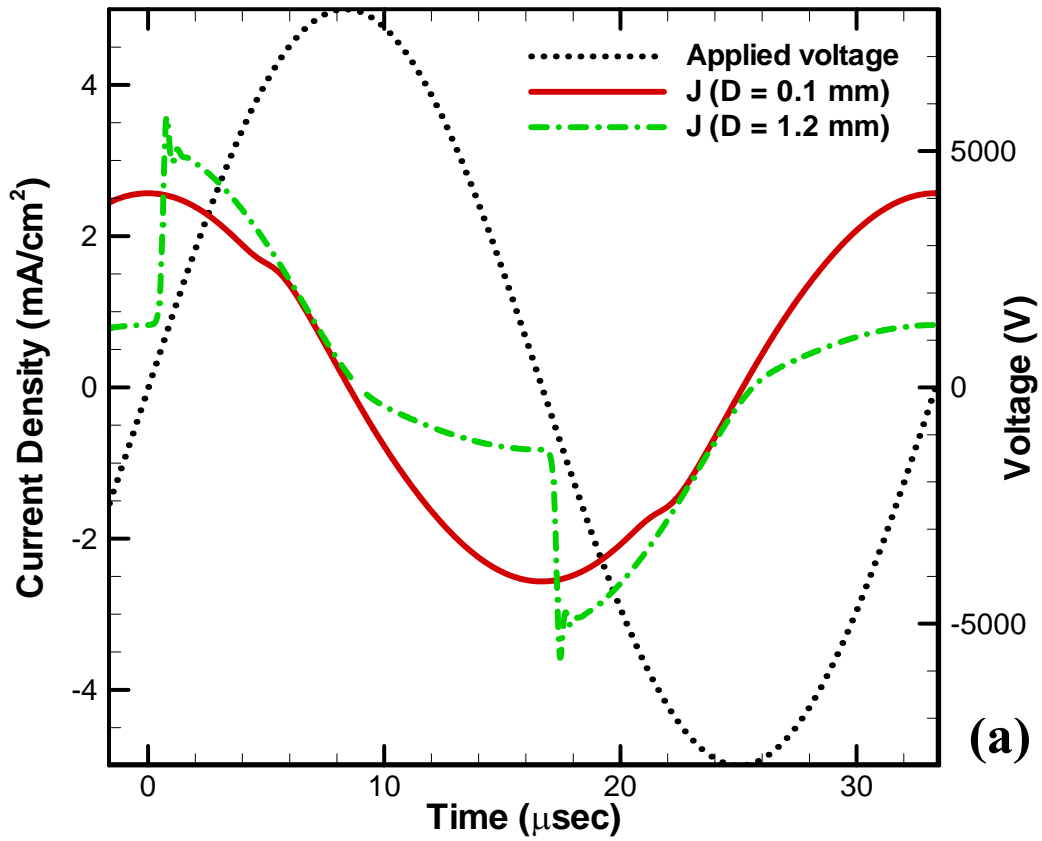
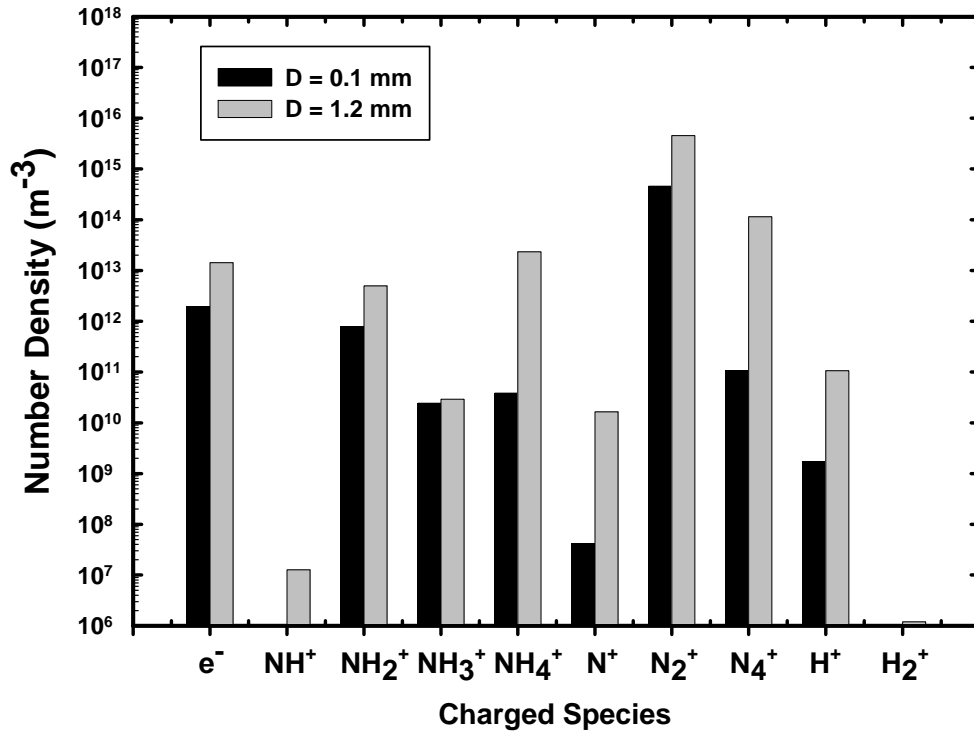
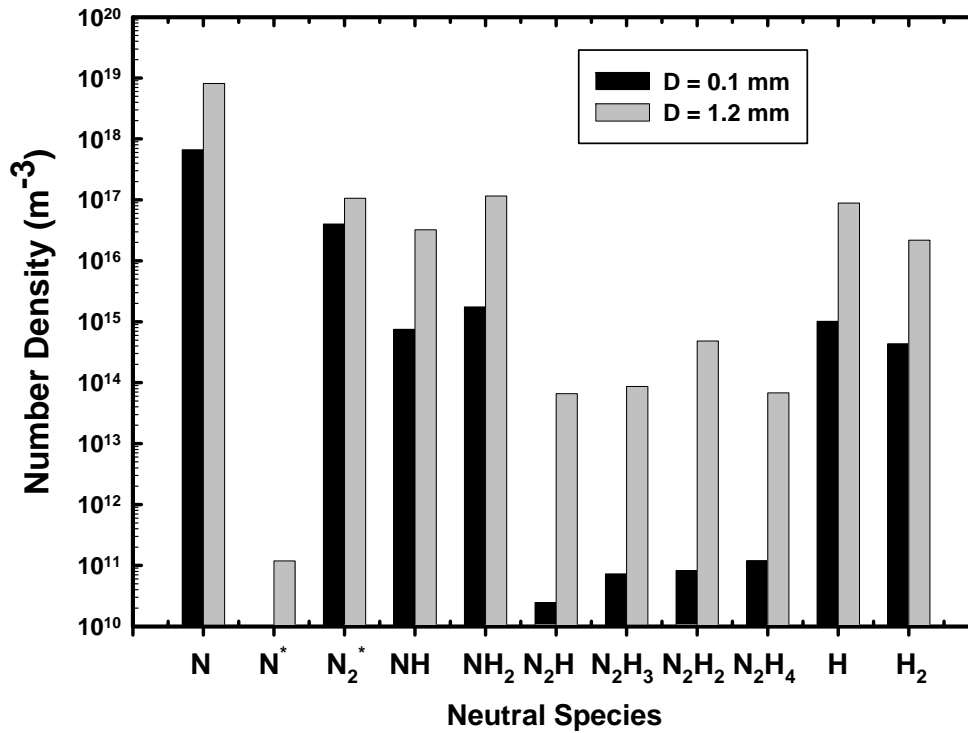


Figure 26. Temporal variation of (a) current density and (b) displacement (J_D) and conduction current density (J_C) at various gap distances.



(a)



(b)

Figure 27. Spatiotemporal averaged number densities of (a) charged species and (b) neutrals for various gap distances.

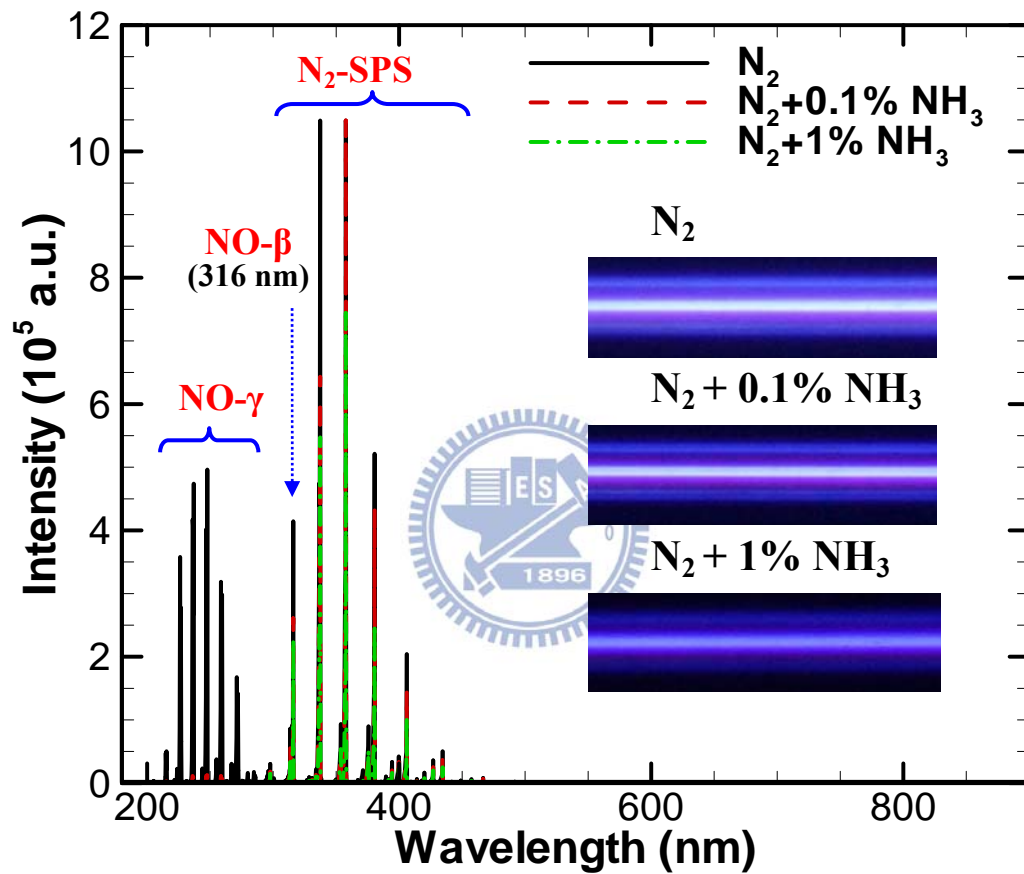


Figure 28. Optical emission spectra of N₂/(0-1%)NH₃ AP-DBD from 180 to 900 nm under experimental conditions (30 kHz, 8 kV, 50 SLM, 400W).

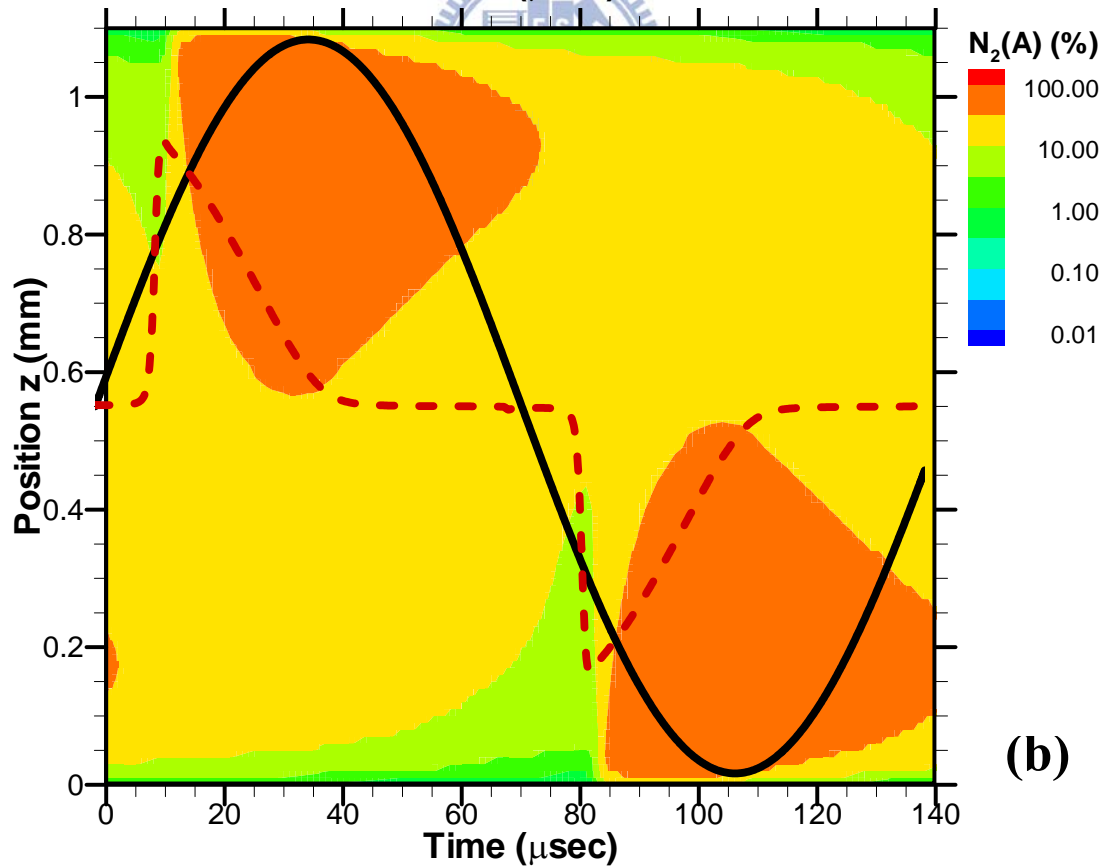
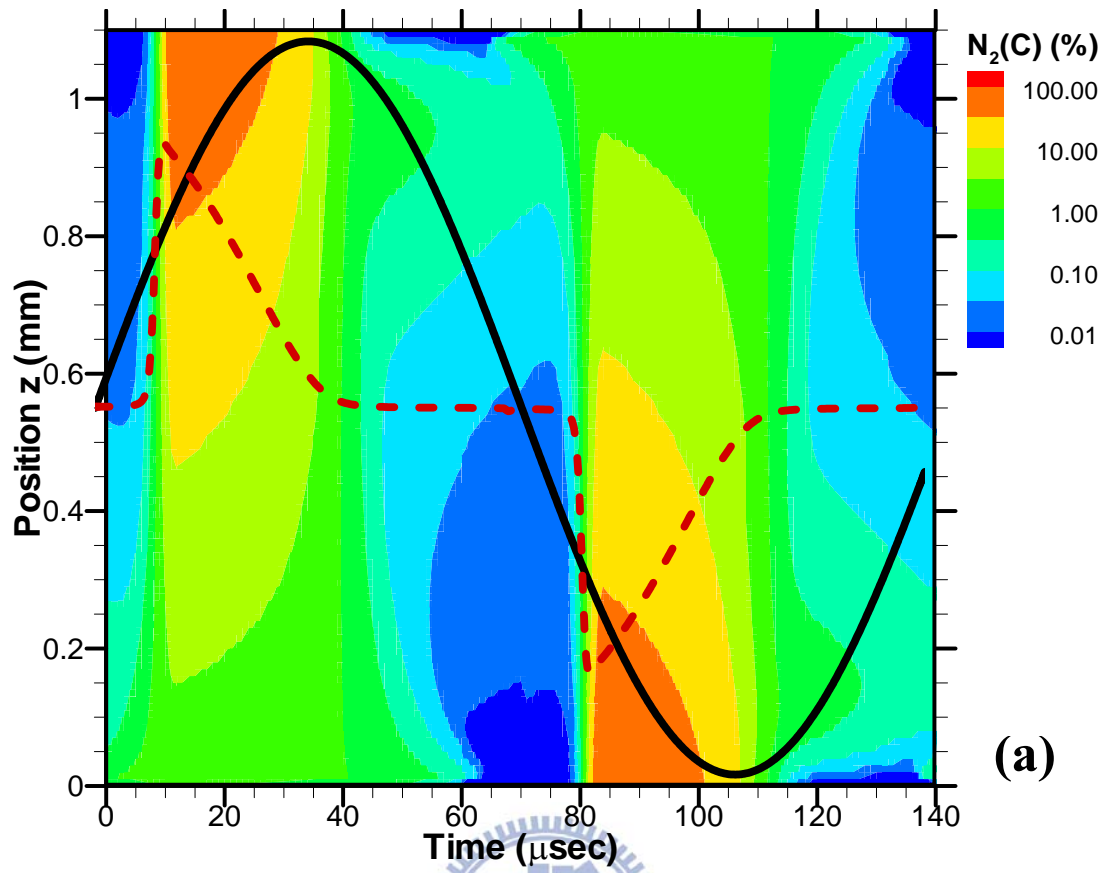


Figure 29. Spatiotemporal distributions of (a) $N_2(C)$ and (b) $N_2(A)$ under same conditions as Brandenburg's experimental conditions [34].

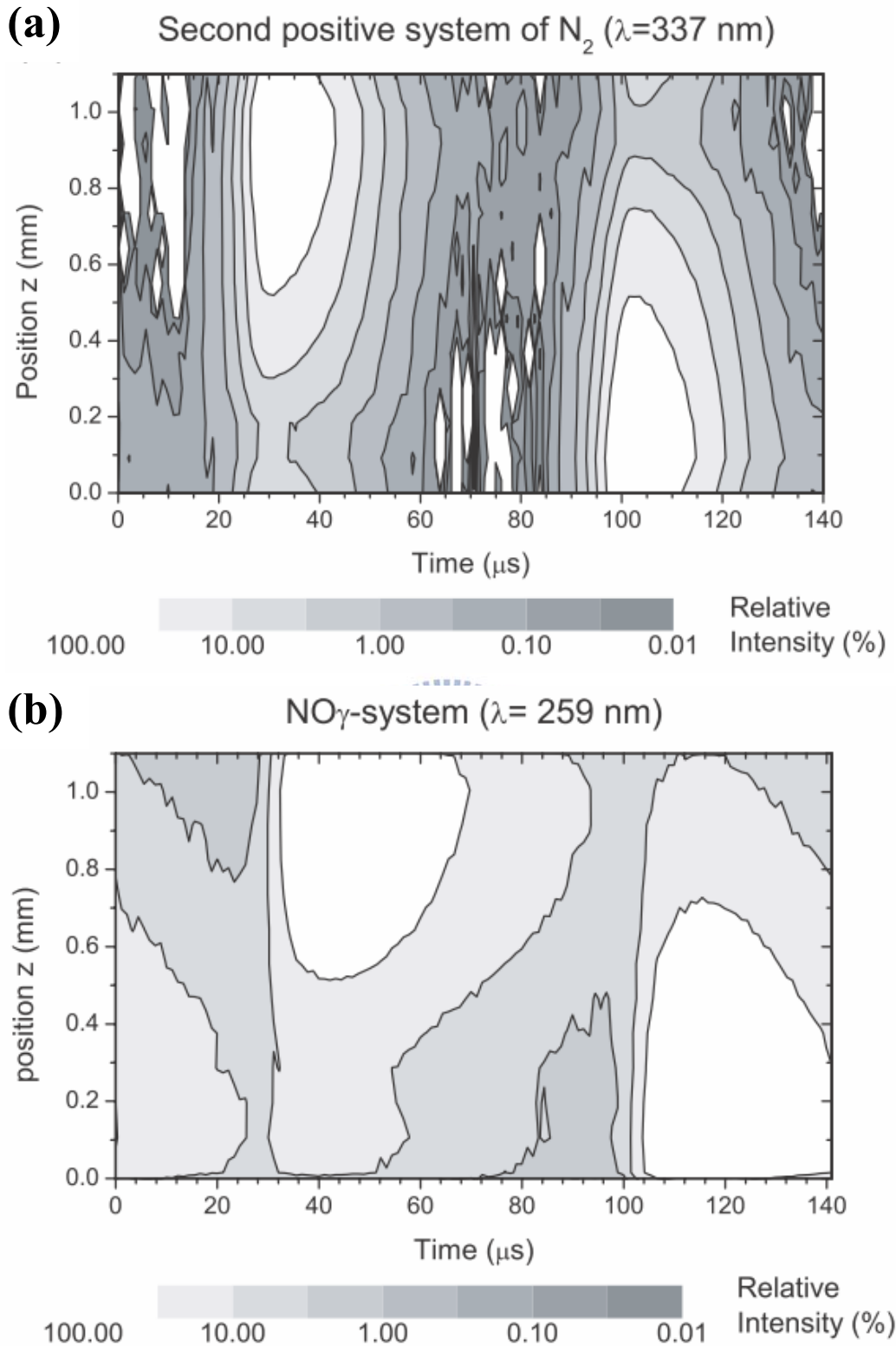


Figure 30. Spatiotemporal intensity distributions of (a) N_2 -SPS and $NO\gamma$ were measured in the gas mixture of 300ppm O_2 in N_2 by Brandenburg *et al.* [34].

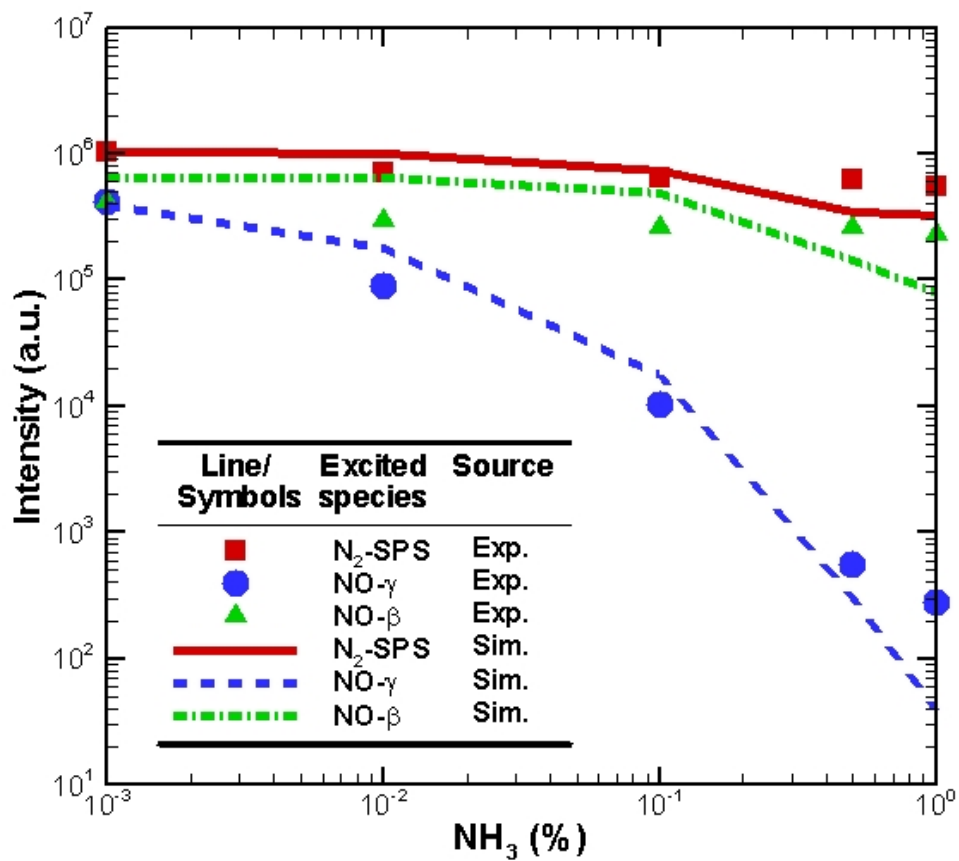
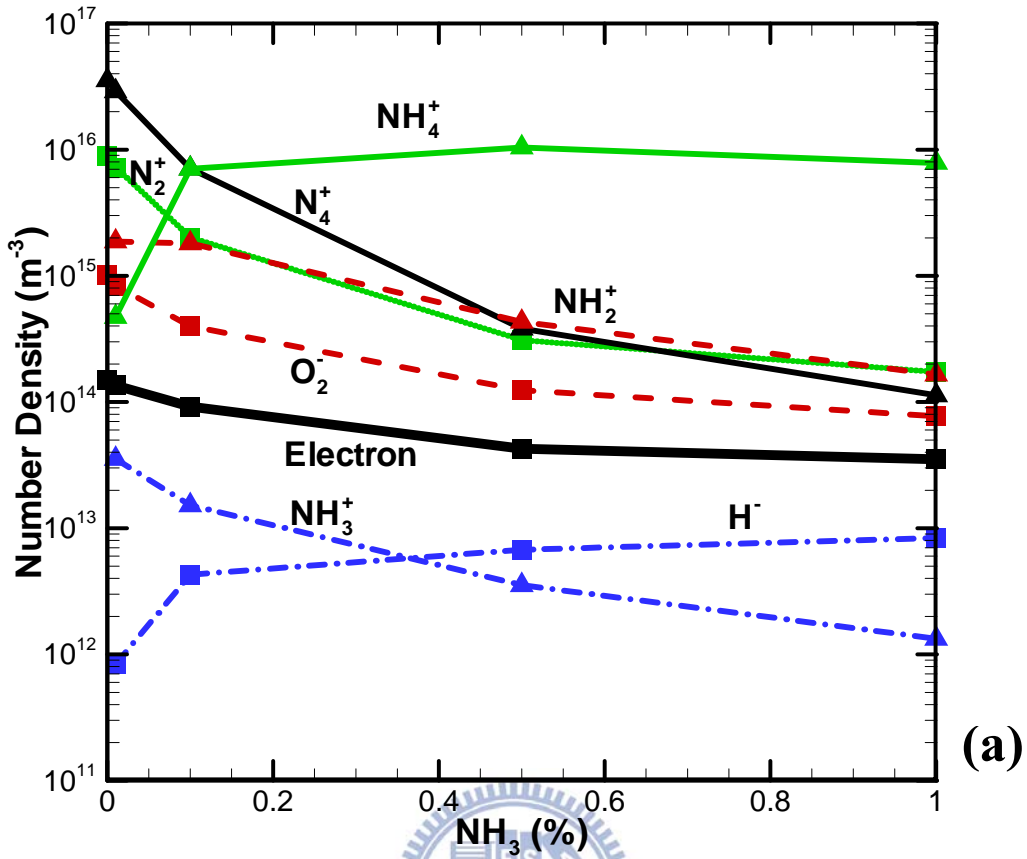
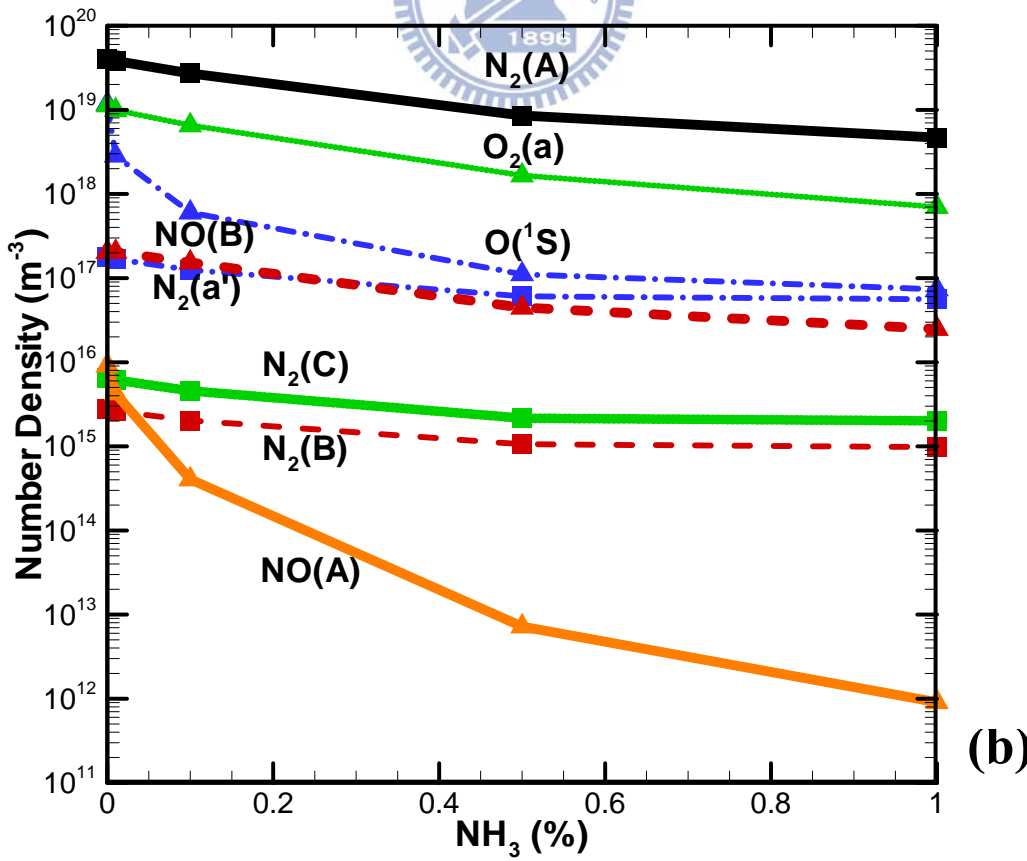


Figure 31. Optical emission spectra comparison of simulations and measurements.

(Note that 0.001% NH₃ really represents 0% NH₃ on the x-axis.)



(a)



(b)

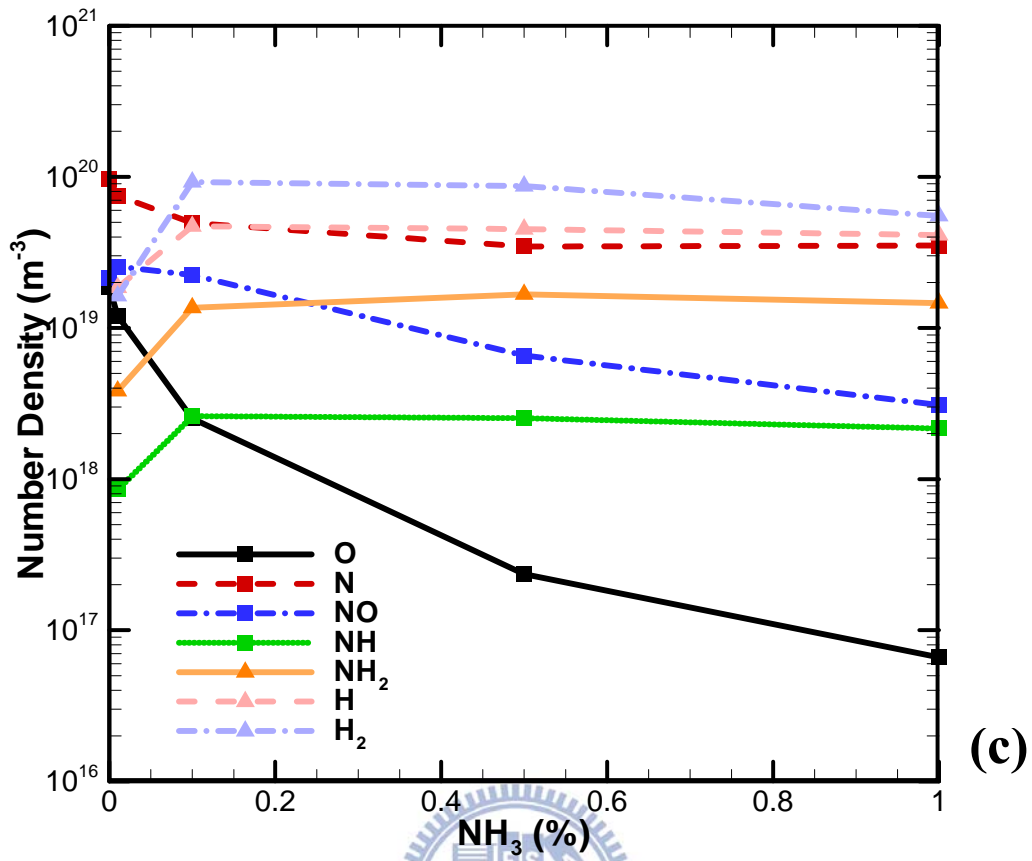


Figure 32. Spatiotemporal averaged number density of (a) charged, (b) excited and (c) neutral species as function of concentration of ammonia from 0 to 1%.

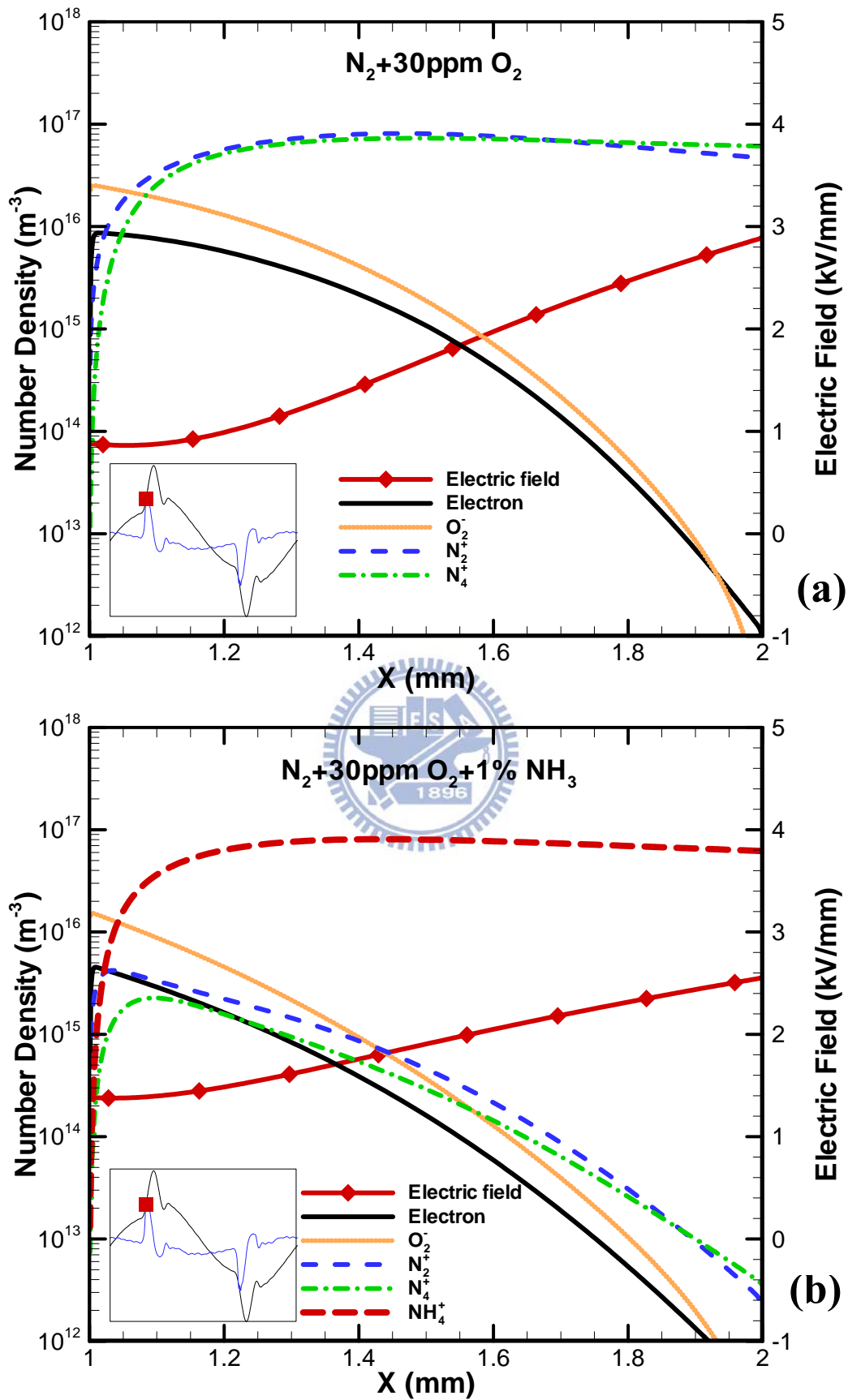


Figure 33. Snapshots of distribution of plasma properties of charged species in (a) $\text{N}_2/30\text{ppm-O}_2$ and (b) $\text{N}_2/30\text{ppm-O}_2/1\% \text{NH}_3$ discharges at maximum current density.

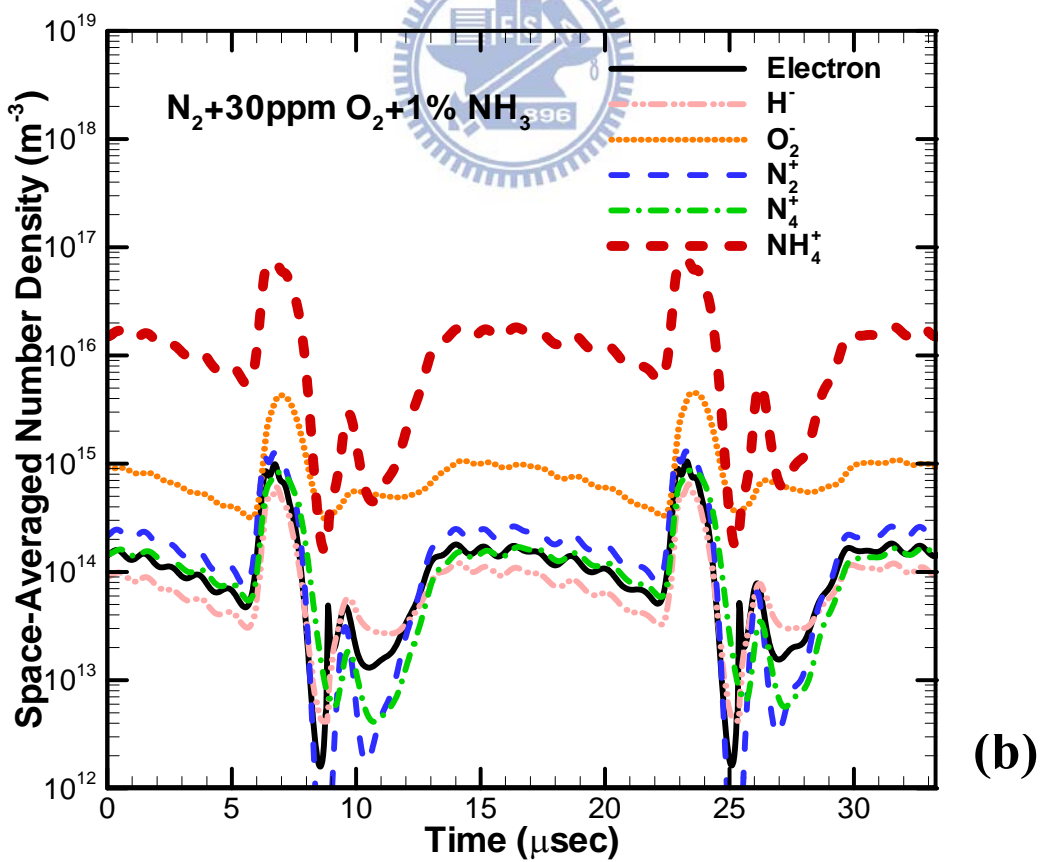
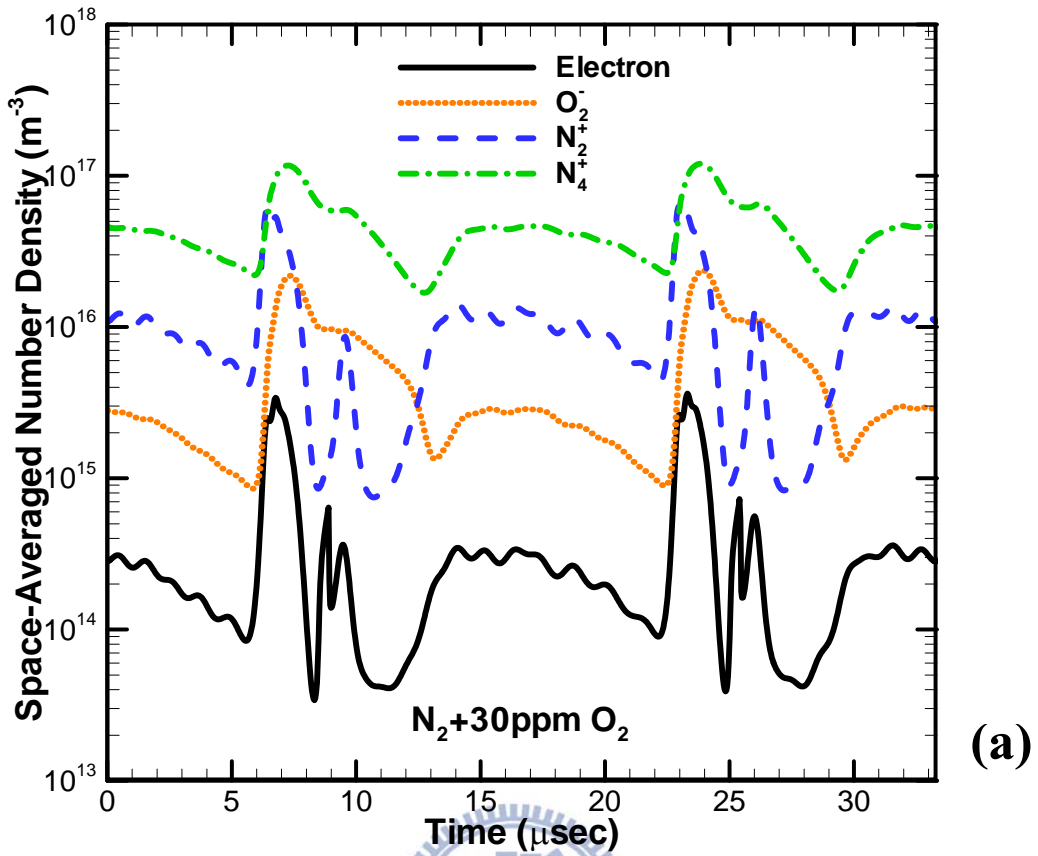


Figure 34. Temporal profiles of space-averaged number densities of charged species in (a) $\text{N}_2/30\text{ppm-O}_2$ and (b) $\text{N}_2/30\text{ppm-O}_2/1\% \text{NH}_3$ discharges in a cycle.

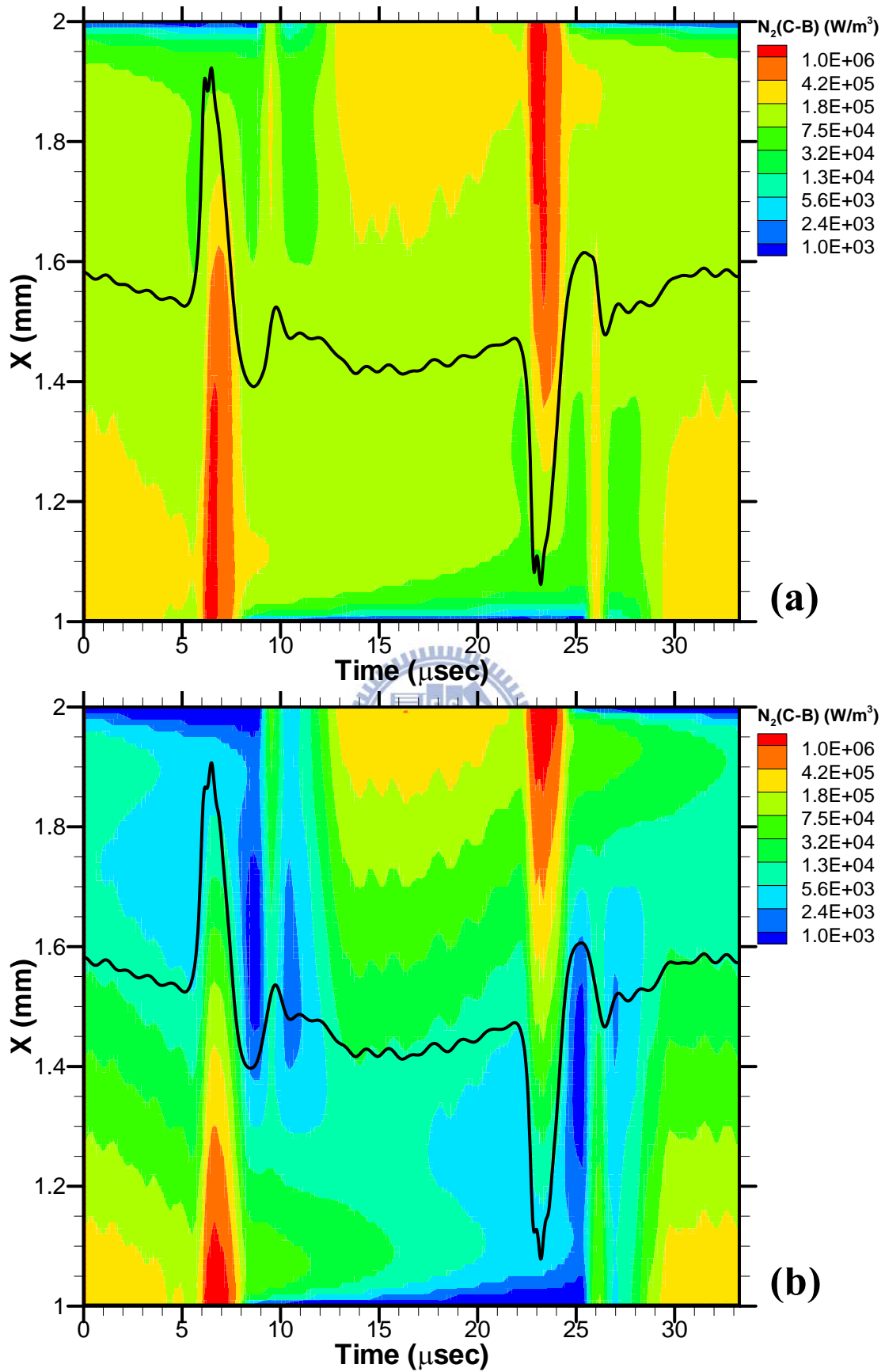


Figure 35. Spatiotemporal distribution of light emission intensity of N_2 -SPS in (a) $N_2/30ppm-O_2$ and (b) $N_2/30ppm-O_2/1\% NH_3$ discharges in a cycle.

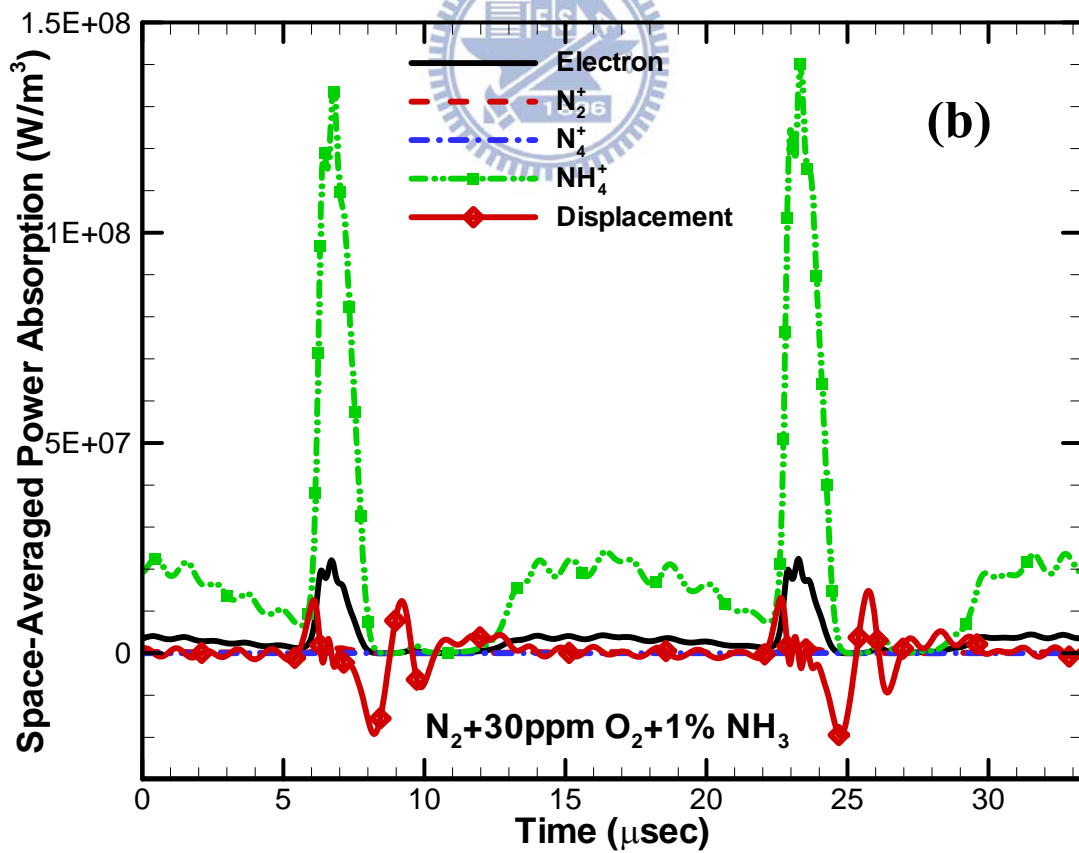
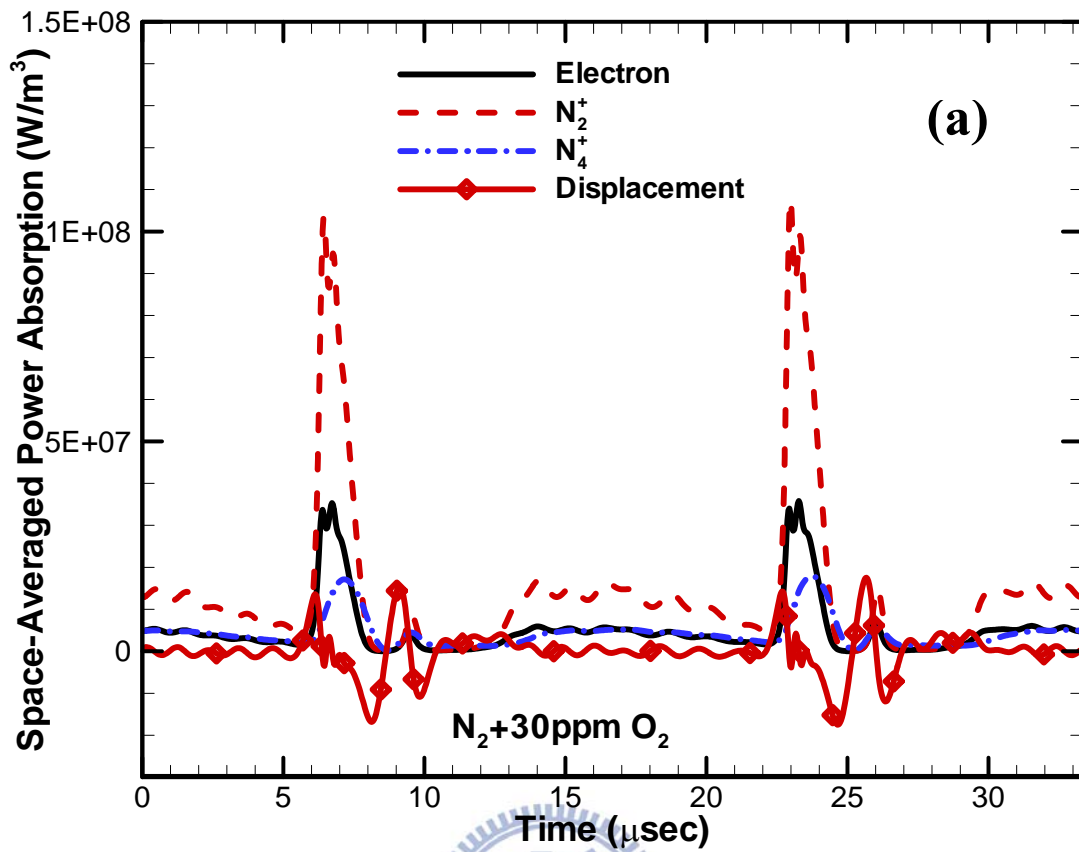


Figure 36. Temporal power absorption in (a) $\text{N}_2/30\text{ppm-O}_2$ and (b) $\text{N}_2/30\text{ppm-O}_2/1\%$ NH_3 discharges.

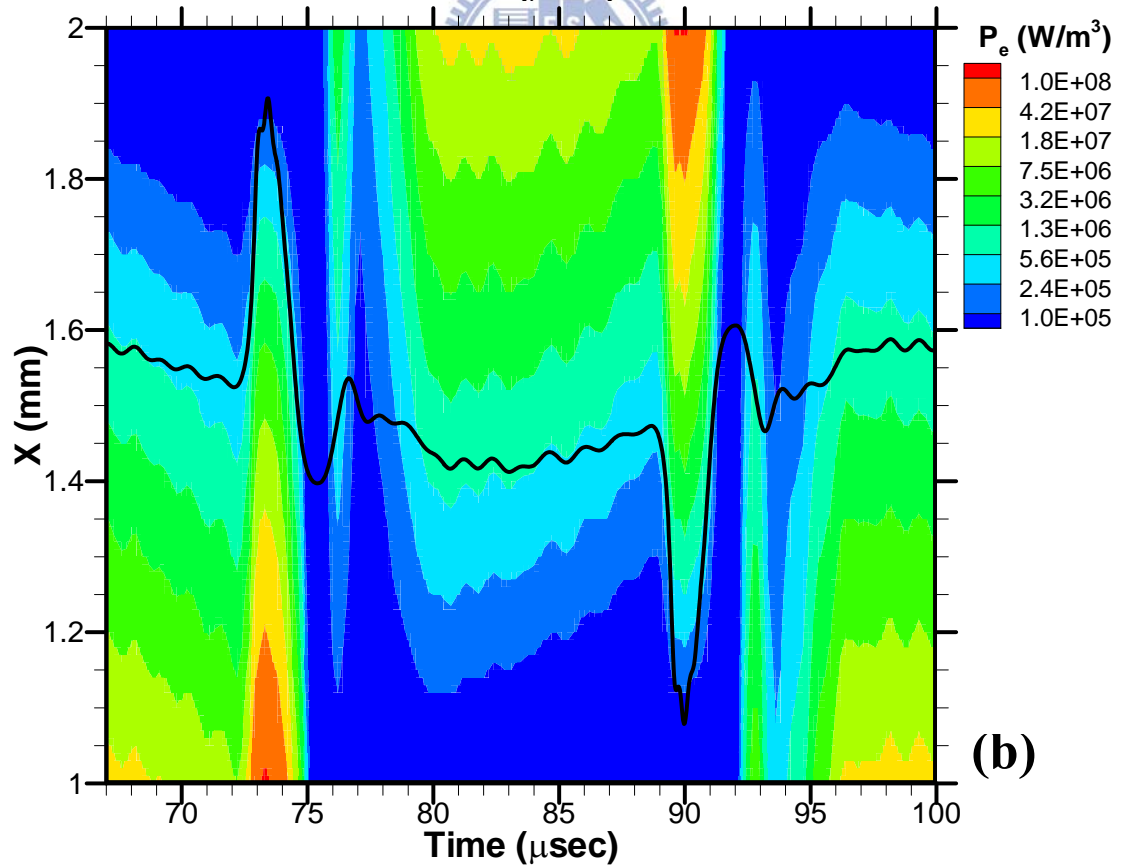
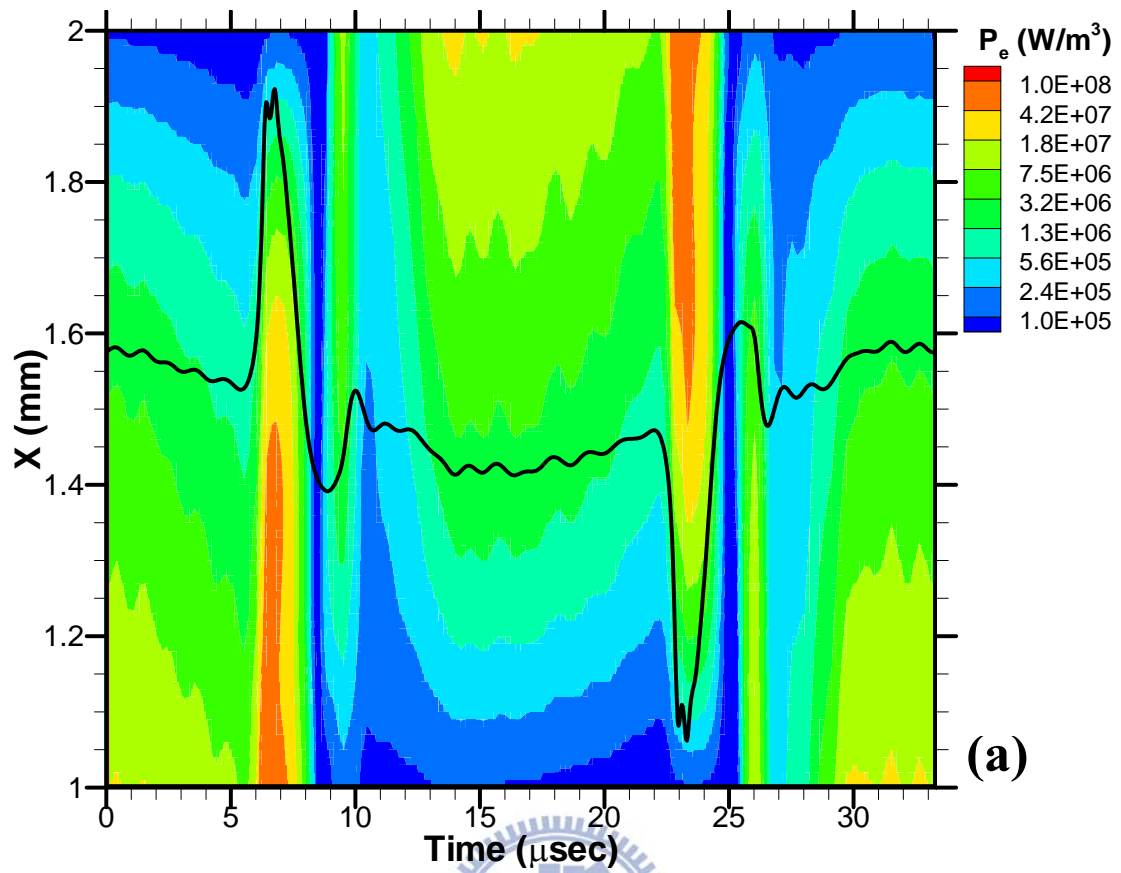


Figure 37. Spatiotemporal distribution of electron power absorption in (a) $N_2/30\text{ppm-O}_2$ and (b) $N_2/30\text{ppm-O}_2/1\% \text{NH}_3$ discharges in a cycle.

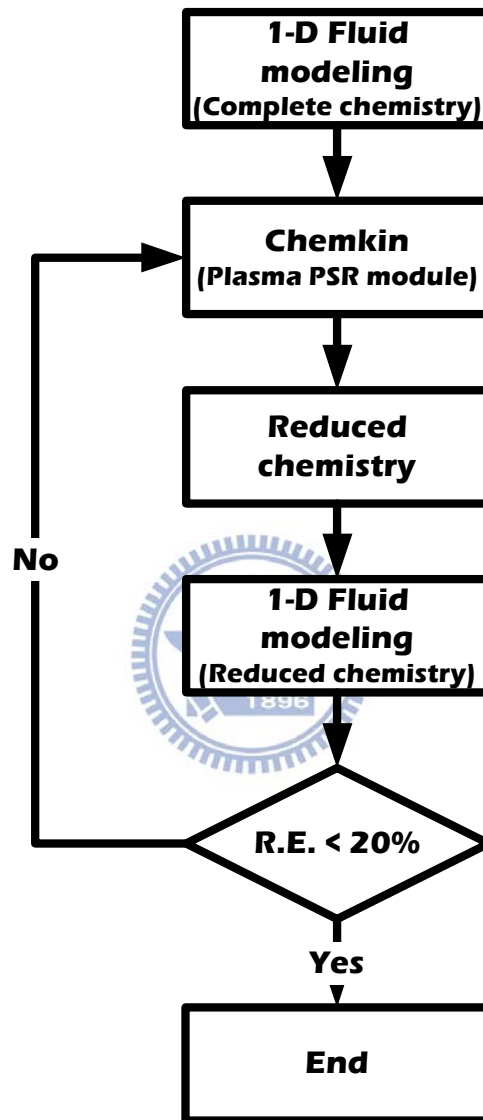


Figure 38. The flowchart of reduced chemistry algorithm.

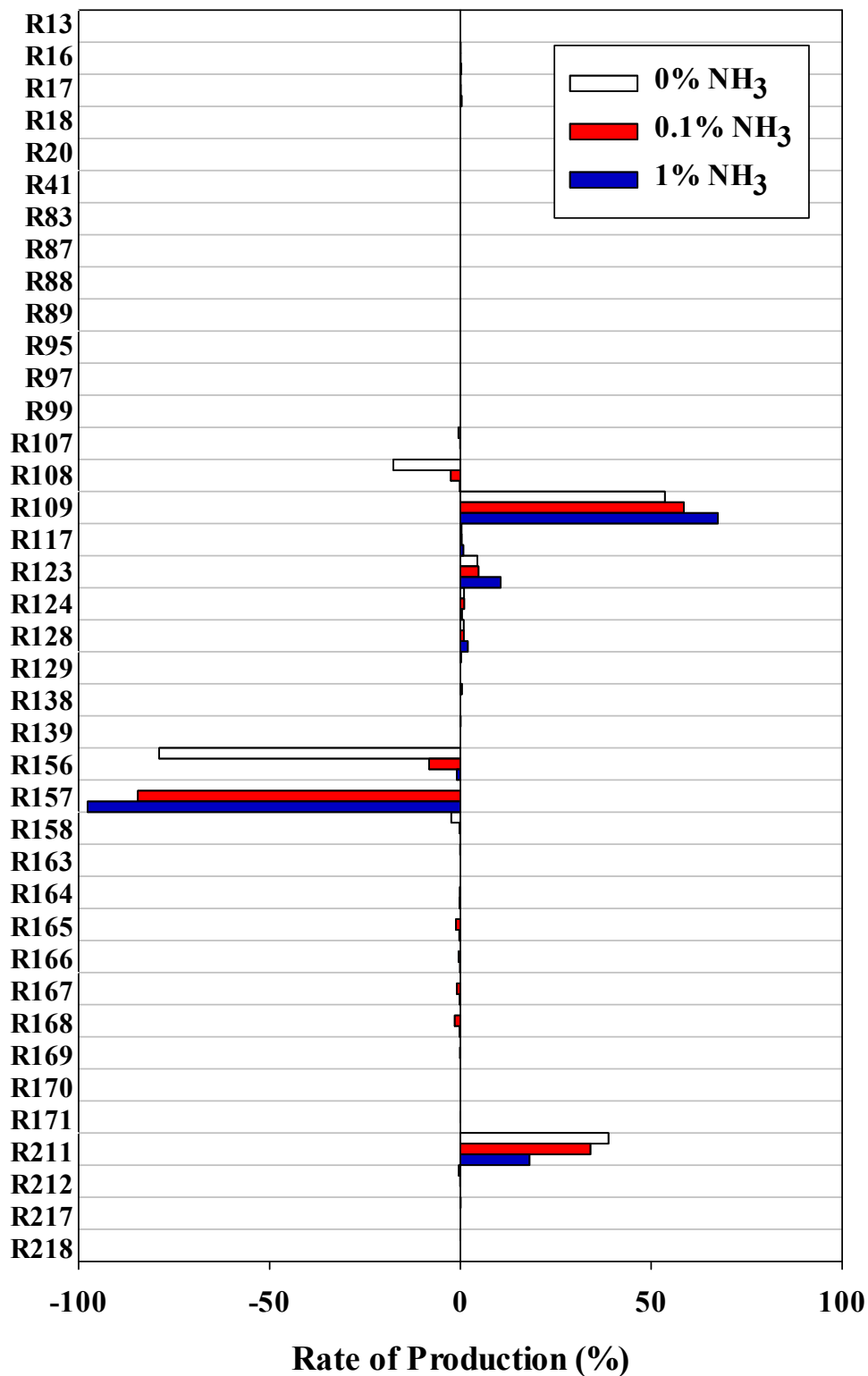


Figure 39. Comparison of rate of production of atomic oxygen among various ammonia concentrations in N₂/O₂ discharges.

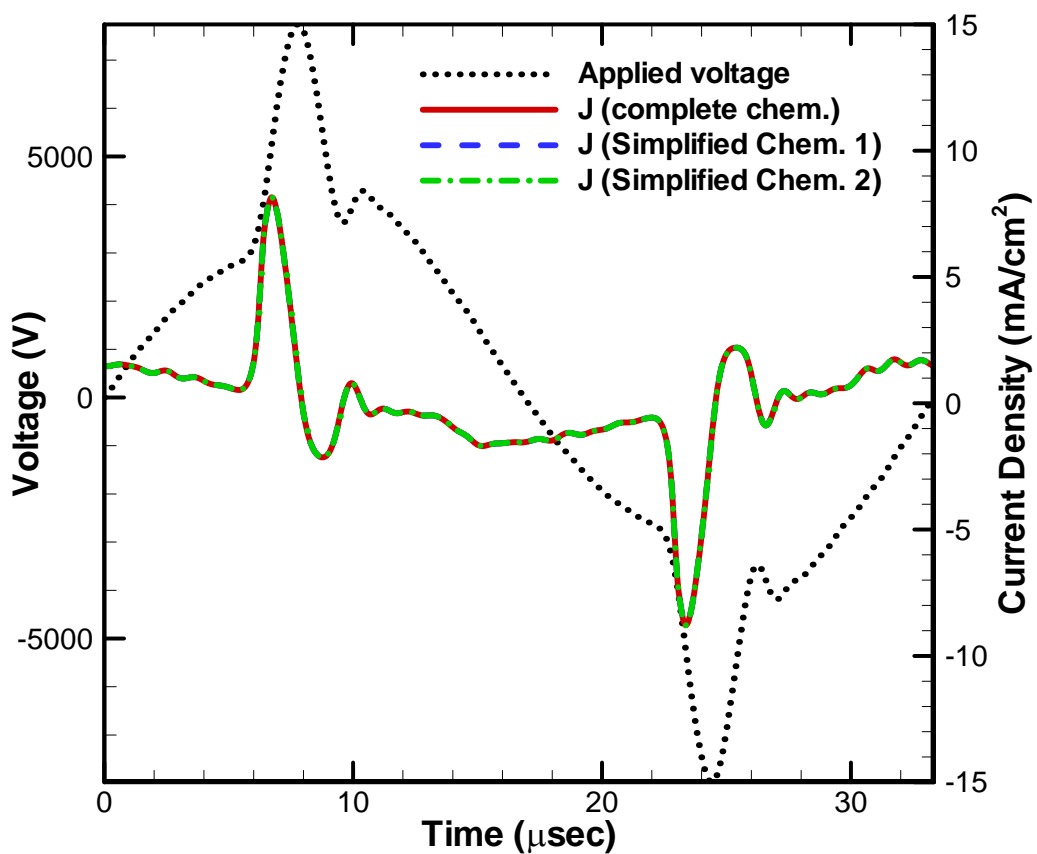


Figure 40. Comparison of discharge current density among various chemical kinetics in $N_2/30\text{ppm-O}_2/0.1\% \text{NH}_3$ discharge.

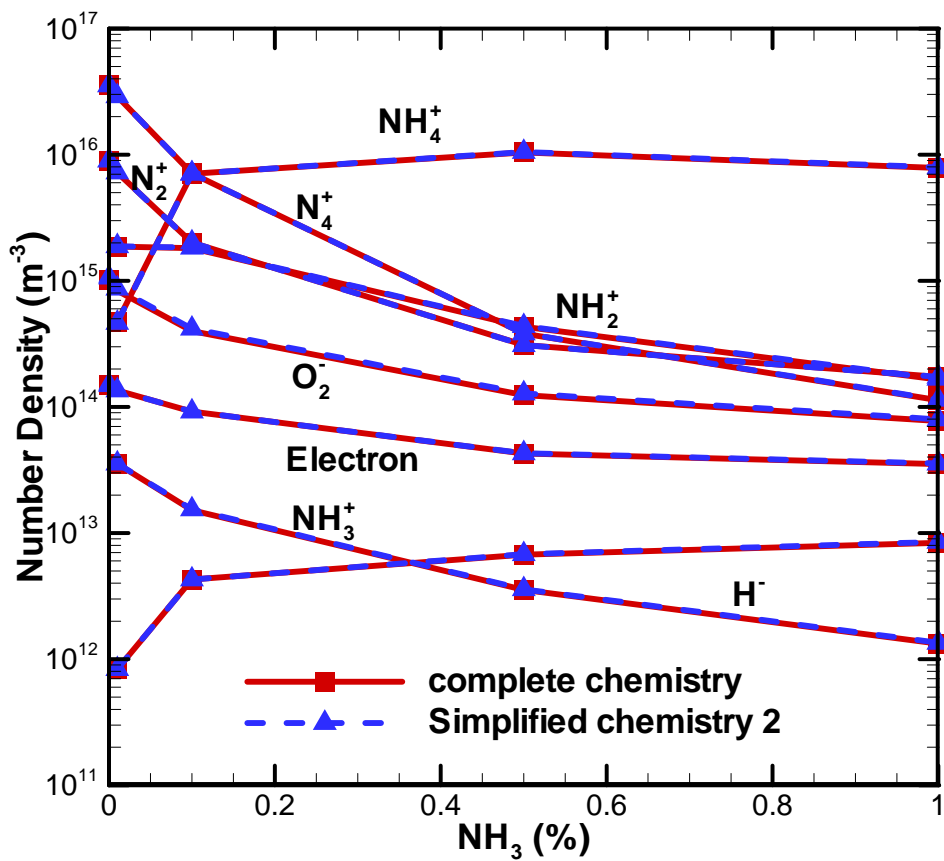


Figure 41. Spatiotemporal averaged number density of charged species comparison of complete chemistry and Simplified Chemistry 2 at various concentrations of ammonia.

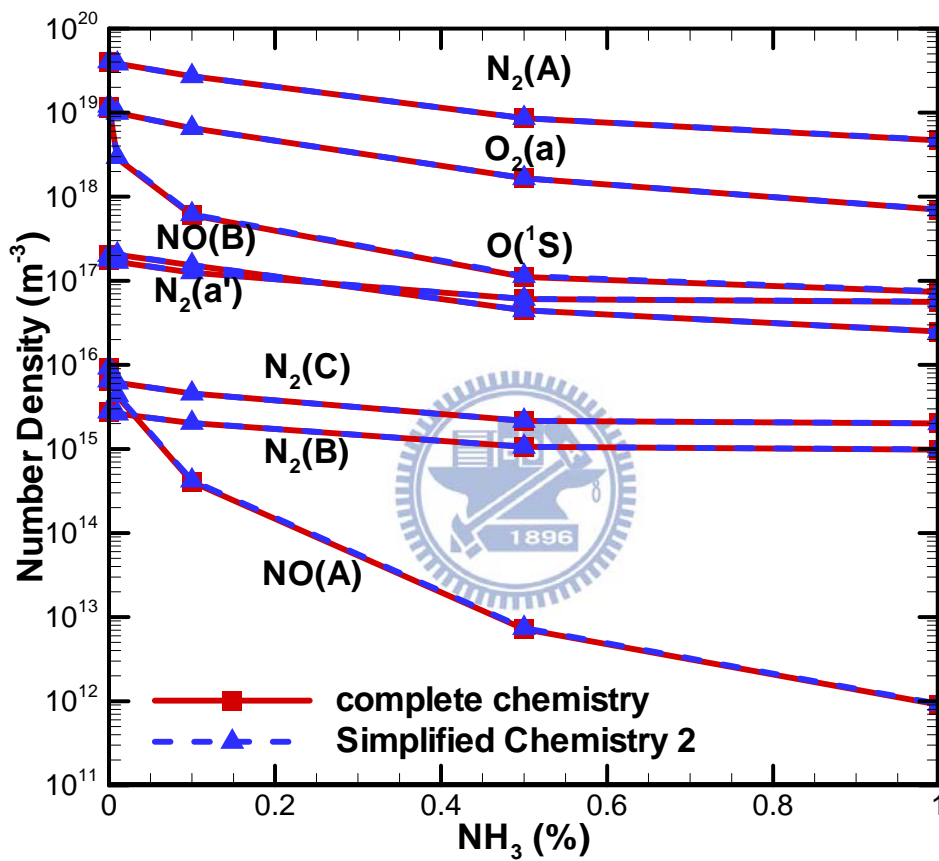


Figure 42. Spatiotemporal averaged number density of excited species comparison of complete chemistry and Simplified Chemistry 2 at various concentrations of ammonia.

List of Publications

Journal Papers: (*corresponding author)

1. J.-S. Wu*, K.-H. Hsu, **F.-L. Li**, C.-T. Hung and S.-Y. Jou, “Development of a parallelized 3D electrostatic PIC-FEM code and its applications,” Computer Physics Communications, Vol. 177, pp. 98-101, 2007.
2. **F.-L. Li**, K.-M. Lin, Y.-W. Yang, C.-T. Hung, J.-S. Wu*, and J.-P. Yu, “ Numerical Investigation of a Parallel-Plate Atmospheric-Pressure Nitrogen/Ammonia Dielectric Barrier Discharge,” Plasma Chemistry and Plasma Processing, Vol. 31, Number 3, pp. 547-564, 2012.
3. **F.-L. Li**, K.-M. Lin, Y.-W. Yang, C.-T. Hung, J.-S. Wu*, and J.-P. Yu, “One-Dimensional Fluid Modeling of Planar Atmospheric-Pressure Nitrogen Dielectric Barrier Discharge Mixed with Ammonia,” The European Physical Journal D, 2012. (Submitted)
4. **F.-L. Li**, C.-T. Hung , K.-M. Lin, and J.-S. Wu*, “Numerical and Experimental Investigation of Light Emissions of a Planar Nitrogen Atmospheric-Pressure Dielectric Barrier Discharge Due to Addition of Ammonia Considering Oxygen Impurity,” Plasma Sources Science and Technology, 2013. (Preparing)
5. **F.-L. Li**, C.-T. Hung, B.-R. Gu, T.-C. Wei, K.-M. Lin, and J.-S. Wu*, “A Reduced Chemical Kinetics for a Planar Atmospheric-Pressure N₂/O₂/NH₃ Dielectric Barrier Discharge,” Plasma Chemistry and Plasma Processing, 2013. (Preparing)

International Conference Papers: (*corresponding author)

1. J.-S. Wu*, K.-H. Hsu, **F.-L. Li** and C.-T. Hung, “Development of a Parallelized 3D PIC-FEM Code and Its Applications,” Conference on Computational Physics,

Geongju, KOREA, August 28-September 1, 2006.

2. **F.-L. Li**, Y.-W. Yang, K.-M. Lin, and J.-S. Wu*, “Numerical and Experimental Investigation of Light Emission of a Planar Nitrogen Atmospheric-Pressure Dielectric Barrier Discharge Due to Addition of Ammonia Considering Oxygen Impurity,” Ninth International Conference on Flow Dynamics (ICFD2012), Sendai, Japan, September 19-21, 2012.
3. Y.-W. Yang, J.-Y. Wu, C.-T. Liu, G.-C. Liao, **F.-L. Li**, M.-H. Chiang, J.-S. Wu*, “Enhancement of Amine Functional Group Incorporation for Improving Biocompatibility Using a Two-Step Atmospheric-Pressure Plasma Jet Treatment,” The joint meeting of 11th APCPST (Asia Pacific Conference on Plasma Science and Technology) and 25th SPSM (Symposium on Plasma Science for Materials), Kyoto, Japan, October 2-5, 2012.
4. **F.-L. Li**, B.-R. Gu, K.-M. Lin, C.-T. Hung and J.-S. Wu*, “One-Dimensional Fluid Modeling of a Planar Atmospheric-Pressure $N_2/O_2/NH_3$ Dielectric Barrier Discharge with Reduced Chemical Kinetics,” Conference on Computational Physics, Kobe, Japan, October 14-18, 2012

